PHOTOTRIGGERING NITRIC OXIDE SYNTHASE FROM *GEOBACILLUS STEAROTHERMOPHILUS*

Thesis by
Gretchen Eva Keller

In Partial Fulfillment of the Requirements for the Degree
of
Doctor of Philosophy

CALIFORNIA INSTITUTE OF TECHNOLOGY
Pasadena, California
2013
(Defended October 1, 2012)

For Dorothy who always dug deeper

and for Peter who bridged art and science.

ACKNOWLEDGEMENTS

One of the more pleasant side effects of my extended stay in graduate school has been my interactions with an enormous number of truly wonderful people; I have been *incredibly* fortunate to have such a large and unique Caltech Family. Get comfy, this will be a very long read…

First, I need to thank the so-called "grown ups". My advisor, Harry Gray, has been a constant source of scientific inspiration and excitement. I would like to thank him for believing in everyone's potential, supporting his graduate students in travel, conferences, and networking, for opening doors, for being a sympathetic ear, for his "chemical intuition," for his appreciation of romance, and his outrageous overuse of the exclamation point!!!!!!!!!!! (totally warranted here). I thank Jay Winkler for always demanding more, for his constant questioning, for his uncanny ability to tinker and fix almost anything, and for that ridiculous ice-cream joke. Whether he realizes it or not, he has a profound impact on his students, and despite many difficult encounters with him, I have learned a great deal about science and myself from these interactions. I am also very grateful to my thesis committee: thanks to Bil Clemons for teaching me about structural biology and for his academic mentorship; to Dave Tirrell for his insightful comments and critiques; and to Jack Richards for attending all of my group meetings over the last 7 years, asking good questions, and genuinely caring about my progress.

I would not have gone to graduate school without the inspiration from some of my early mentors: in addition to sharing her love of inorganic chemistry, Carmen Works had an ankle tattoo of hydrogen-bonded water molecules that showed me even nerds can rock. Gary Carroll was my organic chemistry teacher at SBCC, always had an open door,

and taught me the value of being OCD in the lab. As an undergrad at UCSB, Tony Cheetham and Gui Bazan gave me the opportunities to explore life in a research lab. Kevin Plaxco got me excited about biochemistry and provided a great example of living a balanced academic life. I am grateful that Kevin has remained a friend and mentor.

Speaking of mentors, many people have helped in my Caltech experience, but there are three individuals specifically who deserve acknowledgement: Matt, Jeff, and Maraia. Matt Hartings has been a staunch and true friend since day one. Once we realized we could both quote the entirety of the movie Anchorman, it was game on! He has shared the ups and downs of our joint projects in and out of the lab, always offered good advice, a shoulder to cry on, the ability to make me laugh in the darkest (and often most inappropriate) of times, his lovely family has always welcomed me, and I just can't imagine getting through grad school without his support. Jeff Warren – Oh, el jeffe guapo, what can I say? When he first showed up as a postdoc in our lab, I sorta just took him for granted as a "Matt-lite": a reasonable replacement for my big-brother/mentor/lab-husband. But Jeff has proven to be weirder than I ever could have predicted. He has also been an invaluable resource in all things chemical, and dare I say proton-electron coupled, as well as in career and life goals. He has been a great travel buddy and is forever the king of the tuggle-hawks! Maraia Ener is actually a few years younger than me but she quickly became my mentor when I started my final project (which constitutes the bulk of this thesis). She is knowledgeable, patient, and always willing to take the time to teach others. The things she doesn't know, she finds out. She has a quiet modesty about her intelligence and an absolutely wicked sense of humor that still surprises me. She is one of those people you can count on to "show up," both emotionally and in

person (despite a horrible commute). She is a fellow mesophonic (look it up!) and somewhere along the line she became one of my very best friends at Caltech. I have been truly blessed to know her and hope that we stay close in our future endeavors.

Before I really get going here, I need to give another HUGE thanks to Jeff and Maraia who took on the lion's share of editing and proofreading this thesis. They also, along with Alec, Matt, Oliver, and Justin, helped edit my proposals. Thank you all!

In the beginning, we were bright-eyed and bushy-tailed… I had the excellent timing to begin graduate school and join the Gray lab at the same time as Jillian Dempsey, Morgan Cable, and Kyle Lancaster. The early days of my friendship with Jillian involved Amigos (with Val, Caroline, and Suz) and thankfully this evolved into classier wine-tasting and dinner parties! Jill has been a great friend, a scientific inspiration, and I'm super excited to see where her independent research career goes in the future. I will never forget meeting Morgan in Bercaw's Inorganic class "Hi, I'm Morgan. Let's be study-buddies," followed by a gift of fuzzy cat socks. I am so very glad that we became roommates, that we shared custody of the "great travel hat," and co-parented the kitties. Can't wait to see her launched into space! And Kyle, Kylie, Lyle, Lyla, Carlslyle, or whatever his name is, was like a brother to me. Kyle has been an ill-fated bench mate, partner-in-crime for taking back the Mondays, and a true friend.

I would also like to specifically thank Charlotte Whited, Alec Durrell, and Josh Palmer (and Elle!) for their friendship in and out of the lab. You guys have really made this whole debacle fun.

I have had two great officemates on the 3rd floor and I've enjoyed scientific discussion as well as their company: John Magyar and Nicole Bouley-Ford. Work in the

sub-basement of the BI over the years has been vastly improved by the presence of some wonderful labmates. Thanks to Melanie, Bert, Gitrada, Brian, Tetsu, and Matt for helping me get started and sharing the "rules of grad school." I give a huge thank you to all the people who have trained me on various BILRC instruments: John Magyar (ss-FL), Bert Lai (FPLC and CD), Tetsu Kimura and Matt Hartings (picosecond laser), Charlotte Whited ("wet box"), Jillian Dempsey, Alec Durrell and Maraia Ener (nanosecond laser), and Yuling Sheng (molecular biology goddess). More recently, we started having regular bio subgroup meetings to informally discuss our projects and get feedback. These discussions with Nicole, Maraia, Kana, Oliver, Peter, Jeff, Heather, and Keiko have been incredibly helpful, and I only regret that we didn't start this earlier. On the topic of subgroups, I'd like to acknowledge Team Haem Team (past and present): Yen Hoang Nguyen, Lionel Cheruzel, Charlotte Whited, and Maraia Ener. Their combined work on heme-thiolate enzymes paved the way for this thesis.

Outside of lab, there are a number of incredible Caltech staff that have helped make things run smoothly and enabled my research. I would like to thank Rick Jackson and Catherine May for providing everything the Beckman Institute denizens could possibly need (including half n half), Pat Anderson for keeping paperwork flowing smoothly and for always being chatty; Anne Penney and Chris Smith are unsung heroes of the chemistry department, and Chris has been a good friend; Dian Buchness, Laura Howe, and Agnes Tong for helping guide us grad students through all our requirements; Steve Gould for ordering all of our chemicals; Joe, Terry, and Ron for keeping us supplied (and seeing Joe always cheers me up); Cora and Carlos for keeping us stocked; Mona Shahgholi for help with mass spec/LC-MS; the folks at PPMAL for millions of

protein mass spectra; EH&S and the chemistry safety team for putting out fires and cleaning up spills; Larry Henling, Mike Day, and Dick Marsh for holding court in the 4th floor conference room every day at 3:30 pm; Bruce Brunschwig for his wit and absurd sense of humor; and Ernie Mercado, taco God and good friend, for 7 years of food comas (he's been feeding Caltech grad students for 25 years!).

Lab-hilarity has been an important part of getting me through grad school. Many thanks go to the early participants of hallway golf, to Kate for the hula hooping, to Alec and Matt for their random dance routines, to Lionel for his colorful language (pardon your French), to Charlotte for hiding in that huge FPLC box to scare the hell out of Kyle, to Jeff and Maraia for tinfoil hats, to Oliver and Peter for the continued game of throwing things through the holes in the ceiling, to Jeff and Peter for the scare-competitions, Seiji for that ridiculous wig, and to Kyle for putting up with Alec, Matt, and me epoxy-ing stuff onto your bench. Along with lab shenanigans, the Gray group sure does like to party! It has been my pleasure to plan many of these celebrations with Crystal Shih, Charlotte Whited, Paul Bracher, and most recently, with Oliver Shafaat (good luck, buddy!).

I wish I could acknowledge everyone individually, as I have truly enjoyed overlapping with the following people in the Gray group: Steve Contakes, Kate Pletneva, Jennifer Lee, Karn Sorasaenee, Don Walker, Paul Oblad, Bryan Stubbert, Matt Bierman, Astrid Mueller, Hemamala Karunadasa, Qixi Mi, Mike Rose, Yan Choi Lam, Judy Lattimer, James McKone, Chris Roske, Paul Bracher, James Blakemore, Daniel Konopka, and Smaranda Marinescu. And it has been fun getting to know the "new kids"

in the Gray Nation: Michael Lichterman, Tania Darnton, Carl Blumenfeld, and Bryan Hunter.

There are a number of people at Caltech outside of my research group that I would like to thank for their friendship and support. Leslie O'Leary and Rachel Klet have been great friends, and I've enjoyed our time together drinking wine, doing cardio-kick, jumping in pools, and generally commiserating. Go Team Unicorn! I am so glad that Samantha MacMillan decided to move here from MIT; becoming friends with Sam has been awesome! The Mentor House Salons during my first few years at Caltech were inspiring and fun. Thanks to Tamara Knutsen, Dylan Morris, Rob Walters, Dan Busby, Jeff Smith, and James Maloney, to name a few. I have really enjoyed getting to know and spending time with Eric Olmon, Chethana Kulkarni, Pam Sontz, Will Ford, Edgardo Garcia Berrios, Anna Folinsky, Liz Santori, Emily Warren, Justin Chartron, Young-In Oh, and Alex Goldberg (you still owe me an RC Cola, btw). Dave Weinberg and I have been through a hell of a lot and I'm so thankful for our time together, as well as our continued friendship. I would be remiss if I did not thank the Bercaw Group at large. I have immensely enjoyed lunches with the old Ernie's crew, the many backpacking trips, fantasy football leagues, summer softball with the Cp-AllStars, poker nights, and some of the absolutely worst hangovers of my life. Special thanks to Ian "Archie" Tonks, Dave Weinberg, Steve Baldwin, Alex Miller, Suz & Shane, Ned & Erin, A-rod & Kourtney, Paul & Stephanie, Val, Matt Winston, Rachel, Taylor, Jeff Byers, Theo Agapie, Paul Elowe, Jon Owen, Nilay, and John Bercaw himself for adopting me multiple times.

My life outside of Caltech is also blessed by a number of very special people. I'd like to thank Rob "Beanpot" Hansen: from biking to the Four Corners in middle school to

trekking across New Zealand a few years ago, our adventures have been a blast! Thanks also go to Clovis for being one of the most constant and trustworthy friends I've ever had. I have blown off a fair amount of grad school-induced steam with trips to Santa Barbara, and I am *very* grateful to those groups of friends for the good times hanging out on porches, drinking wine, dancing, and playing music all night. Thanks to Team Upside Down for the rollercoaster thrills and always keeping your damn hands in the air! And finally, I give my undying thanks to Ingrid for being my lifelong best friend. I am constantly inspired by her passion and honesty. She has truly been present at all stages of my life and my confidante. Hers is a friendship without disclaimer. It is difficult to put to words how much her support means to me.

I cannot thank my family enough for all they've done to support me. My extended family has remained a steadfast source of support and entertainment: Peter, Robert, Jessie, Tom, Sarah, Neal, Sam, Tom Jr., Suz, and Ned are all amazing people full of so much love and laughter! I miss you, Peter. Thanks also go to Korth family for being so loving and taking me in as one of their own. Maury Boswell has been a wonderful "sister" and her beautiful family an inspiration. What the heck, I've already gone on way too long, so I'll mention my cats. They're crazy little furry members of the family. Thanks to Mufasa, ThePeople, Dorian Gray, and the departed "Tiny."

My brother, Joshua Buckner Cobb, may very well have been the biggest influence in getting me here. He is one of those people who just does not understand the meaning of the word "impossible." Life keeps trying to explain it to him, but he won't budge. He also has one of the biggest hearts of anyone on Earth and this is reflected in his wonderful family, Ariana, Olivia, and Caleb! I thank him for all the little (and big) things he has

done for me over the years (including teaching me algebra by mail while he was living abroad). My dad, Bob Keller, is a wonderfully curious man and I treasure all of our conversations about life, science, relationships, and "what it all means." He has a way of reminding me of the big picture and what's really important. He also has a bizarre sense of humor that meshes so well with mine, there is no question we're related. This nut doesn't fall far from the tree. Eye Heart U. My mom, Kathryn Brown, is one of the most insightful, fun, and courageous women I've ever known. She has supported and loved me unconditionally (and deserves a medal for putting up with my antics over the years). I aspire to be more like her every day. Dorothy Boswell was my second mom and one of the major "forces" in my life. Forget electrostatic or gravitational, the Dorothy Force was truly impressive. She always dove in and got to the bottom of it, whatever it was. I miss her madly.

Lastly, I thank William Zachary Korth for being the best partner imaginable in every endeavor thinkable, for adventuring and nesting, for supporting me and calling me on my shit, for serenading me and for making me laugh, for being comfortably silent yet never running out of conversation, for sharing a life with me— a really, really, REALLY good life! And for giving me $3 that night to buy us all beer, for attending that new-new-year's party, for a truly Mammoth family reunion, for jumping out of that plane on our second date, and for never leaving.

ABSTRACT

Nitric oxide synthases (NOS) produce L-citrulline and nitric oxide (NO) in two turnovers from L-arginine via the bound intermediate, N-hydroxy-L-arginine. NO is an important biological signaling molecule, and NOS-like enzymes have been identified in all kingdoms of life. NOS enzymes utilize electrons from a reductase domain as well as a unique redox-active cofactor, tetrahydrobiopterin, in the activation of dioxygen. The NOS catalytic mechanism is only partially known, with proposed hihg-valent oxygenating intermediates similar to those of other monooxygenases. In the continued effort to understand the mechanism by which NOS catalytically produces NO, we have chosen to study NOS from the thermostable, nonpathogenic bacterium *Geobacillus stearothermophilus* (gsNOS).

In this work, covalently modified gsNOS with a ruthenium(II) diimine photosensitizer has been prepared to circumvent the need for an external reductase domain, while maintaining access to the substrate-binding channel. In this way, we hoped to produce the NOS ferrous state by rapid electron injection and to be able to access intermediates that form downstream. Chapter two describes the engineered gsNOS for selective cysteine labeling with $[Ru(bpy)_2(IA\text{-}phen)]^{2+}$ (IA-phen = 5-iodoacetamido-1,10-phenanthroline) to form the conjugate $Ru(II)_{K115C}$-gsNOS. The labeled protein was characterized by mass spectrometry, UV-visible absorbance, and circular dichroism spectroscopy. $Ru(II)_{K115C}$-gsNOS was crystallized and its structure solved to 2.6 Å

resolution. Chapter three details phototriggered reduction by laser flash-quench methodology using the reversible, reductive quencher *p*-methoxy-*N,N*-dimethylanaline. Transient absorption studies have shown that rapid phototriggered heme reduction occurs on the order of 625 ns. Binding of substrates and/or cofactor is known to alter the heme reduction potential in NOS. However, these observed reduction rates are independent of substrate/cofactor, suggesting that the system is driving force optimized. Studies performed in the presence of oxygen were complicated by side-reactions with the ruthenium label and small molecule quencher. Excitingly, enzymatic turnover was achieved by steady-state LED illumination at 470 nm using the irreversible reductive quencher diethyldithiocarbamate, and is described in chapter four. NO produced from light-driven $Ru(II)_{K115C}$-gsNOS catalysis was measured by the Griess Assay and L-citrulline production confirmed by liquid chromatography-mass spectrometry. In chapter five, we show how phototriggered heme reduction can be used to monitor CO binding and potential studies of gas diffusion pathways, and substrate/cofactor effects are discussed. In all, the development of this ruthenium-modified gsNOS system has enabled preliminary studies of reduction kinetics, diatomic ligand binding, and light-driven catalysis and may provide a useful platform for further investigation into the catalytic cycle of NOS.

TABLE OF CONTENTS

LIST OF FIGURES

LIST OF SCHEMES AND TABLES

Chapter One

INTRODUCTION

1.1 Nitric Oxide Synthases

The radical nitric oxide (NO) is now recognized as an essential biological regulator after having been long considered solely a poison and pollutant.[1] NO has many roles, such as an endothelial relaxing factor, a protective immunocytotoxin, and a signaling molecule in the nervous system.[2] NO is produced in mammals by a family of nitric oxide synthases (mNOS). The family contains three isoforms: endothelial (eNOS), inducible (iNOS), and neuronal NOS (nNOS) and NOS dysfunction is implicated in a variety of disease states.[3,4] mNOS catalyzes the oxidation of L-arginine (L-Arg) to L-citrulline (L-Cit) and NO. The reaction proceeds in two turnovers with N^{ω}-hydroxy-L-arginine (NOHA) as a stable, enzyme-bound intermediate[5] and the overall reaction is shown in Scheme 1.1.

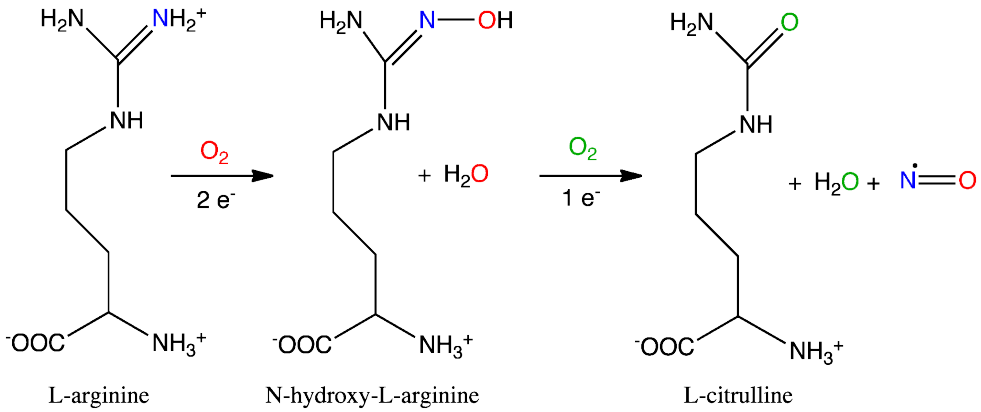

Scheme 1.1 Overall reaction for the NOS-catalyzed production of NO and L-Cit starting with L-Arg, via the intermediate NOHA. The oxygen atom in both NO and L-Cit come from dioxygen; the nitrogen atom in NO is derived from the guanidinium nitrogen in L-Arg.

All three mNOS isoforms are active as homodimers that contain an oxygenase domain linked to reductase domain.[6] The oxygenase domain houses a cysteine-ligated heme, as well as substrate and redox cofactor binding sites that create the active site of

the enzyme. The dedicated reductase domain is connected through a calmodulin linker and has binding sites for flavin adenine dinucleotide (FAD), flavin mononucleotide (FMN), and nicotinamide adenine dinucleotide phosphate (NADPH).[5] In eNOS and nNOS, the reductase domain is regulated by the calmodulin peptide linker that prevents electron transfer in the absence of bound Ca^{2+}.[7] In all cases, the reductase domain is the initial source of electrons necessary to initiate catalysis; the unique redox-active cofactor (6R)-5,6,7,8-tetrahydrobiopterin (H_4B, pterin) provides additional reducing equivalents to complete the cycles. While there is structural data available for the separate reductase and oxygenase domains[8,9,10] there is no crystal structure for full-length mNOSs to date, and thus the *in vivo* connectivity/domain interaction is only estimated (Figure 1.1).

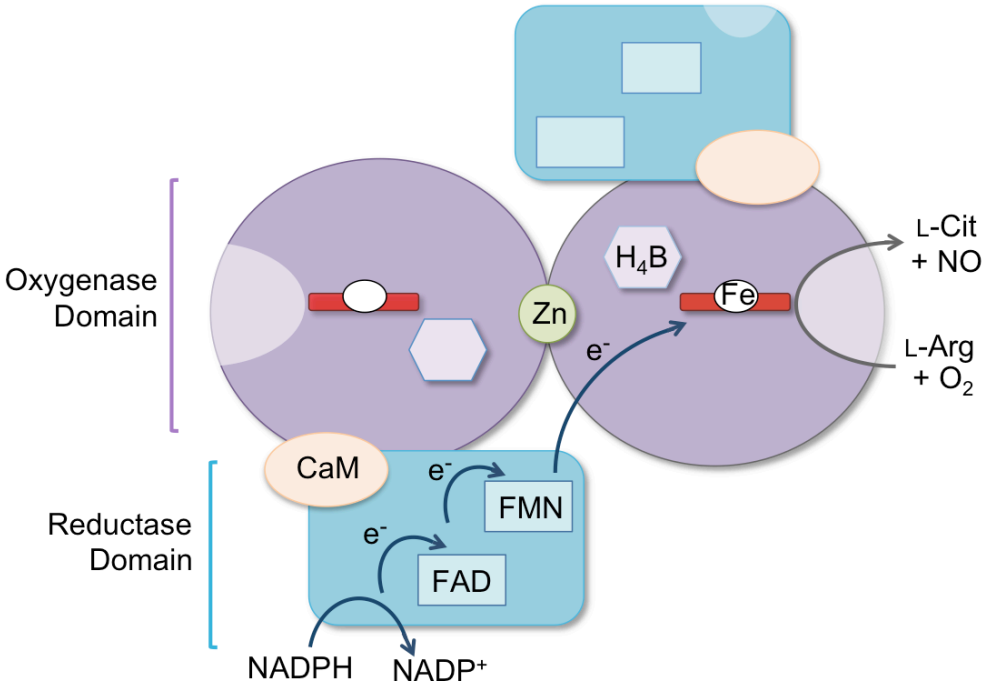

Figure 1.1 Illustrative representation of possible full-length NOS domain interactions, cofactor binding, and electron flow in the production of NO (adapted from Alderton[5] and Nguyen[11]).

1.2 Bacterial NOS

Many bacterial NOS homologs have now been identified that exhibit NOS-like activity,[12] leading researchers over the last decade to look toward them as useful parallel systems for studying mNOS. As NO produced from a certain mNOS is used as a toxin *against* bacterial infection,[7] the biological role of NO in prokaryotes remains an open question. However, *in vivo* NO production has now been confirmed[13,14] and current research suggests that different bacteria may use NO quite differently from mammals.[2] Bacterial NOS shares remarkably similar three-dimensional structure and sequence homology with mNOS,[15] however there are some notable differences. Bacterial NOS lacks the N-terminal motif at the dimer interface involved in zinc coordination and the N-terminal hook involved in H_4B binding.[2] The most striking difference is the lack of a dedicated linked reductase domain in bacterial NOS (with the exception of *Sorangium cellulosum*).[16] Three bacterial forms of NOS have been crystallized from *Bacillus subtilis* (bsNOS),[17] *Staphylococcus aureus* (saNOS),[18] and *Geobacillus stearothermophilus* (gsNOS).[19] All form stable dimers and bind H_4B; the ability to bind cofactor in the absence of the hook is explained by dimer interface residue substitutions. Overall, their structures are very similar to each other and to the oxygenase domains of mNOS (Figure 1.2). The winged β-sheet core is maintained around the active site, as is the conserved Trp that stacks with the heme on the proximal side and hydrogen bonds with the Cys thiolate sulfur. The hydrophobic "helical lariat" involved in pterin cofactor binding makes up much of the dimer interface and is surrounded by the T-shaped helices that associate across the two subunits.[2]

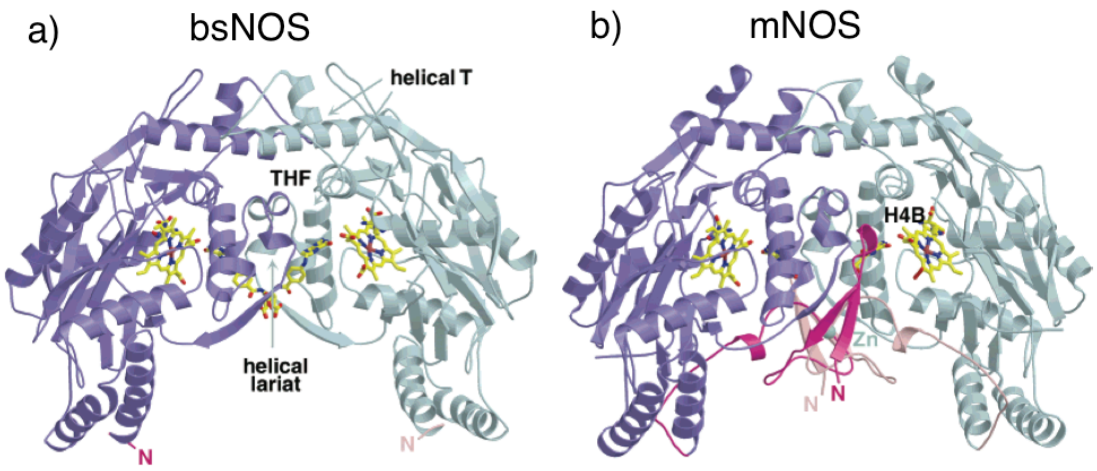

Figure 1.2 Comparison of representative dimeric structures of bacterial and mammalian NOS showing nearly identical overall folds: a) *Bacillus subtilis*, highlighting alternate bound cofactor, tetrahydrofolate (THF); b) inducible NOS from mammalian macrophages, highlighting bound cofactor, tetrahydrobiopterin (H_4B) and the missing N-terminal hook in pink (reproduced from Pant[17]).

Despite slight differences in heme electronics and substrate/cofactor binding, bacterial NOS and mNOS are suggested to share the same mechanism for catalytic production of NO from L-Arg via the bound NOHA intermediate[20] when supplied with electrons from exogenous reductase domains. There are various advantages to working with bacterial NOS including good overexpression yields in *E. coli* and increased stability,[21] particularly in the case of the thermostable gsNOS. Due to their overall similarities in structure and reactivity (both *in vitro* and *in vivo*),[13,19,22,23] it is thought that lessons learned from these NOS-like enzymes can be applied to their mammalian counterparts.

1.3 Mechanism of Catalytic NO Production

NOS belongs to a superfamily of cysteine thiolate-ligated heme enzymes, largely consisting of cytochromes P450 and including chloroperoxidase (CPO).[24] These

monooxygenases activate dioxygen (O_2) to incorporate an oxygen atom into a variety of substrates.[25] P450s, in particular, catalyze a truly impressive array of regio- and stereospecific transformations, including hydroxylations of saturated hydrocarbons, aromatic oxidations, and epoxidations.[26] Owing to its synthetic utility,[27] as well as its biological importance, the reactivity and mechanism of P450 have been extensively investigated.[28] The full two-step mechanism of NO production by NOS is not yet fully understood.[29] The first turnover is a two-electron oxidation of L-Arg resulting in the hydroxylation of a guanidinium nitrogen to form NOHA in a reaction that is nearly identical to that of P450-catalyzed hydroxylation. Thus, the first turnover is thought to follow a cycle similar to that of the well-studied P450s; the second turnover, a one-electron oxidation, is thought to follow a unique mechanism.[30] The NOS resting state is a six-coordinate aquo-ferric heme with an equilibrium of low- and high-spin states ("mixed-spin"). Substrate binding (L-Arg in the first cycle and NOHA in the second) in the pocket sterically displaces water to form a five-coordinate high-spin ferric state.[25] Ferric NOS is reduced by one electron from the reductase domain to give a ferrous species that can bind O_2. Oxygen binding gives a ferrous-oxy species (often represented as a ferric-superoxide), that is further reduced by one electron supplied by the redox-active cofactor H_4B.[31] The next experimentally observed species is the ferric resting state with bound NOHA. The missing reactive intermediate is thought to be a ferryl porphyrin radical cation,[32] analogous to compound I (Cpd I) in P450. The second turnover of the NOS catalytic cycle has similar steps: reduction, O_2-binding, and a second reduction by H_4B. From there, the next observed species is the ferric-NO, which then releases NO (and L-Cit) to complete the cycle. The reactive intermediate responsible for the oxygenation of

NOHA to form L-Cit as product in the second turnover is proposed to be either a hydroperoxo ferriheme[33] or Cpd I formed by subsequent protonation and water loss.[32] Known and proposed intermediates of both turnovers in the catalytic production of NO by NOS are shown in Figure 1.3. Spurred on by the desire to capture these elusive intermediates and encouraged as pieces of the puzzle fall into place, the exciting field of NOS research continues to grow.

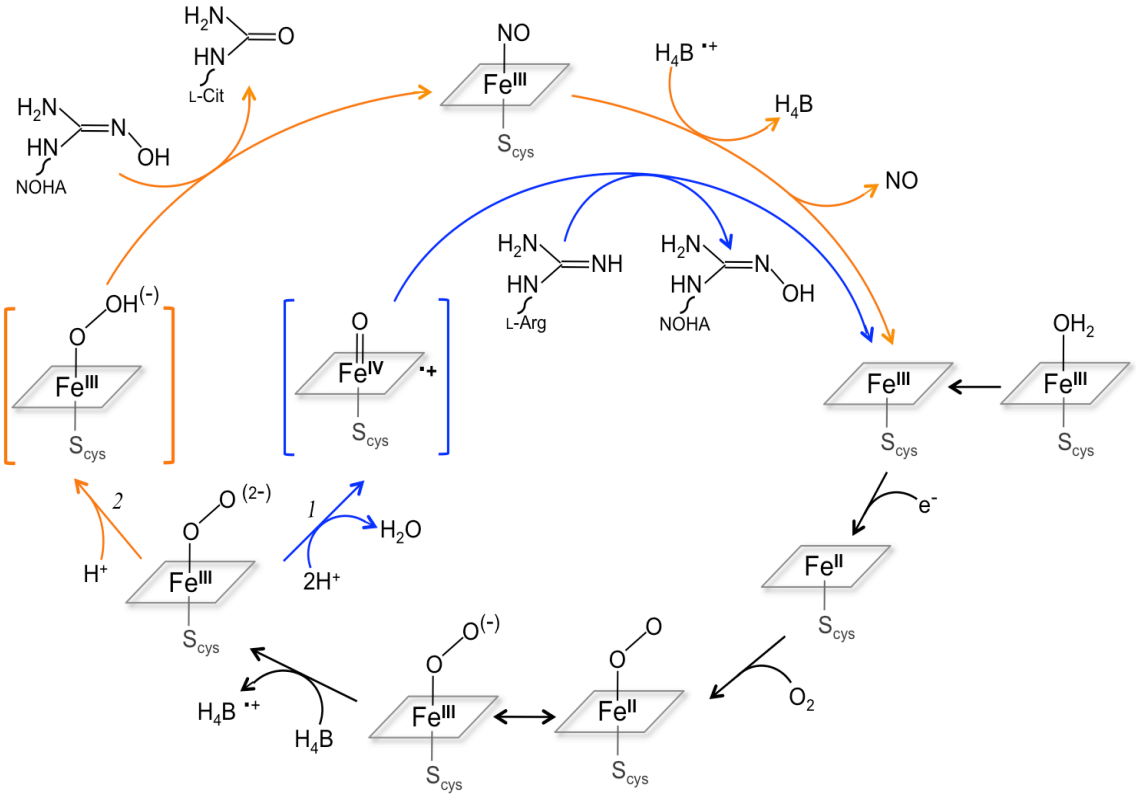

Figure 1.3 Putative mechanism for the catalytic production of NO by NOS enzymes: (1) first turnover formation of NOHA from L-Arg, shown in blue path; (2) second turnover formation of L-Cit and NO radical from NOHA, shown in orange path. The proposed oxygenating intermediates are in brackets.

1.4 Interaction with Diatomic Molecules

While great strides have been made to characterize the unique reactivity of NOS enzymes, there are still many questions that remain unanswered about NO production by NOS. In addition to definitively identifying the reactive intermediates involved in these heme-based oxygenations, it is of interest to understand how NOS interacts with diatomic ligands: O_2 is a reactant (cosubstrate) and NO is a product in this very complex transformation. Distinct gas diffusion pathways are possible and the heme interaction with diatomics is sensitive to substrate and cofactor binding.[20,31,34] A wide variety of techniques, including UV-visible spectroscopy,[20] stopped-flow spectrophotometry,[35] X-ray crystallography,[36,37] electron paramagnetic resonance (EPR), electron-nuclear double resonance (ENDOR)[32] and Raman spectroscopies[38,39] have been used by researchers to gain insight into the interactions of diatomics with mNOS and bacterial NOS. Studies involving O_2 are challenging due to its redox activity, so both NO and carbon monoxide (CO) have been used as surrogates for gas binding while single-turnover experiments have been used for studies of NO release.[16,40–42]

A significant difference between mammalian and bacterial NOSs is in the notably slower NO-release rates observed for bacterial NOSs.[2] Structure and sequence comparisons reveal variations in a few key residues thought to "gate" NO release.[17,42] For example, a conserved Val located directly above the distal side of the heme in mNOS is an Ile in many bacterial NOSs and is thought to slow gas release by sterically constraining the active site.[43] The second gate residue shows more variation, both in position and size of residue, but again NO-release rates seem correlated with steric bulk.[19,42] These gate effects on NO-release have been studied by single-turnover

experiments. Flash photolysis of ferrous-CO adducts is another useful technique for studying interactions of heme proteins with diatomics.[44–46] Excitation by visible light causes rapid CO dissociation and because the iron retains its oxidation state, the released CO can rebind. This rebinding process can be followed by transient absorption (TA) spectroscopy that monitors changes in the heme Soret maxima (e.g., ferrous NOS-CO λ_{max} = 446 nm vs. ferric NOS λ_{max} = 400 nm).[37] Preliminary CO-photolysis experiments have been performed to determine whether diatomic ligand rebinding is also affected by channel gating.[47]

1.5 Accessing Intermediates

The high reactivity and short lifetimes of the proposed oxygenating intermediates in the NOS cycle, along with the relatively slow rates of electron injection, has prohibited their observation. Furthermore, the dependence on a reductase domain as well as the benchtop instability of full-length mNOS has created difficulties for researchers. One way to access these types of reactive intermediates is through rapid phototriggered electron transfer (ET); indeed, previous work in the Gray group has found success using what is now known as "flash-quench" methodology[48] (Scheme 1.2). The excited state of ruthenium(II)diimine photosensitizers, such as $[Ru(bpy)_3]^{2+}$ (bpy = 2,2'-bipyridine), lies ~2.1 eV above the ground state with a lifetime greater than 600 ns in water.[49] This excited state is accessible by illuminating into the metal-to-ligand charge-transfer (MLCT) band at 400–500 nm (the "flash"). Introduction of another small molecule of an appropriate reduction potential (the "quench") can lead to the formation of either a potent -1.3 V reductant, $[Ru(bpy)_3]^{1+}$, or +1.3 V oxidant, $[Ru(bpy)_3]^{3+}$ allowing injection or

removal of an electron from the system of interest.[49] The flash-quench system can by tuned by photosensitizer (metal and/or ligands) or by quencher choice: reductive vs. oxidative and reversible vs. irreversible. The use of reversible quenchers results in the eventual return to the resting oxidation states through back-reaction with either the photosensitizer or a resultant redox species in solution. Irreversible quenchers undergo chemistry upon interaction with the photosensitizer excited state that prevents any further back-reaction and are often useful to further extend the lifetime of the desired reductant/oxidant.[50] The power of the flash-quench system lies in the rapid production of an extremely potent reductant or oxidant, depending on choice of quencher, and the extended lifetime afforded through charge separation, buying time to perform the desired redox chemistry. This technique has been successfully applied to small molecule systems[51,52] as well as proteins.[53]

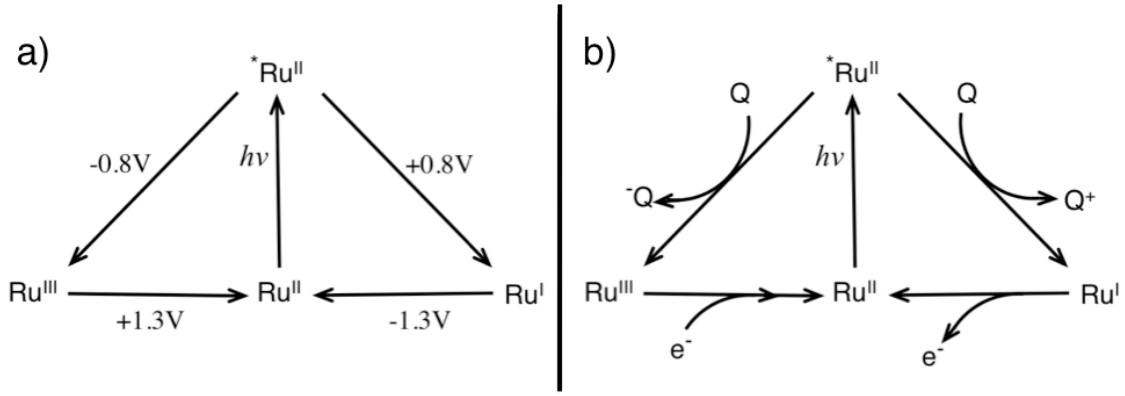

Scheme 1.2 Flash-quench scheme showing both reductive and oxidative quenching routes a) Reduction potentials are given for $Ru(bpy)_3$ species in water.[49] b) Ru represents $Ru(bpy)_3$, Q^+ and Q^- represent oxidative and reductive small-molecule quenchers, respectively.

Previous work in the Gray group has found success in accessing high-valent reaction intermediates in heme systems using flash-quench methodology. Changes in the spin and oxidation states of heme systems result in pronounced shifts in absorption

features, such as in the Soret and Q bands.[25] These shifts can be monitored by transient absorption (TA) spectroscopy and provide an optical handle by which to follow a reaction. The highly solvent-exposed, *c*-type heme in microperoxidase- 8 (MP8)[54] was an ideal initial target for photooxidative studies and led the way to investigations of horseradish peroxidase (HRP).[50] In both cases, the excited state of $[Ru(bpy)_3]^{2+}$ in solution was oxidatively quenched to form $[Ru(bpy)_3]^{3+}$ which was able to oxidize the heme, allowing observation of both ferryl porphyrin radical cation (Cpd I) and the ferryl (Cpd II) species. The reversible quencher, $[Ru(NH_3)_6]^{3+}$, worked well for MP8, but a longer $[Ru(bpy)_3]^{3+}$ oxidized state was required to allow for ET with the slightly less exposed heme in HRP. In the latter case, use of an irreversible quencher was necessary to extend the lifetime of Ru(III) oxidants. Extension to more complex systems, such as P450s and $iNOS_{oxy}$, proved difficult due to the much more buried heme environments of these enzymes. In a project subsequently known as "wires," modified photosensitizers were synthesized with an attached tail that mimicked the appropriate substrate for the given enzyme.[55] As such, the substrate tail gained access to the buried active site, thus establishing electronic communication between the heme and the $[Ru(bpy)_3]^{2+}$ sensitizer. High-valent intermediates were not observed; however efficient heme photoreduction was achieved.[56–58] A fundamental issue with these "wires" arises from the fact that in order to engage in ET, they must bind in the substrate channel. This prevents catalysis and excludes H_2O and/or O_2 needed to access Cpd I or II.

Recent work with P450-BM3 has overcome the problems described above by covalently linking a Ru(II)diimine photosensitizer to the surface of the protein, enabling through-bond ET without blocking the substrate channel.[59] By using site-directed

mutagenesis to engineer a single, nonnative surface cysteine, researchers in our group were able to control the distance to the active site as well as ensure unique labeling. Flash-quench experiments using a reversible oxidative quencher led to observation of various porphyrin radical cation intermediates and Fe(IV)-hydroxide (protonated Cpd II) by TA spectroscopy. This was the first example of a photochemically generated Cpd II in P450. Analysis of their TA data suggested formation of six distinct species following laser excitation. Three species were easily identified and the three remaining intermediates were determined by extensive modeling, partially constrained by previously published results from the oxidation of HRP[50] and MP8.[54] An illustration of the sequential kinetics model used for analysis of P450-BM3 oxidation is shown in Figure 1.4.

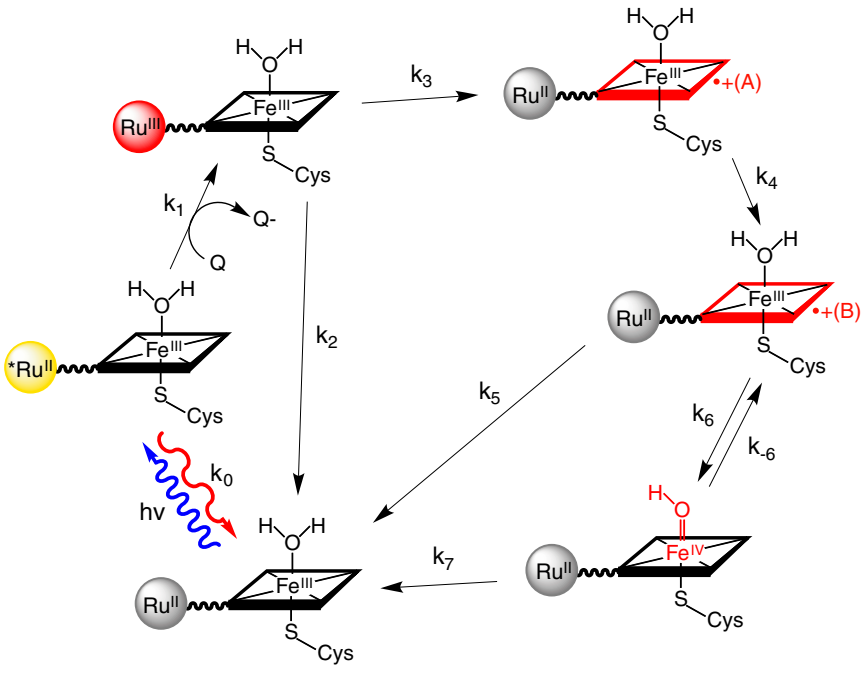

Figure 1.4 Diagram of the model for photochemical P450-BM3 heme oxidation used in transient absorption kinetics analysis (figure reproduced from Ener[59]).

1.6 Moving Forward with gsNOS

In the continued effort to understand the mechanism by which NOS catalytically produces NO, this thesis details work with NOS from the thermostable, nonpathogenic bacterium *Geobacillus stearothermophilus* (gsNOS). gsNOS was first crystallized and structurally characterized in 2006.[19] The enhanced stability of this enzyme, as well as other unique properties, presents a convenient system to study the NOS catalytic cycle. The structure of gsNOS is quite similar to other bacterial NOS-like enzymes, as well as $mNOS_{oxy}$: Cys76 provides thiolate ligation to the heme and stacking with the conserved Trp70 is maintained. The H_4B cofactor-binding site is formed by interface residues: Trp332, Phe347 in subunit one and Trp334, Arg252 in subunit two (Figure 1.5-a). However, there are some differences that seem to have pronounced effects on its interactions with diatomic molecules. Previous studies demonstrated that the ferrous-oxy species is remarkably long-lived in gsNOS,[19] with a lifetime on the order of >60 seconds at 4 °C, compared to seconds in other NOS systems. gsNOS also has the slowest reported NO release rate of both mNOS and bacterial NOS systems; this is ascribed to the bulkier "gate" mutations described previously. Structural analysis revealed another substitution (Arg365 for Lys356 in bsNOS) that plays a role in creating a more constrained active site in gsNOS. This arginine residue is engaged in a hydrogen-bonding network involving Asp225 and Ser224 that ultimately pushes the Ile223 gate residue approximately 0.6 Å closer to the heme iron atom (Figure 1.5-b). This further tightening could also play a role in the slower observed NO release rates. While the dimer interface overlays nearly perfectly with bsNOS, the overall fold of gsNOS appears more compact. Additionally, Resonance Raman spectroscopy has shown unique heme environments in both the distal

and proximal pockets that are very sensitive to substrate binding.[39] In experiments with CO bound at the heme, L-Arg and NOHA are shown to each stabilize different conformations as manifested in the Fe-CO and Fe-Cys stretching modes.

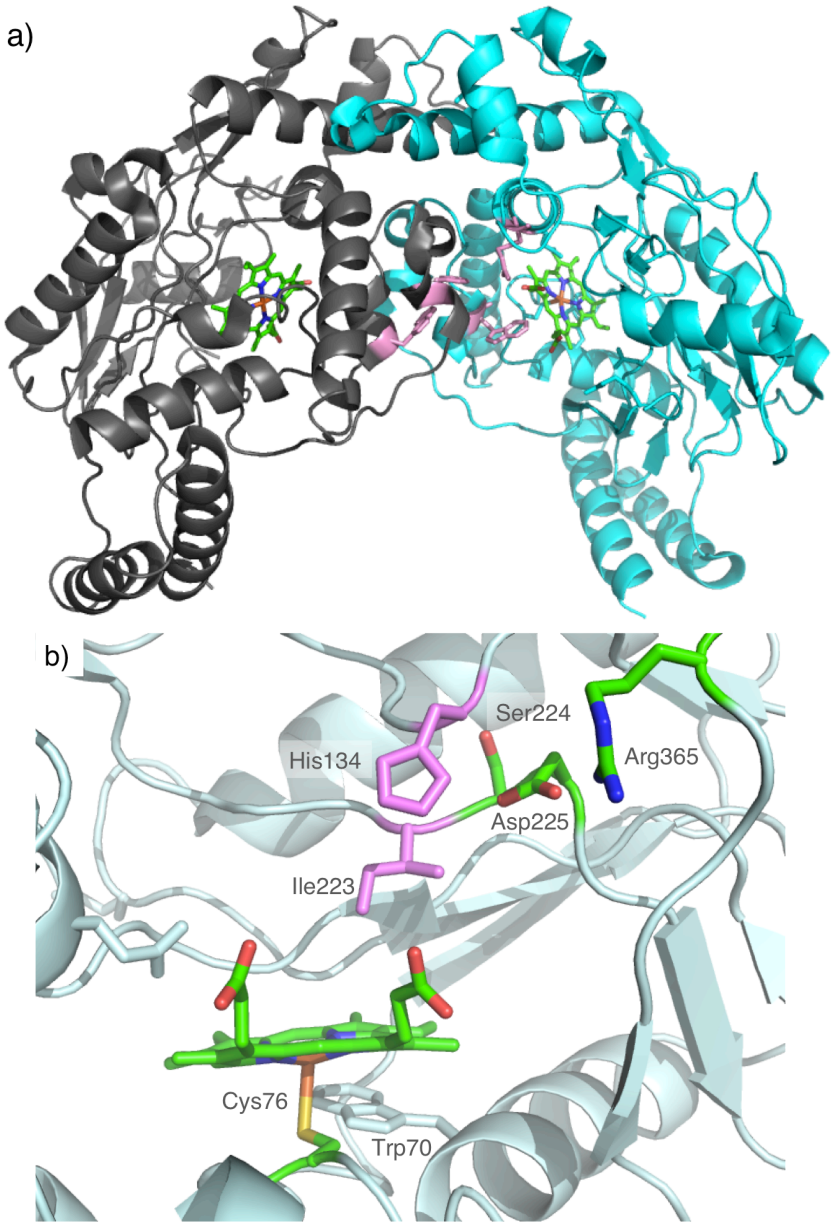

Figure 1.5 a) structure of gsNOS dimer (subunit interface residues involved in H_4B binding shown in violet); b) gsNOS active site highlighting key residues (NO-release "gate" residues shown in pink, hydrogen-bonding network responsible for constrained active site colored by element, conserved Trp, and proximal heme-thiolate by Cys76) PDB code 2FLQ, figure made with MacPymol 2009.

In this work, we covalently modified gsNOS with a ruthenium(II) diimine photosensitizer to circumvent the need for an external reductase domain, while maintaining access to the substrate-binding channel. In this way, we hoped to produce the NOS ferrous state by rapid electron injection and be able to access intermediates that form downstream. Chapter two describes our engineered gsNOS for selective cysteine labeling with $[Ru(bpy)_2(IA\text{-}phen)]^{2+}$ (IA-phen = 5-iodoacetamido-1,10-phenanthroline) to form the conjugate $Ru(II)_{K115C}$-gsNOS, as well as its structural characterization by X-ray crystallography. Chapter three details phototriggered reduction by laser flash-quench methodology using the reversible, reductive quencher *p*-methoxy-*N,N*-dimethylanaline (MeODMA). Enzymatic turnover was achieved by steady-state LED illumination and is described in chapter four. In chapter five, we show how phototriggered heme reduction can be used to monitor CO binding and potential studies of gas diffusion pathways as well as substrate/cofactor effects are discussed. In all, the development of this ruthenium-modified gsNOS system has enabled preliminary studies of reduction kinetics, diatomic ligand binding, and light-driven catalysis. It is my hope that $Ru(II)_{K115C}$-gsNOS may provide a useful platform for further investigation into the exciting and challenging catalytic cycle of NOS.

1.7 References

1. Hughes, M. N. Chemistry of Nitric Oxide and Related Species. *Methods Enzymol* **436**, 3–19 (2008).
2. Crane, B. R., Sudhamsu, J. & Patel, B. A. Bacterial Nitric Oxide Synthases. *Annu Rev Biochem* **79**, 445–470 (2010).
3. Kendrick, K. M. *et al.* Formation of olfactory memories mediated by nitric oxide. *Nature* **388**, 670–673 (1997).
4. Luth, H.J., Holzer, M., Gartner, U., Staufenbiel, M., Arendt, T. Expression of Endothelial and Inducible NOS-isoforms is Increased in Alzheimer's Disease... *Brain Res* **913**, 57-67 (2001).
5. Alderton, W. K., Cooper, C. E., Knowles, R. G. Nitric Oxide Synthase: Structure, Function, and Inhibition. *Biochem J* **357**, 593-615 (2001).
6. Stuehr, D. Oxygen Reduction by Nitric-oxide Synthases. *J Biol Chem* **276**, 14533–14536 (2001).
7. Moncada, S. & Bolanos, J. P. Nitric oxide, cell bioenergetics and neurodegeneration. *J Neurochem* **97**, 1676–1689 (2006).
8. Crane, B. R. The Structure of Nitric Oxide Synthase Oxygenase Domain and Inhibitor Complexes. *Science* **278**, 425–431 (1997).
9. Crane, B. R. Structure of Nitric Oxide Synthase Oxygenase Dimer with Pterin and Substrate. *Science* **279**, 2121–2126 (1998).
10. Feng, C. Mechanism of nitric oxide synthase regulation: Electron transfer and interdomain interactions. *Coordination Chemistry Reviews* **256**, 393–411 (2012).
11. Nguyen, Y. H. Wiring Inducible Nitric Oxide Synthase; PhD Thesis; California Institute of Technology, Pasadena, 2006.
12. Kunst, F., Ogasawara, N., Moszer, I. & et al. The complete genome sequence of the gram-positive bacterium Bacillus subtilis. *Nature* **390**, 249–256 (1997).
13. Adak, S. Direct Evidence for Nitric Oxide Production by a Nitric-oxide Synthase-like Protein from Bacillus subtilis. *J Biol Chem* **277**, 16167–16171 (2002).
14. Johnson, E. G. *et al.* Plant-Pathogenic Streptomyces Species Produce Nitric Oxide Synthase-Derived Nitric Oxide in Response to Host Signals. *Chem Biol* **15**, 43–50 (2008).
15. Gusarov, I. *et al.* Bacterial Nitric-oxide Synthases Operate without a Dedicated Redox Partner. *J Biol Chem* **283**, 13140–13147 (2008).
16. Agapie, T. *et al.* NO formation by a catalytically self-sufficient bacterial nitric oxide synthase from Sorangium cellulosum. *Proc Nat Acad Sci USA* **106**, 16221–16226 (2009).
17. Pant, K., Bilwes, A. M., Adak, S., Stuehr, D. J. & Crane, B. R. Structure of a Nitric Oxide Synthase Heme Protein from Bacillus subtilis. *Biochemistry* **41**, 11071–11079 (2002).
18. Bird, L. E. *et al.* Crystal structure of SANOS, a bacterial nitric oxide synthase oxygenase protein from Staphylococcus aureus. *Structure* **10**, 1687–1696 (2002).
19. Sudhamsu, J. Structure and Reactivity of a Thermostable Prokaryotic Nitric-oxide Synthase That Forms a Long-lived Oxy-Heme Complex. *J Biol Chem* **281**, 9623–9632 (2005).

20. Salard-Arnaud, I., Stuehr, D., Boucher, J.-L. & Mansuy, D. Spectroscopic, catalytic and binding properties of Bacillus subtilis NO synthase-like protein: Comparison with other bacterial and mammalian NO synthases. *J Inorg Biochem* **106**, 164–171 (2012).
21. Sudhamsu, J. & Crane, B. R. Bacterial nitric oxide synthases: what are they good for? *Trends Microbiol* **17**, 212–218 (2009).
22. Shatalin, K. *et al.* Bacillus anthracis-derived nitric oxide is essential for pathogen virulence and survival in macrophages. *Proc Nat Acad Sci USA* **105**, 1009 (2008).
23. Reece, S. Y., Woodward, J. J. & Marletta, M. A. Synthesis of Nitric Oxide by the NOS-like Protein from Deinococcus radiodurans: A Direct Role for Tetrahydrofolate. *Biochemistry* **48**, 5483–5491 (2009).
24. Nelson, D. R., Kamataki, T., Waxman, D. J., et al. The P450 Superfamily: Updaate on New Sequences, Gene Mapping, Accession Numbers, Early Trivial Names of Enzymes, and Nomenclature. *DNA Cell Biol* **12**, 1-51 (1993).
25. Sono, M., Roach, M. P., Coulter, E. D., Dawson, J. H., Heme-Containing Oxygenases. *Chem Rev* **96**, 2841-2887 (1996).
26. Guengerich, F. P. Common and Uncommon Cytochrome P450 Reactions Related to Metabolism and Chemical Toxicity. *Chem Res Toxicol* **14**, 611-650 (2001).
27. Groves, J. T. High-valent iron in chemical and biological oxidations. *J Inorg Biochem* **100**, 434–447 (2006).
28. Meunier, B., de Visser, S. P. & Shaik, S. Mechanism of Oxidation Reactions Catalyzed by Cytochrome P450 Enzymes. *Chem Rev* **104**, 3947–3980 (2004).
29. Stuehr, D. J. Update on Mechanism and Catalytic Regulation in the NO Synthases. *J Biol Chem* **279**, 36167–36170 (2004).
30. Zhu, Y. & Silverman, R. B. Revisiting Heme Mechanisms. A Perspective on the Mechanisms of Nitric Oxide Synthase (NOS), Heme Oxygenase (HO), and Cytochrome P450s (CYP450s). *Biochemistry* **47**, 2231–2243 (2008).
31. Wei, C.-C., Crane, B. R. & Stuehr, D. J. Tetrahydrobiopterin Radical Enzymology. *Chem Rev* **103**, 2365–2384 (2003).
32. Davydov, R. *et al.* EPR and ENDOR Characterization of Intermediates in the Cryoreduced Oxy-Nitric Oxide Synthase Heme Domain with Bound l-Arginine or N G Hydroxyarginine. *Biochemistry* **41**, 10375–10381 (2002).
33. Woodward, J. J., Chang, M. M., Martin, N. I. & Marletta, M. A. The Second Step of the Nitric Oxide Synthase Reaction: Evidence for Ferric-Peroxo as the Active Oxidant. *J Am Chem Soc* **131**, 297–305 (2009).
34. Salard, I. *et al.* Analogies and surprising differences between recombinant nitric oxide synthase-like proteins from Staphylococcus aureus and Bacillus anthracis in their interactions with l-arginine analogs and iron ligands. *J Inorg Biochem* **100**, 2024–2033 (2006).
35. Wei, C. C., Wang, Z. Q. & Stuehr, D. J. Nitric oxide synthase: Use of stopped-flow spectroscopy and rapid-quench methods in single-turnover conditions to examine formation and reactions of heme-O2 intermediate in early catalysis. *Methods Enzymol* **354**, 320–338 (2002).

36. Pant, K. & Crane, B. R. Nitrosyl–Heme Structures of Bacillus subtilis Nitric Oxide Synthase Have Implications for Understanding Substrate Oxidation. *Biochemistry* **45**, 2537–2544 (2006).
37. Doukov, T., Li, H., Soltis, M. & Poulos, T. L. Single Crystal Structural and Absorption Spectral Characterizations of Nitric Oxide Synthase Complexed with N ω-Hydroxy-l-arginine and Diatomic Ligands. *Biochemistry* **48**, 10246–10254 (2009).
38. Santolini, J., Roman, M., Stuehr, D. J. & Mattioli, T. A. Resonance Raman Study of Bacillus subtilis NO Synthase-like Protein: Similarities and Differences with Mammalian NO Synthases. *Biochemistry* **45**, 1480–1489 (2006).
39. Kabir, M., Sudhamsu, J., Crane, B. R., Yeh, S.-R. & Rousseau, D. L. Substrate–Ligand Interactions in Geobacillus stearothermophilus Nitric Oxide Synthase. *Biochemistry* **47**, 12389–12397 (2008).
40. Boggs, S., Huang, L. & Stuehr, D. J. Formation and Reactions of the Heme–Dioxygen Intermediate in the First and Second Steps of Nitric Oxide Synthesis As Studied by Stopped-Flow Spectroscopy under Single-Turnover Conditions. *Biochemistry* **39**, 2332–2339 (2000).
41. Tejero, J. *et al.* Stabilization and Characterization of a Heme-Oxy Reaction Intermediate in Inducible Nitric-oxide Synthase. *J Biol Chem* **283**, 33498–33507 (2008).
42. Whited, C. A. *et al.* Gating NO Release from Nitric Oxide Synthase. *J Am Chem Soc* **134**, 27-30 (2012).
43. Wang, Z.-Q. A Conserved Val to Ile Switch near the Heme Pocket of Animal and Bacterial Nitric-oxide Synthases Helps Determine Their Distinct Catalytic Profiles. *J Biol Chem* **279**, 19018–19025 (2004).
44. Scheele, J. S. *et al.* Kinetics of CO ligation with nitric-oxide synthase by flash photolysis and stopped-flow spectrophotometry. *J Biol Chem* **272**, 12523–12528 (1997).
45. Stevenson, T. H., Gutierrez, A. F., Alderton, W. K., Lian, L. & Scrutton, N. S. Kinetics of CO binding to the haem domain of murine inducible nitric oxide synthase: differential effects of haem domain ligands. *Biochem J* **358**, 201 (2001).
46. Cao, W. *et al.* Investigations of Photolysis and Rebinding Kinetics in Myoglobin Using Proximal Ligand Replacements. *Biochemistry* **43**, 11109–11117 (2004).
47. Whited, C. A. Tuning Nitric Oxide Synthase: Investigating the Thiolate 'Push' and NO Release; PhD Thesis; California Institute of Technology, Pasadena, 2011.
48. Chang, I. J., Gray, H. B. & Winkler, J. R. High-driving-force electron transfer in metalloproteins: intramolecular oxidation of ferrocytochrome c by Ru (2, 2'-bpy) 2 (im)(his-33) 3+. *J Am Chem Soc* **113**, 7056–7057 (1991).
49. Huynh, M. H. V., Dattelbaum, D. M. & Meyer, T. J. Exited state electron and energy transfer in molecular assemblies. *Coord Chem Rev* **249**, 457–483 (2005).
50. Berglund, J., Pascher, T., Winkler, J. R., Gray, H. B. Photoinduced Oxidation of Horseradish Peroxidase. *J Am Chem Soc* **119**, 2464-2469 (1997).
51. Ogata, T., Yanagida, S., Brunschwig, B. S. & Fujita, E. Mechanistic and Kinetic Studies of Cobalt Macrocycles in a Photochemical CO2 Reduction System: Evidence of Co-CO2 Adducts as Intermediates. *J Am Chem Soc* **117**, 6708–6716 (1995).

52. Dempsey, J. L., Winkler, J. R. & Gray, H. B. Kinetics of Electron Transfer Reactions of H2-Evolving Cobalt Diglyoxime Catalysts. *J Am Chem Soc* **132**, 1060–1065 (2010).
53. Winkler, J. R. & Gray, H. B. Electron transfer in ruthenium-modified proteins. *Chem Rev* **92**, 369–379 (1992).
54. Low, D., Winkler, J. R., Gray, H. B. Photoinduced Oxidation of Microperoxidase-8: Generation of Ferryl and Cation-Radical Porphyrins. *J Am Chem Soc* **118**, 117-120 (1996).
55. Hartings, M. R. *et al.* Electron tunneling through sensitizer wires bound to proteins. *Coord Chem Rev* **254**, 248–253 (2010).
56. Dmochowski, I. J., Crane, B. R., Wilker, J. J., Winkler, J. R., Gray, H. B. Optical Detection of Cytochrome P450 by Sensitizer-linked Substrates. *Proc Nat Acad Sci USA* **96**, 12987-12990 (1999).
57. Dunn, A. R., Dmochowski, I. J., Winkler, J. R. & Gray, H. B. Nanosecond Photoreduction of Cytochrome P450cam by Channel-Specific Ru-diimine Electron Tunneling Wires. *J Am Chem Soc* **125**, 12450–12456 (2003).
58. Belliston-Bittner, W. *et al.* Picosecond Photoreduction of Inducible Nitric Oxide Synthase by Rhenium(I)–Diimine Wires. *J Am Chem Soc* **127**, 15907–15915 (2005).
59. Ener, M. E., Lee, Y. T., Winkler, J. R., Gray, H. B. & Cheruzel, L. Photooxidation of cytochrome P450-BM3. *Proc Nat Acad Sci USA* **107**, 18783–18786 (2010).

Chapter Two

RUTHENIUM-MODIFIED NITRIC OXIDE SYNTHASE FROM *GEOBACILLUS STEAROTHERMOPHILUS*

2.1 Introduction

Nitric oxide synthases (NOS) are a class of monooxygenase enzymes responsible for the catalytic production of nitric oxide radical (NO). NO is now recognized as an important biological molecule with many roles, such as an endothelial relaxing factor, a protective immunocytotoxin; and it is involved in neurotransmission and apoptosis.[1–3] There are three NOS isoforms found in mammals (mNOS) and NOS-like enzymes have now been discovered in all kingdoms of life, including archaea and bacteria.[4] Bacterial NOSs share remarkably similar three-dimensional structures with their mammalian counterparts. It was initially surprising to find these enzymes in the bacteria themselves in part because NO is produced by macrophages during immune response to *kill* bacteria.[5] The exact biological role for bacterially synthesized NO is still debated, but both *in vitro* and *in vivo* NO production have been demonstrated.[6–8] In all cases, NOS catalyzes the three-electron oxidation of L-arginine (L-Arg) to L-citrulline (L-Cit) and NO in a two-turnover cycle. This reaction proceeds via the stable, enzyme-bound intermediate, N^{ω}-hydroxy-L-arginine (NOHA)[3] (Scheme 2.1).

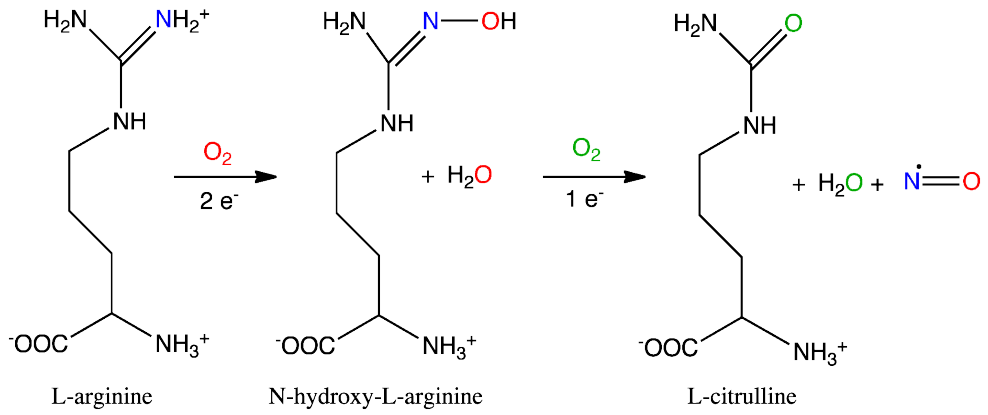

Scheme 2.1 Overall reaction for the NOS-catalyzed production of NO and L-Cit starting with L-Arg, via the intermediate NOHA. The oxygen atom in both NO and L-Cit come from dioxygen; the nitrogen atom in NO is derived from the guanidinium nitrogen in L-Arg.

mNOS functions as a homodimer consisting of an oxygenase domain linked to a reductase domain.[9] The oxygenase domain houses a cysteine-ligated heme, as well as substrate and redox cofactor binding sites that create the active site of the enzyme. The calmodulin-linked reductase domain contains binding sites for flavin adenine dinucleotide (FAD), flavin mononucleotide (FMN), and nicotinamide adenine dinucleotide phosphate (NADPH).[3] A general scheme for proposed full-length NOS domain connectivity and function can be found in chapter one. The reductase domain is the initial source of electrons for catalysis carried out at the oxygenase active site in mNOS. However, with one known exception,[10] all bacterial NOSs lack a dedicated reductase domain; they have been shown to effectively utilize reductase domains from other systems.[4]

The full mechanism by which NOS catalytically produces NO from L-Arg is still unknown,[11] however steps can be borrowed from other members of the cysteine thiolate-ligated heme enzyme superfamily to which it belongs. This family of monooxygenases that also includes chloroperoxidase (CPO) and the well-studied cytochromes P450, activates dioxygen (O_2) to incorporate an oxygen atom into a variety of substrates.[12] The first NOS turnover is a two-electron oxidation of L-Arg resulting in the hydroxylation of a guanidinium nitrogen in a reaction that is nearly identical to that of P450-catalyzed hydroxylation; the second turnover, a one-electron oxidation to form NO and L-Cit, is thought to follow a unique mechanism.[11] The NOS resting state is a six-coordinate ferric-aquo heme with an equilibrium of low- and high-spin states ("mixed-spin"). Substrate binding (L-Arg in the first cycle and NOHA in the second) in the pocket sterically displaces water to form a five-coordinate high-spin ferric state. Ferric NOS is reduced by

one electron originating from the reductase domain to give a ferrous species that can bind O_2. Oxygen binding gives a ferrous-oxy species (often represented as a ferric-superoxide), that is further reduced by one electron supplied by the redox-active cofactor (6R)-5,6,7,8-tetrahydrobiopterin (H_4B, pterin).[13] To date, the next experimentally observed species is the ferric resting state with bound NOHA. The second turnover shares similar steps: reduction, O_2 binding, and reduction by H_4B. From there, the next observed species is the NO-bound ferric heme, which then releases NO. The missing oxygenating intermediates are thought to be a ferryl porphyrin radical cation[14] (analogous to compound I in P450) in the first turnover and either a hydroperoxo ferriheme[15] or Cpd I formed by subsequent protonation/water loss in the second (Figure 2.1).

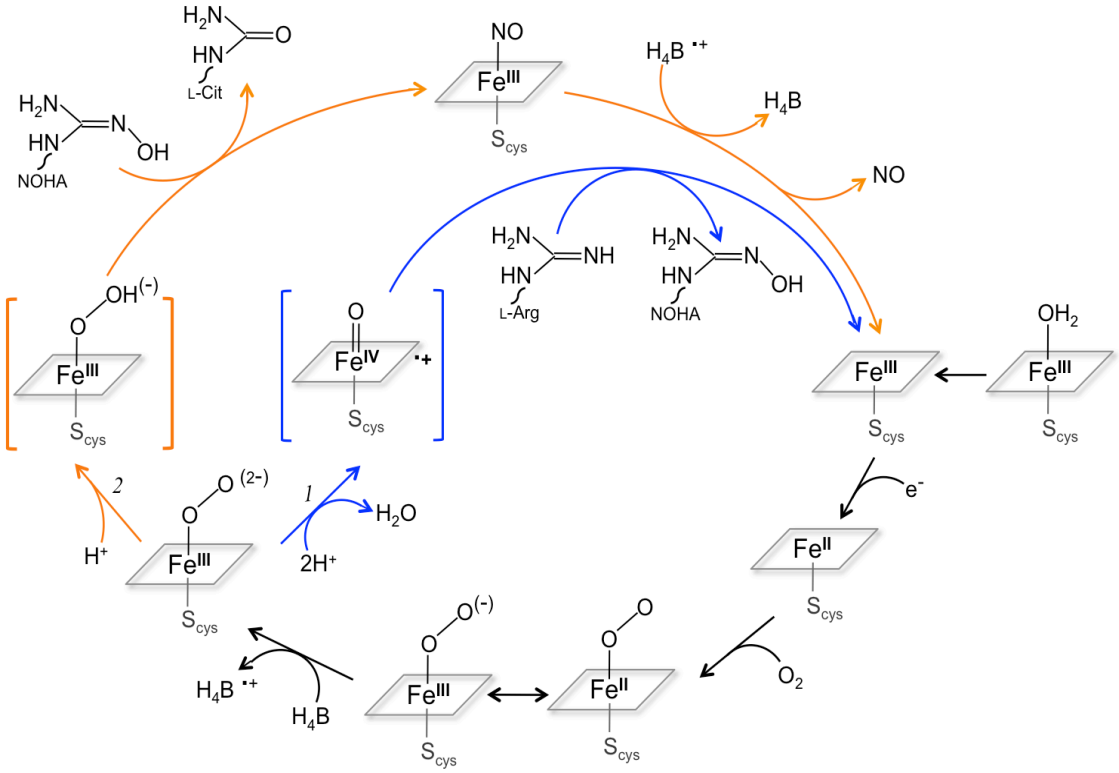

Figure 2.1 Putative mechanism for the catalytic production of NO by NOS enzymes: (1) first turnover formation of NOHA from L-Arg, shown in blue path; (2) second turnover formation of L-Cit and NO radical from NOHA, shown in orange path. The proposed oxygenating intermediates are in brackets.

In general, reactive species with very short lifetimes can only be observed if the reaction initiation is very fast, allowing time for intermediates to accumulate. Additionally, detection methods must be fast enough to "see" these transient species. One way to capture these types of elusive reactive intermediates is through rapid photo-triggered electron transfer (ET), followed by transient absorption (TA) spectroscopy,[16] provided that each reaction component has a unique absorption feature (or a "spectroscopic handle"). The absorption properties of porphyrins, both in small molecule and heme-protein systems, are very sensitive to substrate/ligand binding and oxidation state.[12] Changes in spin state and oxidation state are manifested in pronounced shifts in the Soret region, as well as in the Q-bands of hemes, and these shifts can be used to follow the progress of a given reaction.

The Gray group has developed what is known as "flash-quench" methodology[17] to observe heme-based intermediates. Excitation (the "flash") into the metal-ligand charge-transfer (MLCT) band of ruthenium(II)diimine photosensitizers, such as $[Ru(bpy)_3]^{2+}$ (bpy = 2,2'-bipyridine), creates an excited state ~2.1 eV above the ground state. Introduction of another small-molecule in solution (the "quench") can lead to the formation of either a potent -1.3 V reductant, $[Ru(bpy)_3]^{1+}$, or +1.3 V oxidant, $[Ru(bpy)_3]^{3+}$.[18] From there, electrons can either be injected into or pulled from the heme (Scheme 2.2).

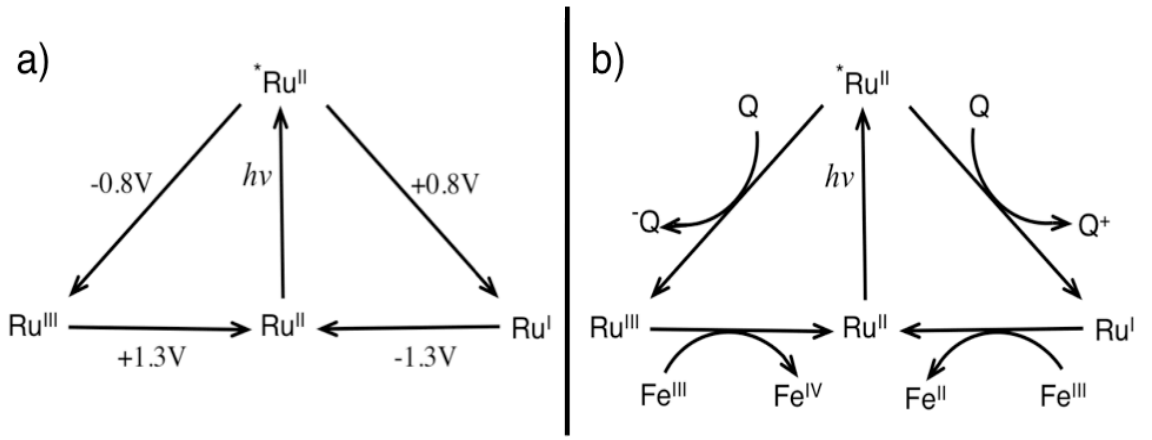

Scheme 2.2 Flash-quench scheme showing both reductive and oxidative quenching routes. a) Reduction potentials are given for $Ru(bpy)_3$ species in aqueous solutions[18] b) Ru represents $Ru(bpy)_3$, Q^+ and Q^- represent oxidative and reductive small molecule quenchers, respectively, Fe represents heme.

Previous work in the Gray group has found success with a flash-quench oxidation scheme using $[Ru(bpy)_3]^{2+}$ in solution which allowed access to Cpd I/II in horseradish peroxidase (HRP)[19] and microperoxidase-8 (MP8).[20] This approach was unsuccessful however, when applied to the more complex enzymes P450 and iNOS as their active sites are much more buried. We have shown that photosensitizers attached to substrate mimics[21–23] can enter the active site and establish electronic communication with the heme; however they block the substrate binding channel preventing access to the full catalytic cycle, as well as excluding H_2O and/or O_2 needed to access Cpd I or II. Recent work with P450-BM3 has overcome these problems by covalently linking a photosensitizer to the surface of the protein, enabling through-bond ET without blocking the substrate channel.[24] Flash-quench experiments using a reversible oxidative quencher led to observation of various porphyrn radical cation intermediates and Fe(IV)-hydroxide (protonated Cpd II). This was the first time a photochemically generated Cpd II has been observed in P450.

In the continued effort to understand the mechanism by which NOS catalytically produces NO, we have chosen to study NOS from the thermostable, nonpathogenic bacterium *Geobacillus stearothermophilus* (gsNOS). gsNOS has a more constrained active site and slightly more compact overall fold as compared with other bacterial NOS-like enzymes, however the three-dimensional structure is remarkably similar to other bacterial NOSs as well as $mNOS_{oxy}$[7] (see chapter one for a more detailed description). The enhanced thermal stability of this enzyme, as well as other unique properties, presents a convenient system to study the catalytic cycle. As gsNOS, like most bacterial NOS-like enzymes, lacks a dedicated reductase domain, we have the opportunity to supply electrons to the active site via a photosensitizer, thus sidestepping the need for a reductase domain entirely. Furthermore, covalent attachment of a ruthenium(II)diimine complex to the surface of the protein would enable electronic communication with the heme without blocking access to the substrate channel.

2.2 Results and Discussion

Preparation of gsNOS Mutant for Labeling

Previous work in the Gray group has exploited surface histidines as labeling sites for various small molecule dyes and photosensitizers used in fluorescence energy transfer and ET experiments.[16] gsNOS contains over a dozen surface exposed His residues, and it was thus determined that covalent labeling via a cysteine was more feasible. There are four native cysteines in gsNOS at positions 76, 161, 227, and 269. The sulfur of Cys76 ligates the heme iron center of the active site and is necessary for heme incorporation and activity. Inspection of space-filling models reveals that Cys161 is thoroughly buried and

was thus left intact. The solvent-exposed residues Cys227 and Cys269 on the other hand, could present a problem in the selective labeling of gsNOS and were mutated to serine to prevent unwanted multiple labeling sites. Position 115 is natively a lysine residue and was determined to be a good candidate for mutagenesis and labeling: it is solvent-exposed, close enough to the heme to provide reasonable electronic communication, and is located on the opposite side from the dimer interface so that the label does not interfere with the active dimer form of the protein (Figure 2.2). The plasmid for the triple mutant K115C/C227S/C269S (referred to as K115C-gsNOS) was constructed by site-directed mutagenesis, expressed in *E. coli*, and purified as described in the materials/methods section.

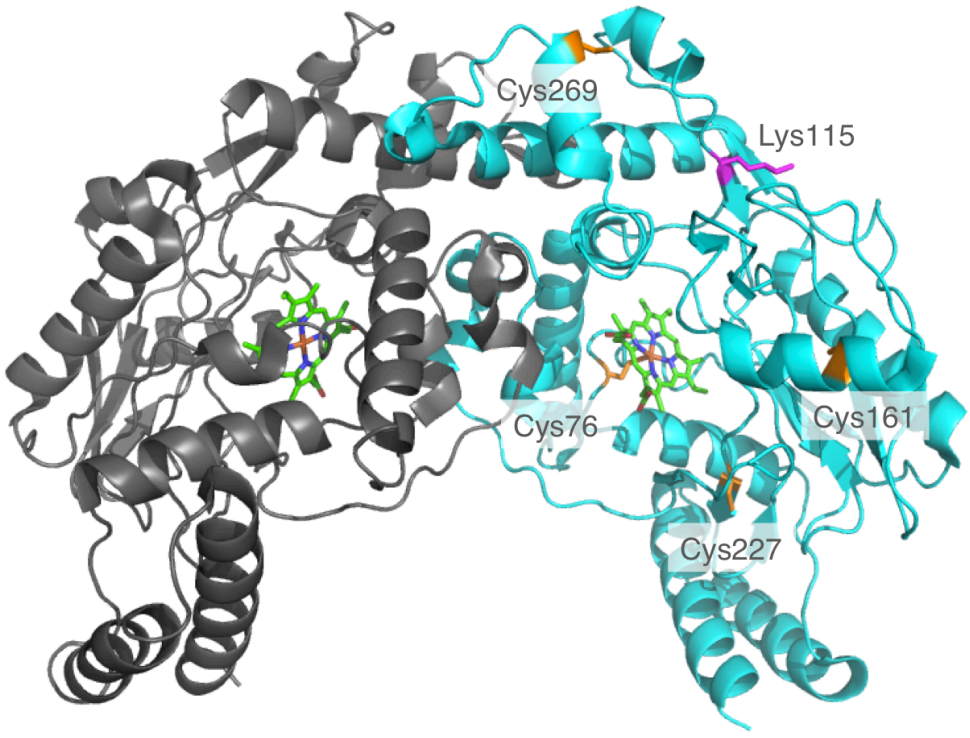

Figure 2.2 Structure of gsNOS dimer highlighting residues important to the labeling construct; the four native cysteines are shown in orange and the lysine to be mutated to cysteine is shown in magenta. PDB code 2FLQ, figure was made with MacPymol 2009.

Labeling with a Ruthenium Photosensitizer

The choice of a photosensitizer for protein labeling is important and one must consider the reduction potential, solubility in aqueous media, synthetic ease, and reactive moiety. Two major strategies have been employed in the Gray group for the attachment of a ruthenium (or rhenium) diimine complex: replacement of a pyridine ligand with the imidazole of a protein histidine residue[16] or reaction of a cysteine sulfur with an alkyl halide linker to form a thioester bond.[25] As mentioned earlier, gsNOS contains a large number of native histidines that could complicate selective labeling reactions. Previous attempts at labeling K115C-gsNOS have proven challenging and unreliable using the photosensitizer $[Ru(bpy)_2(Br\text{-}dmbpy)]^{2+}$ (Br-dmbpy = 4-bromomethyl-4'-methyl-2,2'-bipyridine).[26] It is not entirely clear why this complex was inefficient at labeling, but it is possible that the methyl-bromo group could not gain access to the cyseine due to linker length and/or rigidity or that bromide is not a good enough leaving group. We have had success using a longer and more flexible iodoacetamide linker for the attachment of organic fluorophores, such as Dansyl,[25,27] to various proteins for energy transfer experiments. Recently that same linker scheme was used to attach a $[Ru(bpy)_2(IA\text{-}phen)]^{2+}$ (IA-phen = 5-iodoacetamido-1,10-phenanthroline) complex to the surface of P450-BM3.[24] Due to this previous work and the relatively straightforward synthetic route, we chose to use $[Ru(bpy)_2(IA\text{-}phen)]^{2+}$ for attachment to K115C-gsNOS.

The labeling reaction with $[Ru(bpy)_2(IA\text{-}phen)]^{2+}$ was optimized over several attempts and protocols were established that gave consistent yields of ~60%, with unlabeled protein that can be pooled and saved for relabeling. The covalent attachment proceeds via an S_N2 reaction to give the conjugate, $Ru(II)_{K115C}$-gsNOS (Figure 2.3).

Unreacted label can be easily removed by filtration and the resultant labeled protein purified by fast protein liquid chromatography (FPLC).

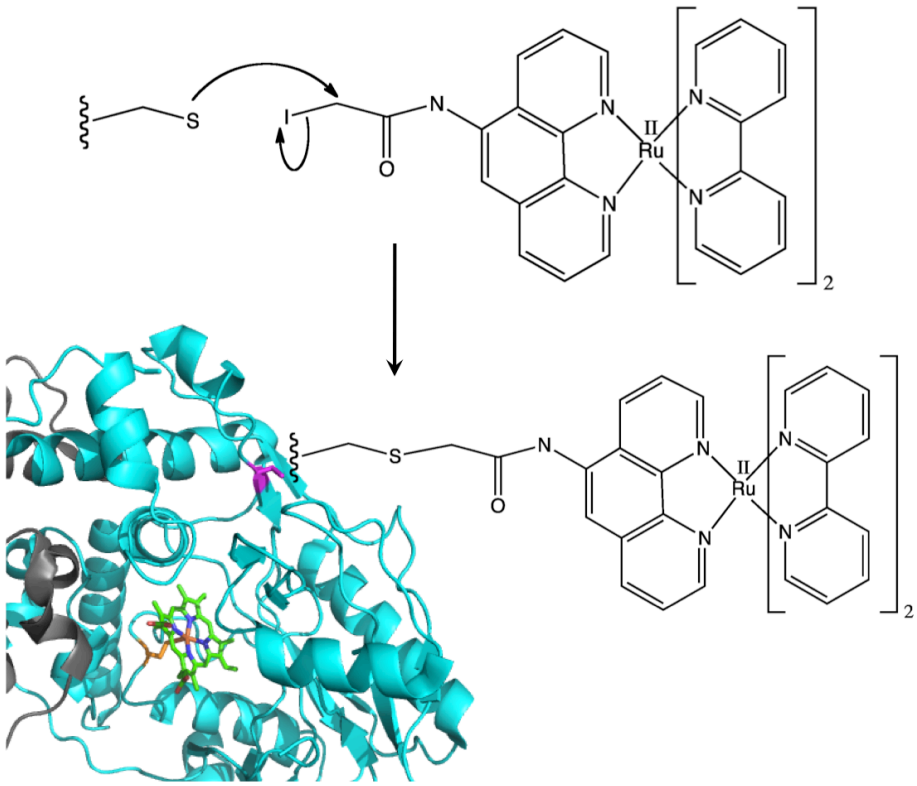

Figure 2.3 Illustration of K115C-gsNOS labeling reaction: the lone pair of electrons on the Cys115 sulfur attack the alkyl halide carbon releasing iodide as the leaving group in an S_N2 reaction to give $Ru(II)_{K115C}$-gsNOS via thioester linkage.

Characterization

The labeled protein, $Ru(II)_{K115C}$-gsNOS, was initially characterized by mass spectrometry (mass spec) and UV-visible absorption spectroscopy (UV-vis). Electrospray ionization (ESI) mass spec reliably confirmed the calculated mass of protein plus label (See Materials/Methods) and the absorption spectrum showed the expected shoulder from the $[Ru(bpy)_2(IA\text{-}phen)]^{2+}$ label (Figure 2.4).

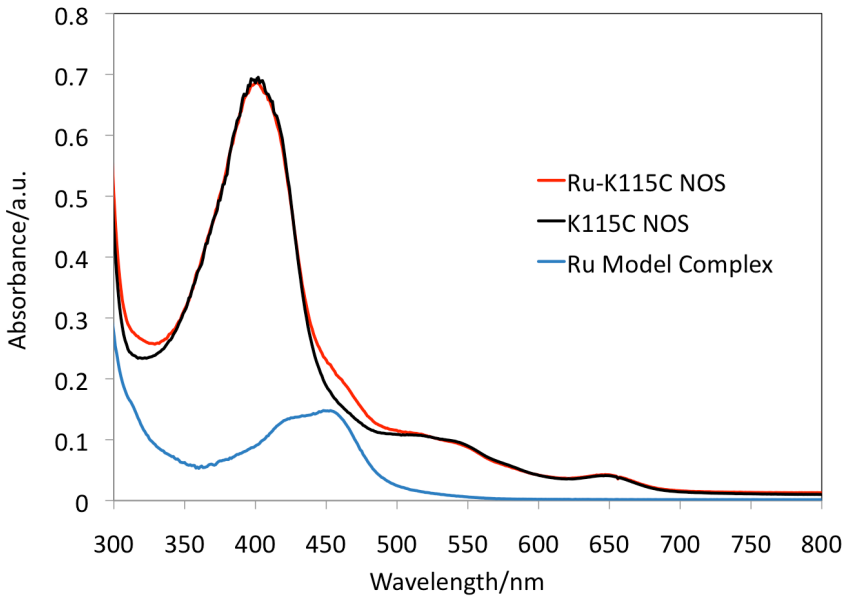

Figure 2.4 UV-visible absorption spectra of unlabeled K115C-gsNOS, $Ru(II)_{K115C}$-gsNOS, and the $[Ru(bpy)_2(IA\text{-}phen)]^{2+}$ model complex. The six-coordinate low-spin ferric-aquo heme Soret maximum is at 403 nm, and the ruthenium photosensitizer-labeled protein shows a shoulder at 450 nm, as expected.

Circular dichroism (CD) spectroscopy is a useful technique to determine the overall helical content and thermal stability of proteins.[28] Chiral objects interact with circularly polarized light, and the resulting changes in polarity are measured as ellipticity. Proteins are made up of chiral amino acids, resulting in chiral tertiary structures such as α-helices and β-sheets, which give signature ellipticity in CD experiments. As a protein unfolds, these tertiary features are lost and result in CD signal changes. Unfolding curves can be generated by addition of a denaturant (urea or guanidinium chloride) or by increasing temperature, and the unfolding midpoint can be used to assess the overall stability of the system. The helical content of both the K115C-gsNOS mutant and the labeled protein, $Ru(II)_{K115C}$-gsNOS, were assessed by CD spectroscopy (Figure 2.5-a). Both proteins share almost identical spectral features in the full wavelength scan,

characteristic of a predominantly α-helical structure. One of the appeals to working with gsNOS is that it is so thermally stable. Wild type (w.t.) gsNOS has a melting midpoint of approximately 80 °C that is about 20 degrees higher than the average bacterial NOS.[7] The temperature-induced unfolding curves (or melting curves) are also quite similar (Figure 2.5-b), both to each other and to w.t. gsNOS. The midpoints for both labeled and unlabeled NOS are approximately 75 °C and are in good agreement with previously measured w.t. gsNOS.[7,26] These experiments were initial indicators that both the mutation and the subsequent labeling did not significantly alter the overall fold and stability of gsNOS.

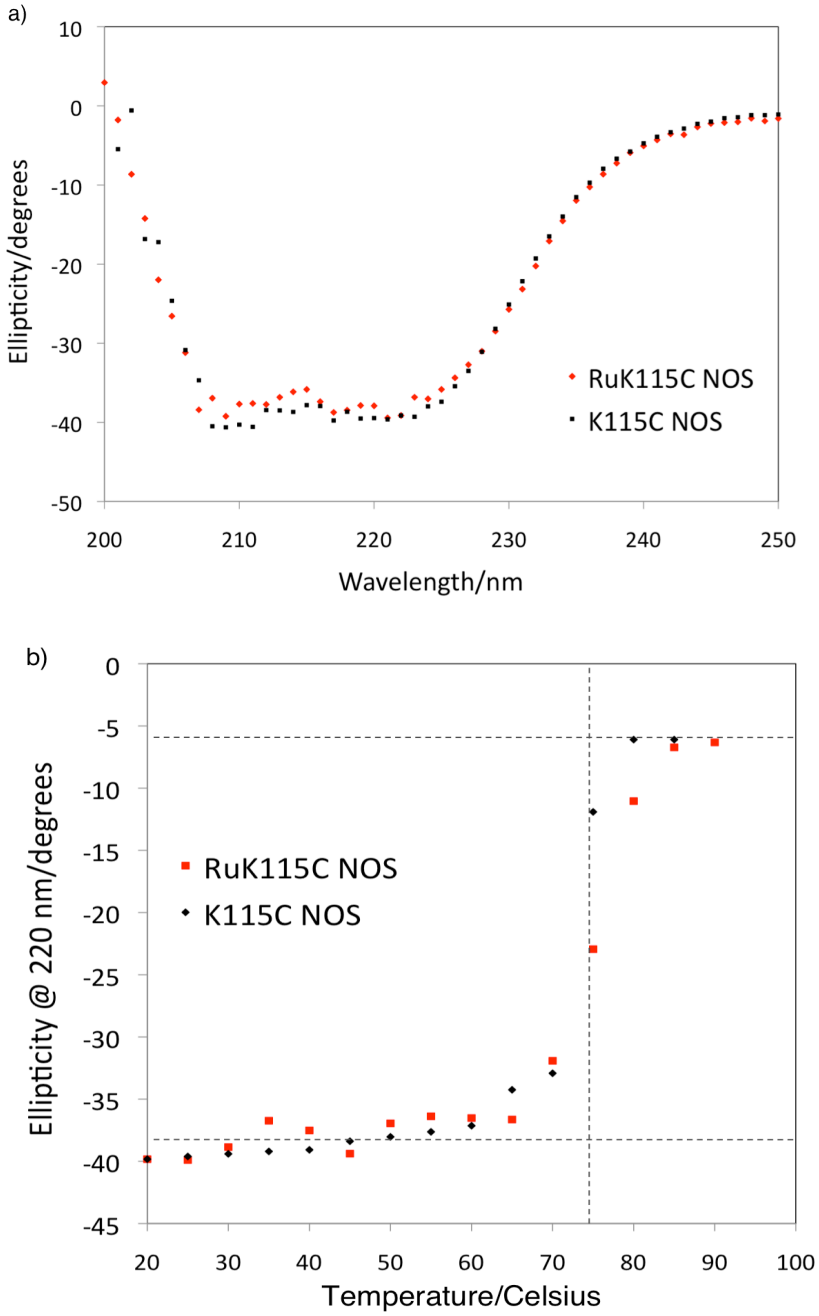

Figure 2.5 Circular dichroism measurements comparing K11C-gsNOS and $Ru(II)_{K115C}$-gsNOS: a) wavelength scan at room temperature to qualitatively assess overall helical content; b) temperature-induced unfolding curves showing nearly identical thermal stability (ellipticity was recorded at the α-helical maximum of 220 nm while increasing temperature).

X-ray Crystallography

In collaboration with the Crane lab at Cornell University, the X-ray crystal structure of our labeled $Ru(II)_{K115C}$-gsNOS conjugate has been solved to a resolution of 2.6 Å. There is one monomer in the unit cell belonging to the space group $P3_221$ with the dimer interface at the edge of the unit cell (as seen in w.t. gsNOS). The structure is remarkably similar to w.t. gsNOS. It maintains all of the major α-helices, including the helical T and lariat at the interface, and the conserved β-winged core.[4] While there are certain areas containing more disorder and flexibility, overlay of the structures indicates that the $[Ru(bpy)_2(A\text{-}phen)]^{2+}$ label does not substantially perturb the overall structure (Figure 2.6).

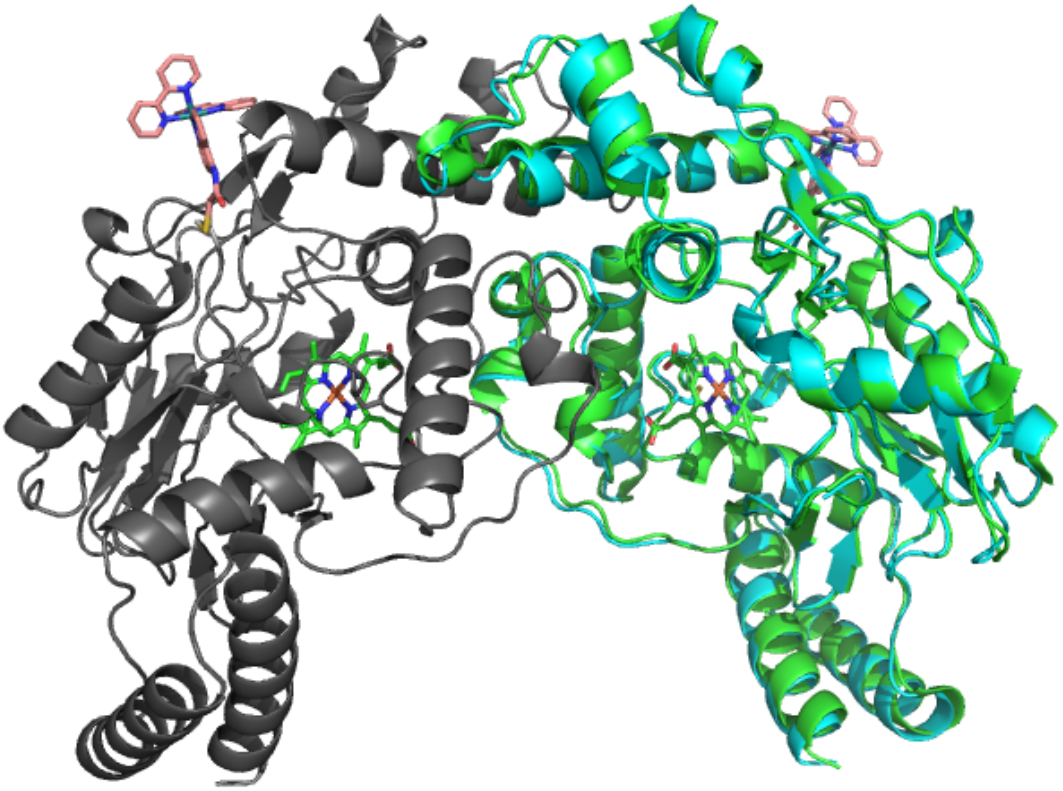

Figure 2.6 Structure of the $Ru(II)_{K115C}$-gsNOS dimer (subunits are in cyan and grey) showing overall fold including helical lariet and T motif. One subunit is overlayed with w.t. gsNOS (shown in green). The $[Ru(bpy)_2(A\text{-}phen)]^{2+}$ label is shown in pink and the hemes in green. w.t. PDB code 2FLQ, figure was made with MacPymol 2009.

There are a few noticeable differences compared to w.t. gsNOS. However it should be noted that the structure of $Ru(II)_{K115C}$-gsNOS was solved in the absence of substrate and cofactor, whereas w.t. gsNOS was solved with L-Arg bound. One area of interest is in the region of Glu248 – Met262, which includes a portion of the H_4B binding site. Since bacterial NOS enzymes lack the typical mammalian H_4B binding loop, the H_4B cofactor is instead bound using key residues at the dimer interface.[4] In gsNOS, these are Phe347 and Trp332 in one subunit and Arg252 and Trp334 on the other. The $Ru(II)_{K115C}$-gsNOS structure shows more flexibility in the loop adjacent to the helix containing Arg252. This seems to manifest as slightly rotated amino acid side chains, including that of Arg252 itself, however the other binding partner in that subunit (Trp334) is basically unchanged (Figure 2.7-a).

Key residues in the heme active site are preserved in the $Ru(II)_{K115C}$-gsNOS structure. The two NO-release "gate" residues (His134 and Ile223)[29,30] are unchanged in this structure as is the conserved Trp70 (see chapter one for relevant discussion). The heme position is mostly the same, however it is slightly rotated and one of the heme propionates is bent out of the plane in this structure (Figure 2.7-b).

Note: Crystals of L-Arg-bound $Ru(II)_{K115C}$-gsNOS have now been grown and a data set has been collected, however the structure has not yet been refined. It will be interesting to see if the presence of substrate imparts more order on the structure.

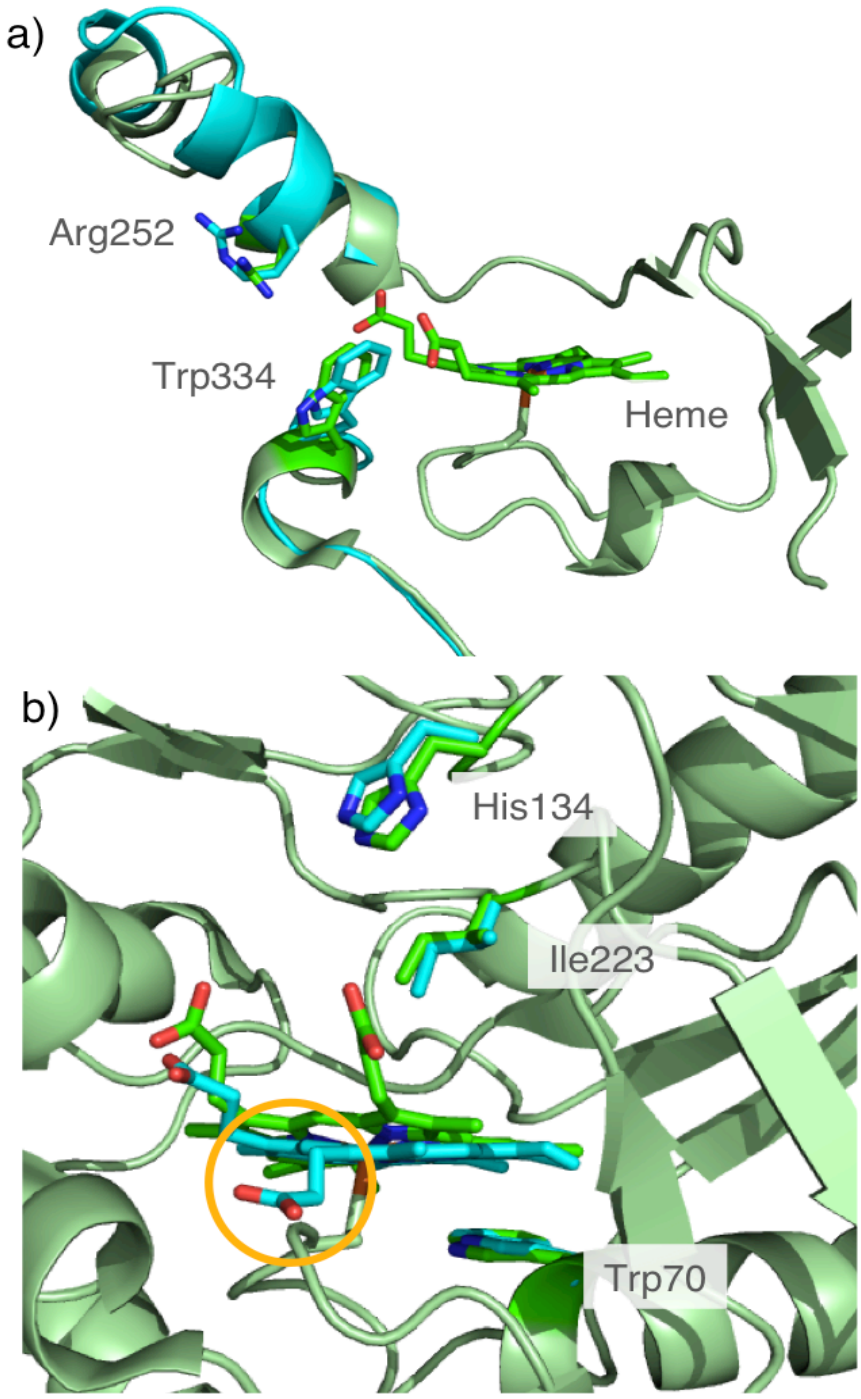

Figure 2.7 Comparison of $Ru(II)_{K115C}$-gsNOS (cyan) and w.t. gsNOS (green) structures. a) Overlay of H_4B binding site showing disorder in the Glu248 – Met262 region causing changes at Arg252 (portions of the protein were removed for clarity) and b) Overlay of the active site showing no significant changes at the "gate residues" or at Trp70. One of the heme propionates is substantially bent out of the plane and is circled in orange. Figure was made with MacPymol 2009.

The distance between the Ru atom of the label and the Fe of the heme is 25 Å (Figure 2.8) in the crystal structure of $Ru(II)_{K115C}$-gsNOS. The label is extended away from the protein surface and the carbonyl of the linker does not appear to hydrogen bond with any of the possible neighboring residues (such as Lys298, R117, or N112). However, there was considerable disorder associated with the $[Ru(bpy)_2(A\text{-}phen)]^{2+}$ label itself, presumably due to the flexible iodoacetamide linker, as seen with ruthenium-labeled P450-BM3[24] (PDB 3NPL). It is possible that the label is actually much closer to the heme when the enzyme is in solution; there is an open pocket containing the surface-exposed Trp243 that could provide π-stacking interactions with the bipyridine or phenanthroline groups of the label. This type of interaction or other hydrophobic interactions with the surface would shorten the Ru-Fe distance by up to 10 Å.

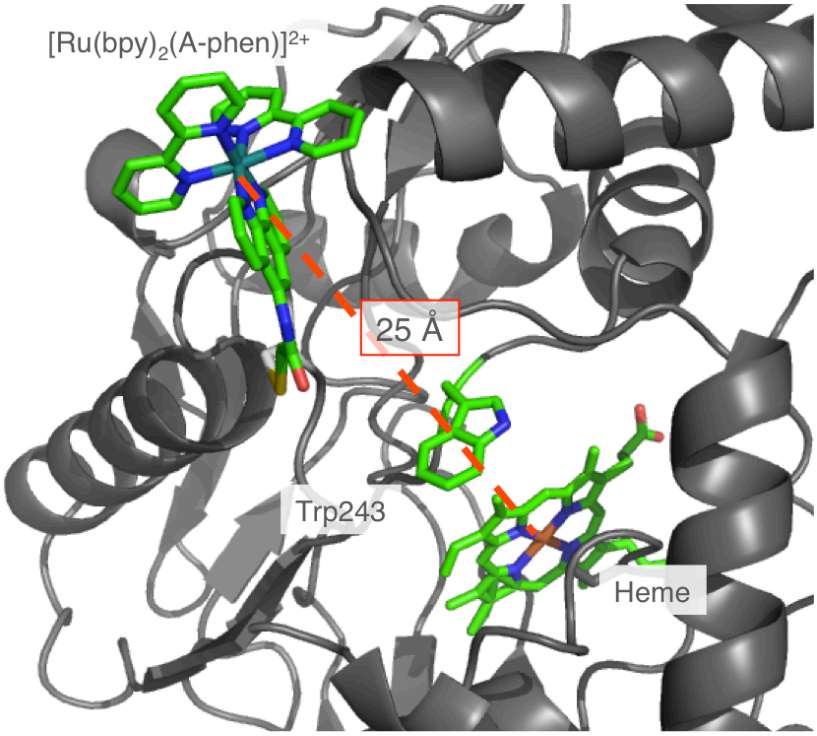

Figure 2.8 Structure of $Ru(II)_{K115C}$-gsNOS. The covalent attachment of $[Ru(bpy)_2(A\text{-}phen)]^{2+}$ at the nonnative Cys115 gives a distance of 25 Å between the Ru and Fe atoms. Surface-exposed Trp243 is shown in green. Figure was made with MacPymol 2009.

Electron Transfer Calculations

The goal of preparing this ruthenium-modified gsNOS was to trigger photoinduced heme reduction and thus bypass the need for a reductase domain. As such, it is worthwhile to briefly discuss the general principles of electron tunneling through proteins to predict ET rates in the present system. Non-adiabatic ET between a redox donor (D) and acceptor (A) held at a fixed distance can be described by the following semi-classical Marcus expression:[31]

$$k_{ET} = \sqrt{\frac{4\pi^3}{h^2 \lambda RT}} H_{AB}^2 \exp\left\{-\frac{(\Delta G^\circ + \lambda)^2}{4\lambda RT}\right\} \qquad \text{(eqn 2.1)}$$

where ΔG° is the driving force and λ is the reorganization parameter that reflects the energy of nuclear reorganization in the charged state. λ is largely affected by the protein fold and can be sufficiently lowered by keeping the redox site buried from aqueous solvent. The electronic coupling matrix element, H_{AB}, is a measure of the strength of interaction between the reactants and products at the transition state and is predicted to decrease exponentially with increasing distance (r) between redox partners:

$$H_{AB}(r) = H_{AB}(r_o)\exp\left\{-\frac{1}{2}\beta(r - r_o)\right\} \qquad \text{(eqn 2.2)}$$

where r_0 is the close-contact D-A distance and β is the distance decay factor describing the ability of a particular medium to facilitate ET. Large values of β result in coupling that is strongly distance dependent (e.g., β = 2.9–4.0 Å^{-1} for ET through a vacuum[32]), whereas small values of β result in D-A coupling interactions that are largely distance independent (e.g., β ~0.4–0.8 Å^{-1} for ET through conjugated polymers[33,34]).

Over the past three decades, the Gray group has been interested in understanding long-distance electron tunneling kinetics in proteins[35] and model systems.[32] ET through

various ruthenium-modified proteins, as well as other media, have been extensively studied and the results can be summarized in tunneling timetables (Figure 2.9). This work allowed very reasonable estimations of λ and β values for ET through proteins.

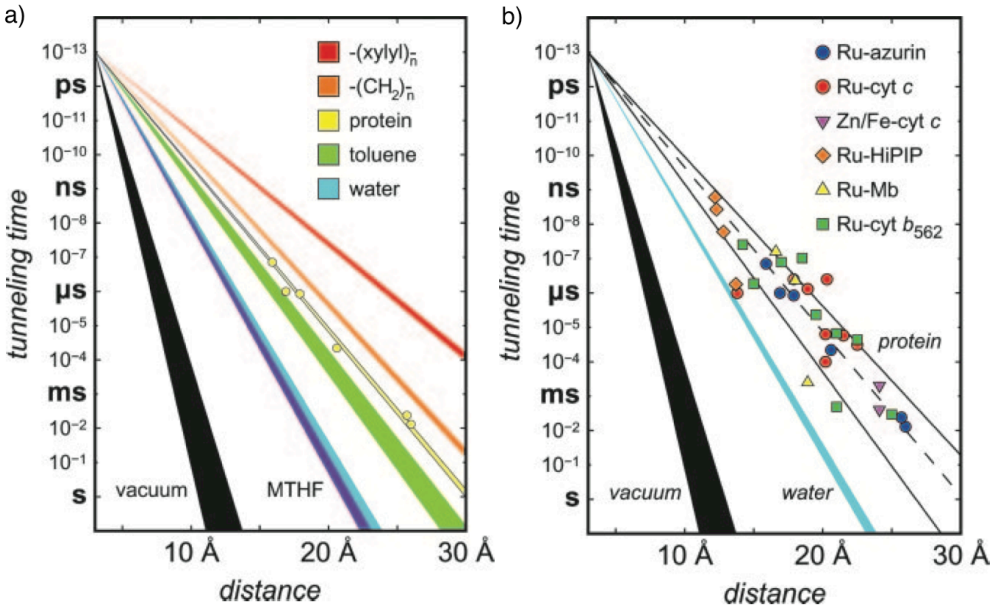

Figure 2.9 a) Timetable for activationless ET in various media. It is of interest to compare the extracted distance dependency (β =1.0 Å^{-1}) of alkane-bridged D-A systems (orange line) with those of proteins; b) Tunneling timetable for intraprotein ET in Ru-modified proteins which fall mainly on the β =1.0 Å^{-1} line. Figure replicated from Gray.[32]

From here we can calculate the rate for heme reduction by Ru(I) in our Ru(II)$_{K115C}$-gsNOS system using the Marcus equation with the estimates β = 1.1 Å^{-1} and λ = 0.8eV.[35] The driving force can be calculated from the reduction potentials for [Ru(bpy)$_2$(A-phen)]$^{2+}$ (estimated from Ru(bpy)$_3$) and K115C-gsNOS (estimated from wild type gsNOS):

$$Ru^{I} \rightarrow Ru^{II} + e^{-}, \quad E° = +1.30 \text{ V } (vs. \text{ NHE})^{18} \qquad \text{(eqn 2.3)}$$

$$Fe^{III} + e^{-} \rightarrow Fe^{II}, \quad E° = -0.360 \text{ V } (vs. \text{ NHE})^{26} \qquad \text{(eqn 2.4)}$$

Taking $\Delta G^{\circ} = +0.940$ V and the Ru-Fe distance of 25 Å from the X-ray crystal structure, we get a rate of $k_{ET} \sim 2.5 \times 10^2$ s^{-1}. However, if we assume that the $[Ru(bpy)_2(A\text{-}phen)]^{2+}$ label is actually tucked in against the protein surface in solution, a Ru-Fe distance of 15–18 Å might be more reasonable. These distances yield a range of rates from $k_{ET} \sim 1.5 \times 10^7$ s^{-1} to $k_{ET} \sim 5.5 \times 10^5$ s^{-1} with time constants (τ_{ET}) from 60 ns to 2 μs. The calculated driving force (ΔG°) and arrangement of redox partners indicates that rapid electron injection is possible to reduce the heme in $Ru(II)_{K115C}$-gsNOS.

2.3 Conclusion

We have used site-directed mutagenesis to install a single surface cysteine at position 115 on gsNOS for selective labeling with $[Ru(bpy)_2(IA\text{-}phen)]^{2+}$. The resultant conjugate, $Ru(II)_{K115C}$-gsNOS, has been characterized in terms of electronic structure and thermal stability. $Ru(II)_{K115C}$-gsNOS has been crystallized and the structure solved to a resolution of 2.6 Å. The crystal structure shows increased flexibility in the H_4B binding region as compared to w.t. gsNOS. One of the heme propionates is bent out of the plane, however the positions of key residues in the active site are unchanged. Overall the structure of $Ru(II)_{K115C}$-gsNOS does not appeared significantly perturbed due to attachment of the $[Ru(bpy)_2(IA\text{-}phen)]^{2+}$ label. While the crystal structure shows a fully extended label-linker with a Ru-Fe distance of 25 Å, a shorter distance is more likely in solution as the label can associate with the protein surface. Electron transfer rates have been estimated depending on actual Ru-Fe distance, with more reasonable rates in the range of $k_{ET} \sim 1.5 \times 10^7$ s^{-1} to $k_{ET} \sim 5.5 \times 10^5$ s^{-1} . With this system in hand, we can photo-

trigger electron injection to reduce the gsNOS heme and explore the biological route of the catalytic cycle.

2.4 Acknowledgements

I am greatly indebted to the following people for help with this project: former student Dr. Charlotte Whited for the initial plasmid construction (used for her gsNOS electrochemistry experiments), Maraia Ener for assistance with the ruthenium label synthesis, and Dr. Sarah Chobot Hokanson in Brian Crane's lab at Cornell for X-ray crystallography.

2.5 Materials and Methods

General

Chemicals were used as purchased unless otherwise noted. All buffers were made with Milli-Q water (18.2 MΩ) and filtered (0.22 μm, Millipore) before use. Molecular biology was carried out using sterile techniques and all media/glassware was prepared by autoclave before use.

Protein Preparation

The w.t. plasmid for gsNOS (pETDuet vector, Novagen) was a generous gift from Professor Brian Crane. The vector encodes for chloramphenicol resistance and a thrombin-cleavable His_6-tag for protein purification. The desired triple mutant K115C/C227S/C269S (K115C-gsNOS) was prepared using site-directed mutagenesis (QuikChange Kit, Stratagene); primers were designed according to standards outlined in the kit and purchased from Operon. The mutant plasmid was transformed into competent

cells for DNA cloning following standard procedure (XL1 Blues, Stratagene) and sequenced (Laragen). The variant was then transformed into BL21 (DE3) competent cells (Invitrogen) and glycerol cell stocks were prepared for later expression.

His_6-K115C-gsNOS was expressed following published procedures for w.t. gsNOS,[7] with minor changes. 3 x 50 mL of culture media (LB and 50 μL of 34 mg/mL stock of chloramphenicol in ethanol) was inoculated from glycerol cell stocks of BL21 (DE3) cells containing the His_6-K115C-gsNOS pETDuet plasmid. After overnight incubation at 37 °C with shaking at 180 rpm, the starter cultures were used to inoculate 9L of media (LB and 1mL/L chloramphenicol stock). After approximately 3 hours of incubation at 37 °C with shaking at 180 rpm, the OD_{600nm} reached 1.0–1.4, and expression was induced with an aqueous solution of iron(III)chloride, isopropyl β-D-1-thiogalactopyranoside (IPTG), and δ-aminolevulinic acid to final media concentrations of 125 mg/L, 100 μM, and 50 mg/L, respectively (*note*— if you make this solution with all three components, make sure to dissolve $FeCl_3$ in water first and let it cool to room temperature before adding IPTG and δ-aminolevulinic acid). After overnight growth (approximately 20 hours), cells were pelleted by centrifugation at 5,000 rpm and then frozen at -20 °C for at least two hours.

His_6-K115C-gsNOS was extracted and purified as follows. Cells were resuspended in 100 mL of lysis buffer (25 mM HEPES, pH 7.5, 5 mM imidazole, 500mM NaCl) along with microspatula tips of four protease inhibitors (Bestatin, Leupeptin, pefabloc SC, and benzamidine). The suspension was sonicated on ice for a total of 10 min (0.5 sec on/0.5 sec off) and centrifuged for two hours at 16,000 rpm. The supernatant was filtered with a 0.22 μm syringe filter (Millipore) and loaded onto an

FPLC nickel-chelating column (3 x 5 mL HisTrap, GE Healthcare). The column was washed with buffer (25 mM HEPES, pH 7.5, 10 mM imidazole, 500 mM NaCl) until absorbance returned to baseline (approximately 100 mL) and His_6-K115C-gsNOS was eluted with a single step (0% –100%) to a buffer containing 300 mM imidazole.

The His_6-tag was cleaved with 100 μL bovine thrombin (Calbiochem, stock prepared according to product instructions) for at least 4 hours at 4 °C with gentle shaking. K115C-gsNOS was concentrated to 2.5 mL via centrifugation using a 30,000 MW cutoff spin filter (Millipore) and loaded onto a size exclusion column (HiLoad 26/60 Superdex 200pg, GE Healthcare). Protein was eluted with a constant flow rate of 1.6 mL/min into 50 mM Tris, pH 7.5, 150 mM NaCl (Figure 2.10). The FPLC fractions were submitted for mass spec, then pooled and concentrated (Figure 2.11). The calculated mass (protein + heme) = 44,490 amu. K115C-gsNOS concentration was determined by absorbance at 400 nm ($\varepsilon \sim 80{,}000\ M^{-1}\ cm^{-1}$).[26]

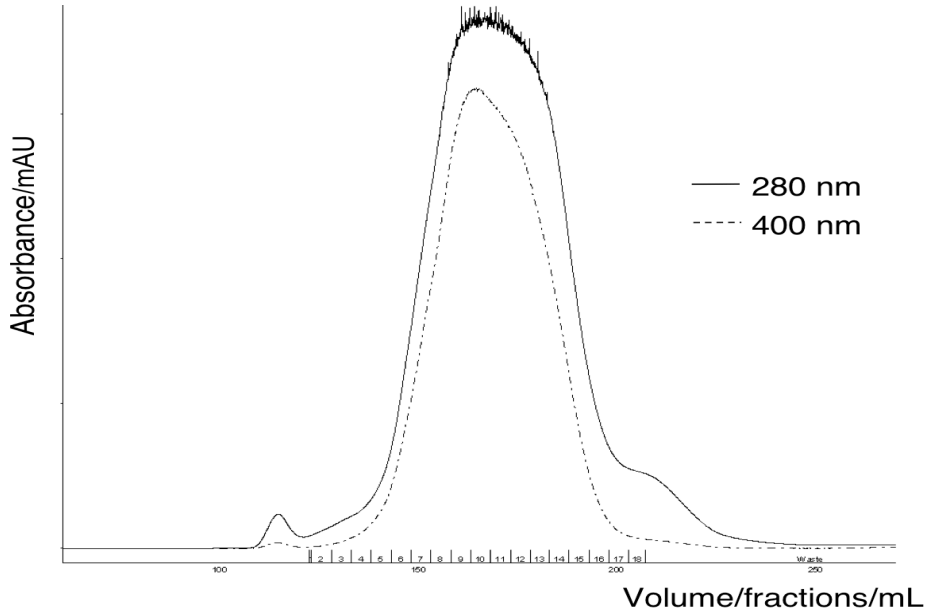

Figure 2.10 Typical FPLC chromatogram for K115C gsNOS purification by size exclusion chromatography; monitored by absorbance at 280 nm (aromatic amino acids) and 400 nm (heme Soret); elution buffer held constant throughout. First and last small shoulders were discarded.

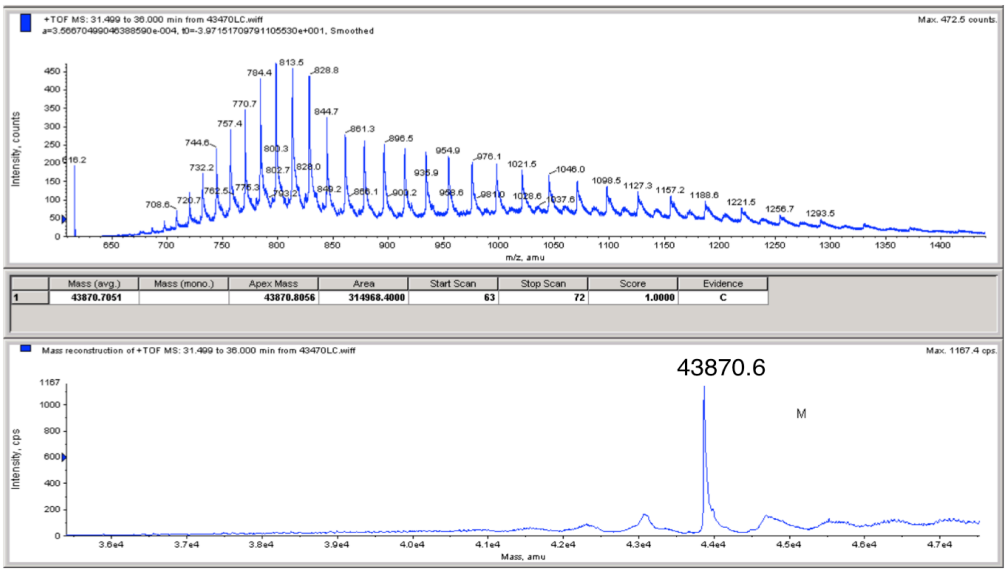

Figure 2.11 ESI mass spectrum of purified K115C gsNOS, showing single major peak at 43,870.6 (*note*— heme does not fly with gsNOS so the calculated mass will add 618 amu).

Synthesis of [Ru(bpy)$_2$(IA-phen)]$^{2+}$ Label

Ruthenium(II) bisbipyridine 5-iodoacetamido-1,10-phenanthroline ([Ru(bpy)$_2$(IA-phen)]$^{2+}$) was synthesized according to published procedure[36] with the following modification: the aminophenanthroline ligand was coordinated to Ru(bpy)$_2$ before converting the amino group to iodoacetamido (Scheme 2.3).

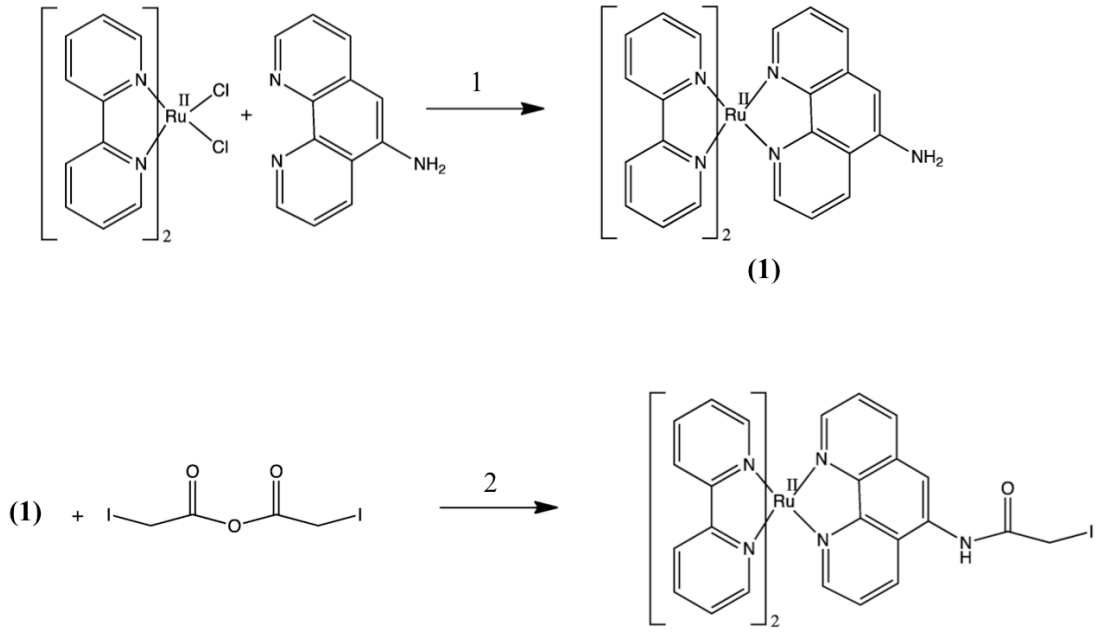

Scheme 2.3 Synthesis of [Ru(bpy)$_2$(IA-phen)]$^{2+}$: 1) reflux in MeOH, 3 hours; 2) CH_3CN, overnight at room temp.

Briefly, Ru(bpy)$_2$Cl$_2$ and a 10-fold molar excess of 5-amino-1,10-phenanthroline were refluxed in methanol for 3 hours with stirring. The solution was cooled to room temperature and filtered. The product **(1)** was precipitated by addition of concentrated aqueous NH_4PF_6 and the solid collected on a medium frit. The solid was washed with water, followed by cold ether, and dried in air. The PF_6 salt of **(1)** and a 5- to 10-fold molar excess of iodoacetic anhydride were dissolved in acetonitrile and allowed to react at room temperature overnight with stirring. The product crystallized and was washed

with cold sodium bicarbonate, followed by water, before being dried over vacuum (*note*: if the product does not crystallize on its own, additional NH_4PF_6 can be added here). The product was a crystalline red powder and only sparingly soluble in water. Mass spec confirmed a molecular weight of 776.1 and showed the characteristic ruthenium isotope pattern. The UV-vis spectrum is nearly identical to that of $Ru(bpy)_3^{2+}$ with characteristic double hump at 428 and 465 nm.[37]

Labeling Reaction

Immediately prior to labeling, K115C-gsNOS was reduced with excess dithiothreitol (DTT) to break up any disulfide bonds that may have formed between the exposed cysteines of two proteins. After 30 min, DTT was removed from the reduced protein with a HiTrap Desalting column (GE Healthcare) into 20 mM Tris buffer, pH 8. The protein concentration was determined by absorbance at 400 nm ($\varepsilon \sim 80{,}000\ M^{-1}\ cm^{-1}$) and then further diluted with Tris to approximately 20 mL of 10 μM protein. An initial spectrum was recorded and the starting absorbance at 450 nm was noted.

Due to the insolubility of the $[Ru(bpy)_2(IA\text{-}phen)]^{2+}$ label, a spatula tip of complex was initially dissolved in 1 mL dimethyl sulfoxide (DMSO) and then brought up to 3 mL with dropwise addition of water. *In the dark* (from here on, any samples containing photosensitizer-labeled protein were stored in the dark and worked with under minimal or red light), the resulting bright yellow/orange solution was slowly added to the protein until the concentration of label reached approximately 10-fold excess of protein. UV-vis spectra were recorded periodically to calculate the concentration of label by difference in absorbance at 450 nm ($\varepsilon \sim 15{,}000\ M^{-1}\ cm^{-1}$, estimated from $Ru(bpy)_3Cl_2$ in water).[38] The reaction was covered in foil and gently shaken for 3 hours at room

temperature (or 4 hours at 4 °C). To stop the reaction, DTT was added and the mixture was desalted again into 20 mM Tris, pH 8 to remove DTT and any unreacted label.

The labeled and unlabeled proteins were separated by FPLC equipped with a FastFlow Q sepharose anion exchange column (5 mL, GE Healthcare) (Figure 2.12). *In the dark,* the protein mixture was loaded onto the column and washed with at least 5 column volumes of starting buffer (or until baseline). The proteins were eluted at a flow rate of 4 mL/min with a salt gradient of 12% –32% elution buffer (20 mM Tris, 1 M NaCl, pH 8) over 360 mL. Absorbance was monitored at 280, 400, and 450 nm. The labeled protein contains a larger overall positive charge and eluted first.

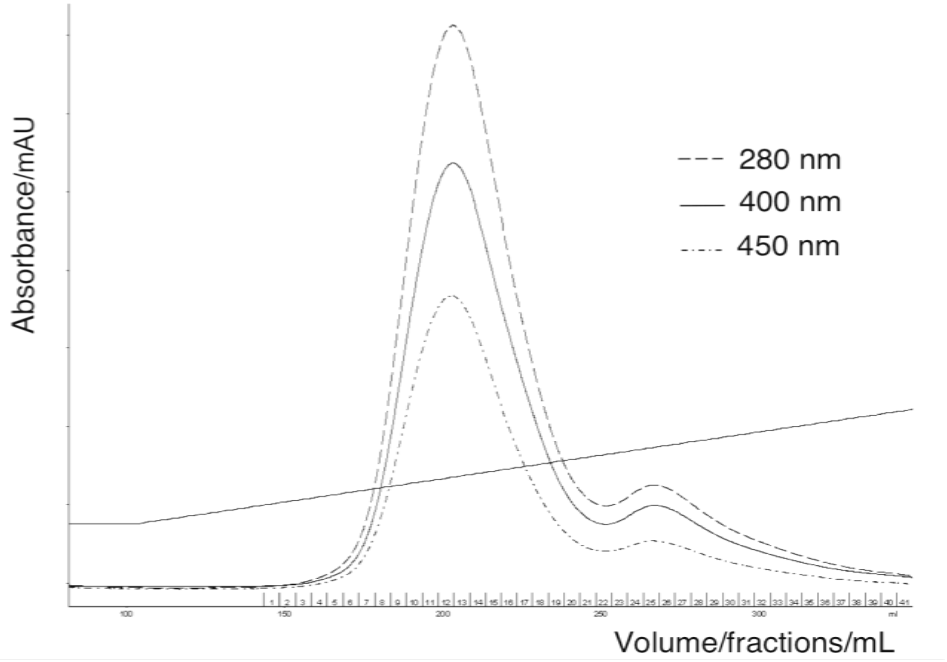

Figure 2.12 Typical FPLC chromatogram for separation of labeled and unlabeled protein using anion exchange chromatography; monitored by absorbance at 280 nm (aromatic amino acids), 400 nm (heme Soret), and 450 nm (Ru label); gradient line = increasing NaCl concentration. First peak corresponds to Ru labeled gsNOS, second peak was mostly unlabeled and kept for later labeling attempts.

UV-vis spectra were recorded for representative fractions, which were then submitted for mass spec analysis before pooling (Figure 2.13). Fractions containing unlabeled protein were pooled and saved for future labeling reactions. Fractions containing pure labeled protein were pooled and concentrated to approximately 100 μM by centrifugation using Amicon spin columns with 30,000 MW cutoff filters. The typical yield for pure $Ru(II)_{K115C}$-gsNOS was 60% –70 %. Stocks were wrapped in foil and stored at 4 °C for use within two weeks or aliquots were flash-frozen in liquid nitrogen and kept at -20 °C for long-term storage.

a)

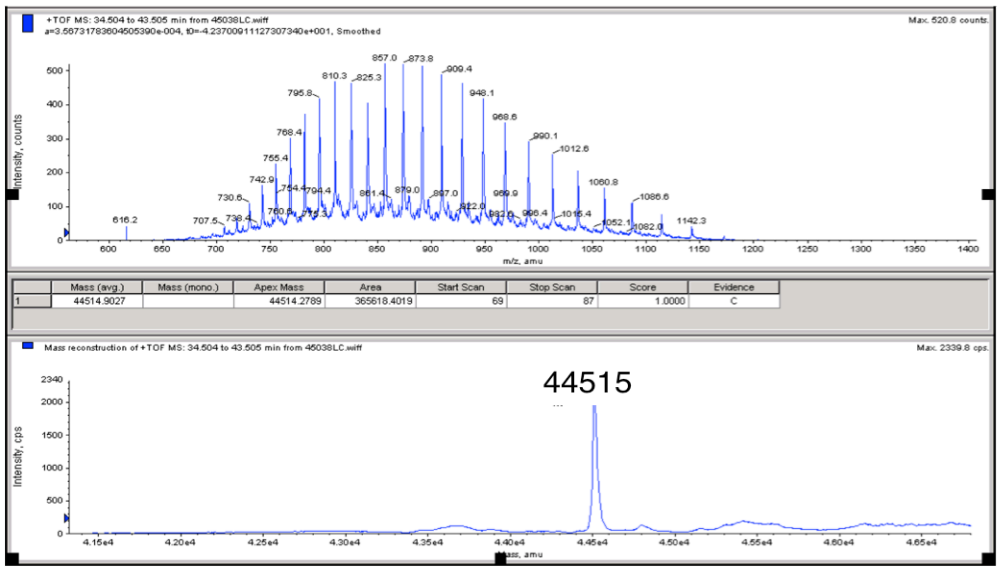

b)

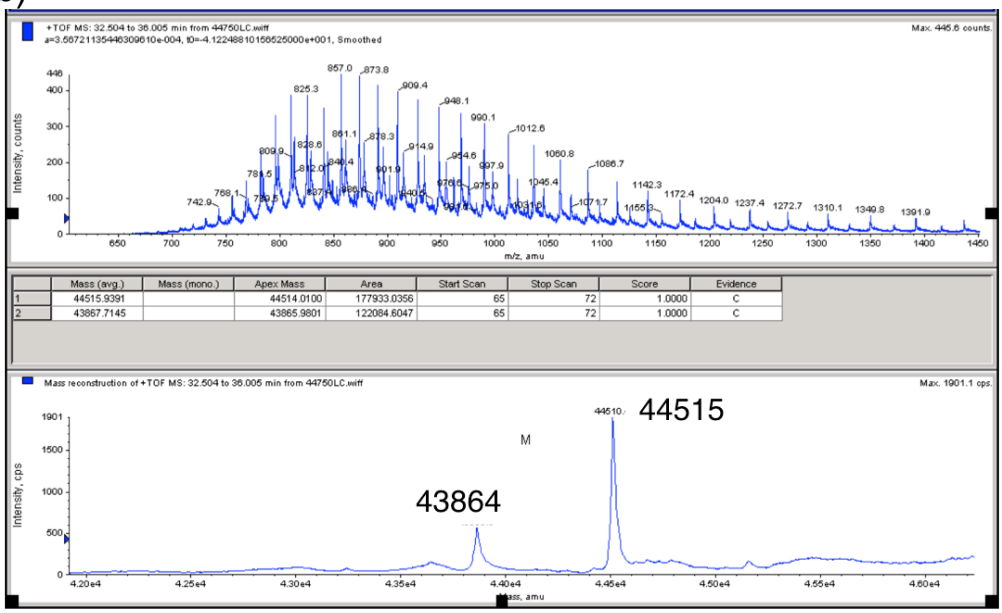

Figure 2.13 ESI mass spectra for $Ru(II)_{K115C}$-gsNOS anion exchange column fractions: a) early fractions showing single peak corresponding to mass of K115C-gsNOS (minus heme) plus the mass of the ruthenium label (minus iodide) (calc ~44,520 amu); b) middle fraction showing mixed peaks for both labeled and unlabeled protein.

Crystallography

Ru(II)$_{K115C}$-gsNOS crystals were grown under the following conditions: 0.5 μL of 400 μM protein in Wizard III (Emerald BioSystems) well condition #31 containing 70 mM sodium acetate buffer, pH 4.7, 70 mM calcium chloride, 30% glycerol, and 17% isopropanol. Crystals took an average of 2–3 weeks to grow (Figure 2.14). Diffraction data were collected at the Cornell High Energy Synchrotron Source (CHESS) beamline A1 (http://www.chess.cornell.edu/chess/west/A1.htm). Due to the high concentration of isopropanol present, no additional cryportectants were used.

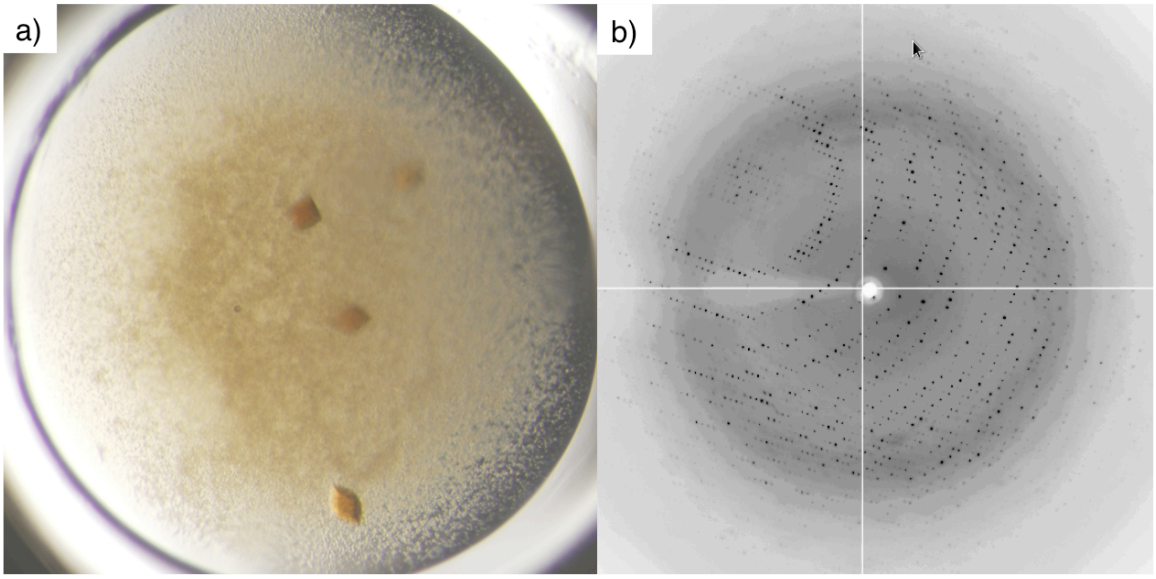

Figure 2.14 Ru(II)$_{K115C}$-gsNOS crystallization a) crystals after 3 weeks b) raw diffraction data collected at CHESS.

Data were indexed and scaled using HKL2000 (HKL Research). Molecular replacement and initial refinement were achieved using Python-based Hierarchical ENvironment for Integrated Xtallography (Phenix) and all other refinement steps using CNS (Crystallography and NMR System, CNSsolve). Data collection and preliminary refinement information are given in Table 2.1.

Table 2.1 Crystallographic data and partial refinement statistics for $Ru(II)_{K115C}$-gsNOS

Wavelength (Å)	0.987
Unit Cell Parameters	
a,b,c (Å)	90.047, 90.047, 112.118
α,β,γ (deg)	90, 90, 120
Space Group	$P3_221$
Diffraction Resolution (Å)	1.98
Refinement Resolution (Å)	2.6
R_{Free}	0.244
R_{Work}	0.241
Completeness	
at 2.6 Å	85 %
at 3.2 Å	100 %

Instrumentation

Protein purification by Fast Protein Liquid Chromatography (FPLC) was carried out using an Akta Purifier from GE Healthcare. Protein mass was recorded using Electrospray Ionization (ESI) spectrometry by the Protein/Peptide MicroAnalytical Laboratory (PPMAL) in the Beckman Institute at the California Institute of Technology. $[Ru(bpy)_2(IA\text{-}phen)]^{2+}$ mass was recorded using a Finnigan LCQ ion trap mass spectrometer. UV-visible absorption spectra were recorded on an Agilent 8453 UV-vis Spectrophotometer; measurements were made in 1 cm pathlength quartz cuvettes (from Starna Cells) and background subtracted using appropriate buffer solutions. Circular dichroism data were acquired using an Aviv Model 62ADS Spectropolarimeter equipped with a thermostated sample holder; measurements were made in 1 mm pathlength cuvettes (Starna Cells).

2.6 References

1. Marletta, M. A. Nitric Oxide Synthase Structure and Mechanism *J Biol Chem* **268**, 12231-12234 (1993).
2. Stuehr, D. J. Update on Mechanism and Catalytic Regulation in the NO Synthases. *J Biol Chem* **279**, 36167–36170 (2004).
3. Alderton, W. K., Cooper, C. E., Knowles, R. G. Nitric Oxide Synthase: Structure, Function, and Inhibition. *Biochem J* **357**, 593-615 (2001).
4. Crane, B. R., Sudhamsu, J. & Patel, B. A. Bacterial Nitric Oxide Synthases. *Annu Rev Biochem* **79**, 445–470 (2010).
5. Moncada, S. & Bolanos, J. P. Nitric oxide, cell bioenergetics and neurodegeneration. *J Neurochem* **97**, 1676–1689 (2006).
6. Adak, S. Direct Evidence for Nitric Oxide Production by a Nitric-oxide Synthase-like Protein from Bacillus subtilis. *J Biol Chem* **277**, 16167–16171 (2002).
7. Sudhamsu, J. Structure and Reactivity of a Thermostable Prokaryotic Nitric-oxide Synthase That Forms a Long-lived Oxy-Heme Complex. *J Biol Chem* **281**, 9623–9632 (2005).
8. Shatalin, K. *et al.* Bacillus anthracis-derived nitric oxide is essential for pathogen virulence and survival in macrophages. *Proc Nat Acad Sci USA* **105**, 1009 (2008).
9. Stuehr, D. Oxygen Reduction by Nitric-oxide Synthases. *J Biol Chem* **276**, 14533–14536 (2001).
10. Agapie, T. *et al.* NO formation by a catalytically self-sufficient bacterial nitric oxide synthase from Sorangium cellulosum. *Proc Nat Acad Sci USA* **106**, 16221–16226 (2009).
11. Zhu, Y. & Silverman, R. B. Revisiting Heme Mechanisms. A Perspective on the Mechanisms of Nitric Oxide Synthase (NOS), Heme Oxygenase (HO), and Cytochrome P450s (CYP450s). *Biochemistry* **47**, 2231–2243 (2008).
12. Sono, M., Roach, M. P., Coulter, E. D., Dawson, J. H., Heme-Containing Oxygenases. *Chem Rev* **96**, 2841-2887 (1996).
13. Wei, C.-C., Crane, B. R. & Stuehr, D. J. Tetrahydrobiopterin Radical Enzymology. *Chem Rev* **103**, 2365–2384 (2003).
14. Davydov, R. *et al.* EPR and ENDOR Characterization of Intermediates in the Cryoreduced Oxy-Nitric Oxide Synthase Heme Domain with Bound l-Arginine or N G Hydroxyarginine. *Biochemistry* **41**, 10375–10381 (2002).
15. Woodward, J. J., Chang, M. M., Martin, N. I. & Marletta, M. A. The Second Step of the Nitric Oxide Synthase Reaction: Evidence for Ferric-Peroxo as the Active Oxidant. *J Am Chem Soc* **131**, 297–305 (2009).
16. Winkler, J. R. & Gray, H. B. Electron transfer in ruthenium-modified proteins. *Chem Rev* **92**, 369–379 (1992).
17. Chang, I. J., Gray, H. B. & Winkler, J. R. High-driving-force electron transfer in metalloproteins: intramolecular oxidation of ferrocytochrome c by Ru (2, 2'-bpy) 2 (im)(his-33) 3+. *J Am Chem Soc* **113**, 7056–7057 (1991).
18. Huynh, M. H. V., Dattelbaum, D. M. & Meyer, T. J. Exited state electron and energy transfer in molecular assemblies. *Coord Chem Rev* **249**, 457–483 (2005).
19. Berglund, J., Pascher, T., Winkler, J. R., Gray, H. B. Photoinduced Oxidation of Horseradish Peroxidase. *J Am Chem Soc* **119**, 2464-2469 (1997).

20. Low, D., Winkler, J. R., Gray, H. B. Photoinduced Oxidation of Microperoxidase-8: Generation of Ferryl and Cation-Radical Porphyrins. *J Am Chem Soc* **118**, 117-120 (1996).
21. Dmochowski, I. J., Crane, B. R., Wilker, J. J., Winkler, J. R., Gray, H. B. Optical Detection of Cytochrome P450 by Sensitizer-linked Substrates. *Proc Nat Acad Sci USA* **96**, 12987-12990 (1999).
22. Dunn, A. R., Dmochowski, I. J., Winkler, J. R. & Gray, H. B. Nanosecond Photoreduction of Cytochrome P450cam by Channel-Specific Ru-diimine Electron Tunneling Wires. *J Am Chem Soc* **125**, 12450–12456 (2003).
23. Belliston-Bittner, W. *et al.* Picosecond Photoreduction of Inducible Nitric Oxide Synthase by Rhenium(I)−Diimine Wires. *J Am Chem Soc* **127**, 15907–15915 (2005).
24. Ener, M. E., Lee, Y. T., Winkler, J. R., Gray, H. B. & Cheruzel, L. Photooxidation of cytochrome P450-BM3. *Proc Nat Acad Sci USA* **107**, 18783–18786 (2010).
25. Pletneva, E. V., Gray, H. B. & Winkler, J. R. Many Faces of the Unfolded State: Conformational Heterogeneity in Denatured Yeast Cytochrome c. *J Mol Biol* **345**, 855–867 (2005).
26. Whited, C. A. Tuning Nitric Oxide Synthase: Investigating the Thiolate 'Push' and NO Release; PhD Thesis; California Institute of Technology, Pasadena, 2011.
27. Pletneva, E. V., Gray, H. B. & Winkler, J. R. Snapshots of cytochrome c folding. *Proc Nat Acad Sci USA* **102**, 18397 (2005).
28. Sreerama, N., Venyaminov, S. Y. U. & Woody, R. W. Estimation of the number of alpha-helical and beta-strand segments in proteins using circular dichroism spectroscopy. *Protein Sci* **8**, 370–380 (1999).
29. Pant, K., Bilwes, A. M., Adak, S., Stuehr, D. J. & Crane, B. R. Structure of a Nitric Oxide Synthase Heme Protein from Bacillus subtilis. *Biochemistry* **41**, 11071–11079 (2002).
30. Whited, C. A. *et al.* Gating NO Release from Nitric Oxide Synthase. *J Am Chem Soc* **134**, 27–30 (2012).
31. Marcus, R. A. & Sutin, N. Electron transfers in chemistry and biology. *Biochim Biophys Acta* **811**, 265–322 (1985).
32. Gray, H. B. & Winkler, J. R. Long-range electron transfer. *Proc Nat Acad Sci USA* **102**, 3534 (2005).
33. Helms, A., Heiler, D. & McLendon, G. Electron transfer in bis-porphyrin donor-acceptor compounds with polyphenylene spacers shows a weak distance dependence. *J Am Chem Soc* **114**, 6227–6238 (1992).
34. Wenger, O. S. Electron Tunneling Through Organic Molecules in Frozen Glasses. *Science* **307**, 99–102 (2005).
35. Gray, H. B. & Winkler, J. R. Electron tunneling through proteins. *Q Rev Biophys* **36**, 341–372 (2003).
36. Castellano, F. N., Dattelbaum, J. D., Lakowicz, J. R. Long-Lifetime Ru(II) Complexes as Labeling Reagents for Sulfhydryl Groups. *Anal Biochem* **255,** 165-170 (1998).
37. Felix, F., Ferguson, J., Guedel, H. U. & Ludi, A. The electronic spectrum of tris (2, 2'-bipyridine) ruthenium (2+). *J Am Chem Soc* **102**, 4096–4102 (1980).

38. Juris, A., Balzani, V., Barigelletti, F; et al. Ru(II) Polypyridine Complexes: Photophysics, Photochemistry, Electrochemistry, and Chemiluminescence *Coord Chem Rev* **84**, 85-277 (1988).

Chapter Three

PHOTOREDUCTION OF RUTHENIUM-MODIFIED NITRIC OXIDE SYNTHASE FROM *GEOBACILLUS STEAROTHERMOPHILUS*

3.1 Introduction

Nitric oxide (NO)[1,2] is a biological signaling molecule produced by a class of enzymes aptly named nitric oxide synthases (NOS).[3] There are three NOS isoforms found in mammals (mNOS),[4] and NOS-like enzymes have now been discovered in all kingdoms of life, including archaea and bacteria.[2] NOS catalyzes the five-electron oxidation of L-arginine (L-Arg) to L-citrulline (L-Cit) and NO in two turnovers, proceeding via the stable, enzyme-bound intermediate, N^{ω}-hydroxy-L-arginine (NOHA).[5] The overall reaction is summarized in Scheme 3.1.

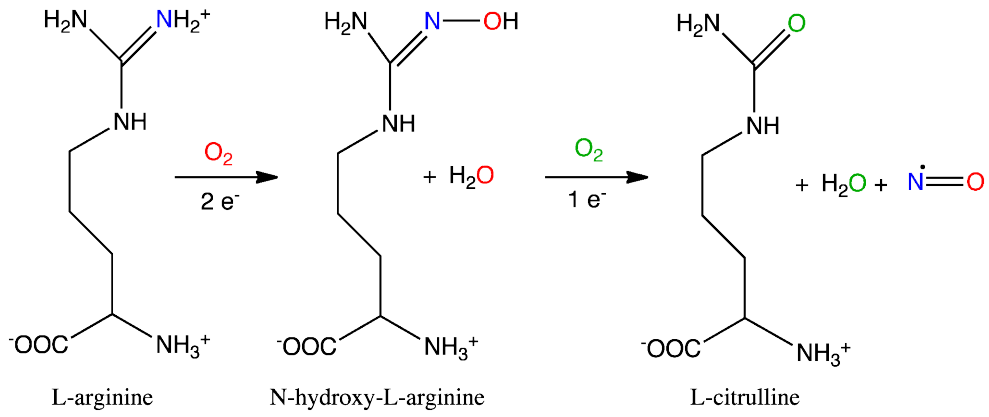

Scheme 3.1 Overall reaction for NOS-catalyzed production of NO and L-Cit starting with L-Arg, via the intermediate NOHA. The oxygen atom in both NO and L-Cit come from dioxygen; the nitrogen atom in NO is derived from the guanidinium nitrogen in L-Arg.

All isoforms of NOS function as homodimers and share nearly identical active sites containing a cysteine-ligated heme, as well as substrate and redox cofactor binding sites. However there are some noteworthy differences between mNOS and bacterial NOS. The most striking difference is that mNOSs have a linked reductase domain,[6] but all but one bacterial NOS lack any dedicated NADPH-dependent reductase domain.[7] Details about the domains of mNOS and structural differences in bacterial NOS are described in chapter one of this thesis.

Some of the discrete steps by which NOS produces NO from L-Arg are still unknown,[4] however steps can be borrowed from other members of the cysteine thiolate-ligated heme enzyme superfamily to which it belongs. This family of monooxygenases includes chloroperoxidase (CPO) and the well-studied cytochromes P450. Like NOS, these enzymes activate dioxygen (O_2) to incorporate an oxygen atom into a variety of substrates.[8] The first NOS turnover is a two-electron oxidation of L-Arg resulting in the hydroxylation of a guanidinium nitrogen to yield NOHA in a reaction that is reminiscent of P450-catalyzed hydroxylations. The second turnover, a one-electron oxidation to form NO and L-Cit, is thought to follow a unique mechanism.[9] The NOS resting state is a six-coordinate ferric-aquo heme with an equilibrium of low- and high-spin states ("mixed-spin"). Substrate binding (L-Arg in the first cycle and NOHA in the second) in the pocket sterically displaces water to form a five-coordinate high-spin ferric state. Ferric NOS is reduced by one electron from the reductase domain to give a ferrous species that can bind O_2. Oxygen binding gives a ferrous-oxy species (often represented as a ferric-superoxide), that is further reduced by one electron supplied by the redox-active cofactor (6R)-5,6,7,8-tetrahydrobiopterin (H_4B).[10] To date, the next experimentally observed species is the ferric resting state with bound NOHA. The second turnover shares similar steps: reduction, O_2 binding, and reduction by H_4B. From there, the next observed species is the NO-bound ferric heme, which then releases NO. The missing oxygenating intermediates are thought to be a ferryl porphyrin radical cation[11] (analogous to compound I in P450) in the first turnover and either a hydroperoxo ferriheme[12] or Cpd I formed by subsequent protonation/water loss in the second[11] (Figure 3.1).

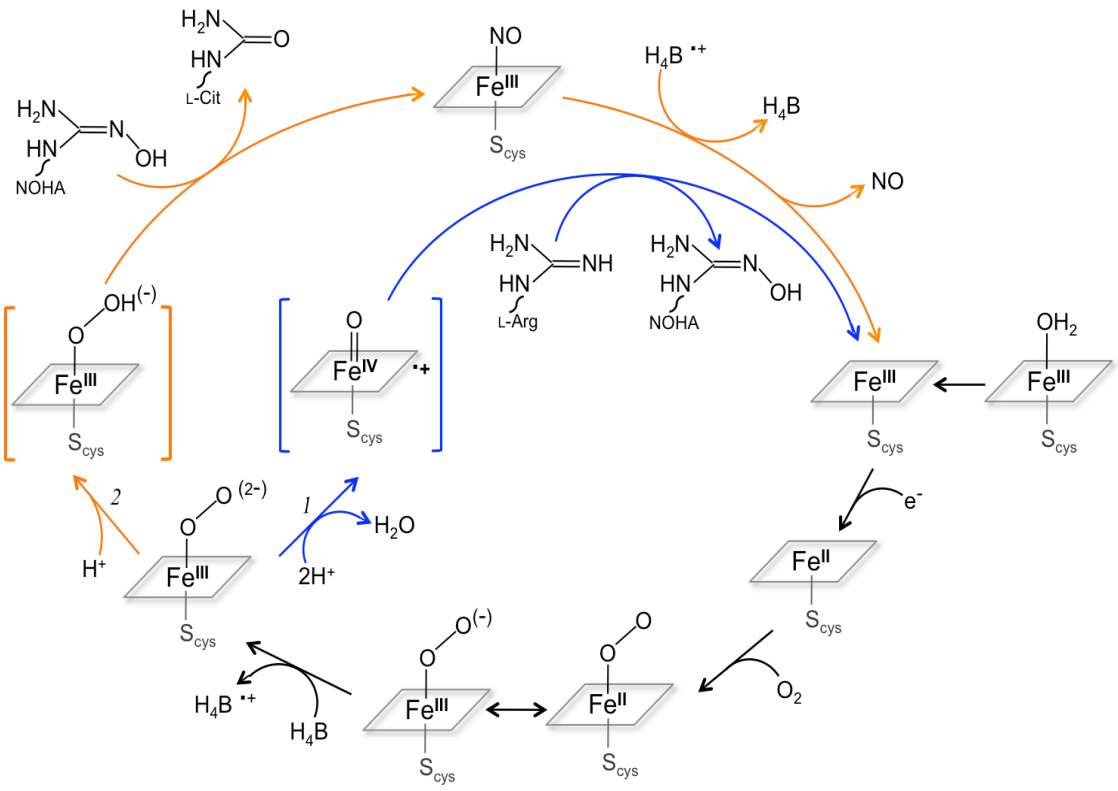

Figure 3.1 Putative mechanism for the catalytic production of NO by NOS enzymes: (1) first turnover formation of NOHA from L-Arg, shown in blue path; (2) second turnover formation of L-Cit and NO radical from NOHA, shown in orange path. The proposed oxygenating intermediates are shown in brackets.

In general, reactive species with very short lifetimes can only be observed if the reaction initiation is very fast, allowing time for intermediates to accumulate. Additionally, detection methods must be fast enough to "see" these transient species. One way to capture these types of elusive reactive intermediates is through phototriggered electron transfer (ET), followed by transient absorption (TA) spectroscopy,[13] provided that each reaction component has a unique "spectroscopic handle," such as an absorption feature. The absorption properties of porphyrins, both in small molecule and heme-protein systems, are very sensitive to substrate/ligand binding and oxidation state.[8] Changes in spin state and oxidation state are manifested in pronounced shifts in the Soret

region and in the Q-bands of hemes, and these shifts can be used to follow the progress of a given reaction. For example, the w.t. gsNOS resting state is a six-coordinate, mixed-spin heme with water occupying the 6th site in the distal pocket and the Soret maximum is at 403 nm. Introduction of the L-Arg substrate displaces the water resulting in a five-coordinate, high spin complex and the Soret band sharpens and shifts to 399 nm. Chemical reduction to give the five-coordinate ferrous species results in a red-shifted Soret maximum at 415 nm (Figure 3.2).[14] These species have all been prepared under steady state conditions providing convenient spectroscopic handles with which to watch the cycle in action. Transient measurements involve exciting the sample with a laser pulse while simultaneously probing with white light to give time-resolved absorption information. These experiments can be set up to either detect the entire spectrum at a fixed time delay after excitation or to measure absorbance as a function of time at a single wavelength.

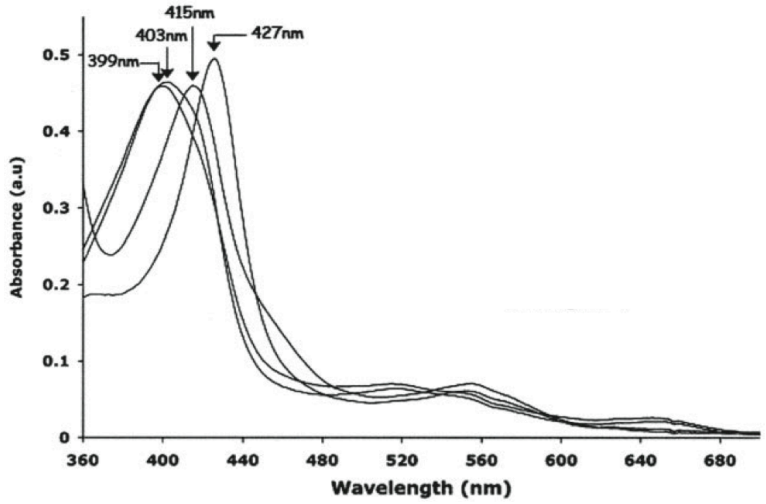

Figure 3.2 UV-visible absorption of wild type gsNOS showing characteristic Soret shifts upon substrate binding and changes in oxidation state. Soret maxima for substrate-free ferric state (403 nm), L-Arg-bound ferric (399 nm), imidazole-bound ferric (427 nm), and chemically reduced ferrous (415 nm). Figure replicated from Sudhamsu.[14]

As described in chapter one, "flash-quench" methodology can be employed to photoinduce reduction or oxidation.[15] Briefly, laser excitation (the "flash") into the metal-ligand charge-transfer (MLCT) band of a ruthenium(II)diimine photosensitizer creates an excited state approximately 2.1 eV above the ground state. This excited state can be "quenched" by an appropriate small molecule in solution yielding either a potent -1.3 V reductant, $[Ru(bpy)_3]^{1+}$, or +1.3 V oxidant, $[Ru(bpy)_3]^{3+}$,[16] that can then inject or extract electrons from the system of interest (in this case, gsNOS heme). The resultant reduced or oxidized heme will have a shifted Soret band (Figure 3.2). TA data collected at a particular wavelength in the Soret region over time can show either a signal increase (positive change in optical density, $\Delta OD > 0$) or a signal decrease (often referred to as a "bleach," $\Delta OD < 0$). Carefully fitting these signal changes to kinetics models can yield valuable information about the rates of individual steps in a given reaction.

Researchers in the Gray group have successfully observed the ferryl porphyrin radical cation (Cpd I) and ferryl species (Cpd II) in both horseradish peroxidase (HRP)[17] and microperoxidase-8 (MP8)[18] using oxidative flash-quench techniques with $[Ru(bpy)_3]^{2+}$ in solution. Applications of this technique to P450 and iNOS were unsuccessful probably because of weak electronic coupling between the solution photosensitizer and the much more buried hemes of these enzymes. Subsequent studies with photosensitizers linked to substrate mimics were successful in heme photoreduction.[19–21] These "wires" penetrate the substrate-binding channels to engage in ET with the active site, however they effectively block the distal pocket, preventing access to later steps in the catalytic cycle, as well as H_2O/O_2 binding necessary to access Cpd I.

Recent work with P450-BM3 circumvented the aforementioned problems by covalently attaching a Ru(II)diimine photosensitizer to the protein surface, enabling through-bond ET without blocking the substrate channel.[22] Oxidative flash-quench was used to rapidly pull an electron from the Fe(III) resting state, generating one-electron oxidized porphyrin radical cation intermediates. TA spectroscopy was used to observe these transient species, allowing the assignment of one high-valent intermediate as Fe(IV)-hydroxide (protonated Cpd II). This was the first time a photogenerated Cpd II has been seen in P450. The kinetics of formation and disappearance of these intermediates were complex over the microsecond to second range. Singular value decomposition analysis of the TA data pointed to at least five distinct phases (Figure 3.3-a), suggesting that six species form after laser excitation. The first and second were identified as the *Ru(II)-Fe(III) excited state and the oxidatively quenched Ru(III)-Fe(III) species, respectively. The final species was assigned to the original Ru(II)-Fe(III) resting state, leaving three distinct intermediates to be determined by modeling. A scheme for the sequential kinetics model used for the heme oxidation of Ru(II)-P450-BM3 is shown in Figure 3.3-b.

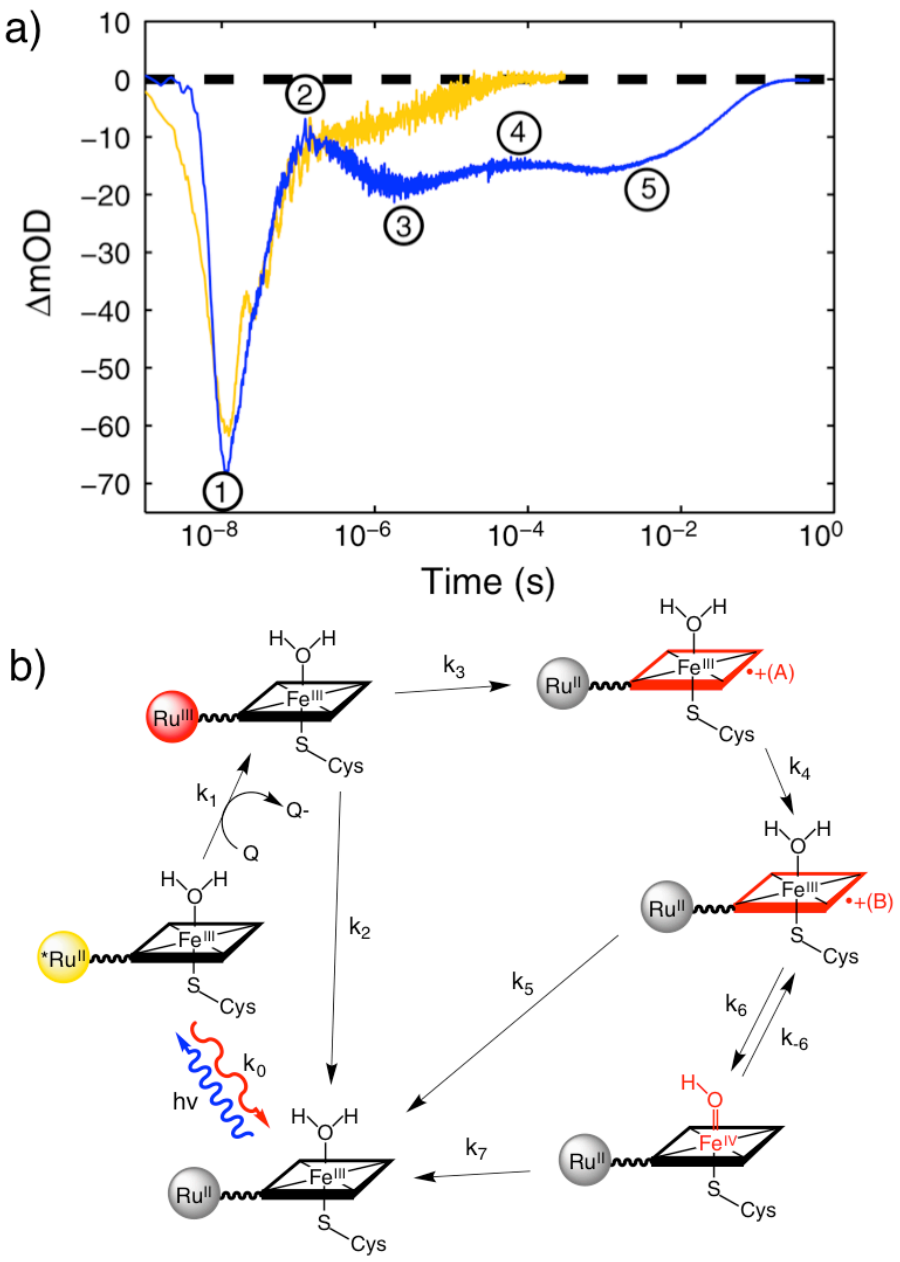

Figure 3.3 Photogenerated formation of compound II in P450-BM3 a) Representative single-wavelength TA data at 420 nm for Ru(II)-Fe(III)P450 (blue) and model complex (yellow), both with oxidative quencher. Circled numbers correspond to the beginning of each phase. b) Diagram of the model for photochemical heme oxidation used in TA kinetics analysis. Figure replicated from Ener.[22]

Taking a page from the P450 book, we have used site-directed mutagenesis to install a single surface cysteine at position 115 in gsNOS for selective labeling with $[Ru(bpy)_2(IA\text{-}phen)]^{2+}$ (where bpy = 2,2'-bipyridine and IA-phen = 5-iodoacetamido-1,10-phenanthroline). The resultant conjugate, $Ru(II)_{K115C}$-gsNOS, has been characterized in terms of electronic structure and thermal stability. Additionally, the labeled protein has been crystallized and the structure solved to a resolution of 2.6 Å. In contrast to the previously described work on P450-BM3[22] which aimed to directly oxidize the heme, our goal here was to explore the biological route of the catalytic cycle by phototriggering electron injection to reduce the gsNOS heme (Scheme 3.2). Initial calculations based on semi-classical electron transfer theory predict that reduction with Ru(I) can occur in the timescale range of 60 ns to 1 μs depending on the actual position of photosensitizer bound to gsNOS in solution. A detailed description of protein expression, ruthenium label synthesis, labeling reaction, characterization, and ET calculations can be found in chapter two of this thesis.

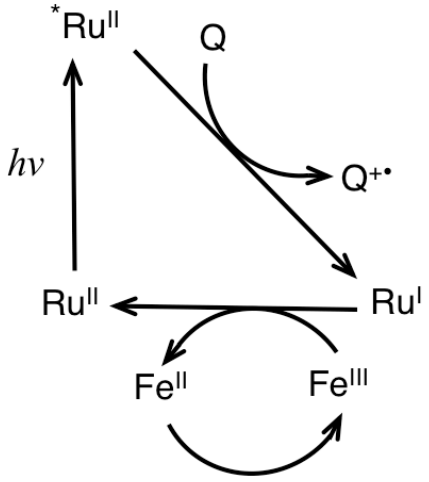

Scheme 3.2 Reductive flash-quench scheme for heme reduction in gsNOS. Ru represents $[Ru(bpy)_2(IA\text{-}phen)]^{2+}$ attached to gsNOS, Q represents the quencher MeODMA, and Fe represents gsNOS heme. *Note*: the reductively quenched excited state may be better described as a Ru(II)(ligand•+), but we will simply use "Ru(I)" here.

3.2 Results and Discussion

Reductively Quenching the Model Complex [Ru(bpy)$_2$(A-phen)]$^{2+}$

In order to investigate the reductive path of the NOS catalytic cycle, we needed a water-soluble, reversible quencher capable of reducing the *Ru(II) excited state to form Ru(I) (this species may actually be Ru(II)(ligand•+), but will be referred to as "Ru(I) in this text), a species capable of injecting an electron into the heme of gsNOS. The organic small molecule quencher, *p*-methoxy-*N.N*-dimethylanaline (MeODMA), has been previously used in the Gray group for flash-quench experiments.[23] Reaction of this quencher with the excited state of a ruthenium(II) diimine complex results in the formation of a MeODMA radical cation, which has its own transient absorption features. Initial controls were performed to independently monitor this quencher species to ensure that it does not interfere with the TA signals of interest, namely the heme Soret of gsNOS (data not shown, but described elsewhere[24]).

In order to distinguish between signals arising from the more complicated labeled protein system and the ruthenium label itself, photophysical properties of the model complex [Ru(bpy)$_2$(A-phen)]$^{2+}$ (where A-phen = 5-acetamido-1,10-phenanthroline) were measured both in the absence and presence of the MeODMA quencher. As expected, the *Ru(II) excited state is luminescent with an emission maxiumum centered around 630 nm. Following 480 nm laser excitation into the tail of the Ru(II) MLCT band, the *Ru(II) luminescence decay is described by a monoexpoenential with a lifetime on the order of τ ~ 1 μs. Upon introduction of excess MeODMA, the luminescence decay at 630 nm is faster with a pseudo first-order rate constant of k = 1.7 x 10^7 s^{-1}, which corresponds to a

time constant (τ) of 58 ns. These data suggest effective quenching and provide a rate of Ru(I) formation.

TA spectroscopy was used to monitor the absorbance changes corresponding to the *Ru(II) electronic excited state, the quenched formation of Ru(I), and recombination to form the Ru(II) ground state of the $[Ru(bpy)_2(A\text{-}phen)]^{2+}$ model complex. The Ru(II) ground state has absorbance bands in the 400–500 nm region which are sensitive to oxidation state: the *Ru(II) excited state has markedly less absorbance in that region and the Ru(I) species has only slightly weaker absorbance than Ru(II). In the absence of MeODMA, the formation of *Ru(II) monitored at 440 nm results in a nearly instantaneous negative optical density (a "bleach") followed by a return to baseline with a rate matching that of the *Ru(II) luminescence decay (Figure 3.4-a). In the presence of quencher, the same initial bleach is observed. A fast increase of absorbance to a very slightly negative overall ΔOD occurs with a rate matching that of the quenched luminescence decay, suggesting the formation of Ru(I). Recombination with the MeODMA radical cation results in a slower return to baseline (Figure 3.4-a). These single-wavelength TA signals were monitored at various wavelengths between 400 and 440 nm and representative traces are shown in Figure 3.4-b. Measurements at longer wavelengths (from 410 to 440 nm) show an unexpected further increase in ΔOD developing at longer timescales (~100 μs). We do not have a definitive assignment for this species, however it seems likely that some of the transiently formed MeODMA radical cation forms other products (e.g., dimerization).[23] Additionally, solutions of MeODMA left overnight under ambient light undergo uncharacterized side reactions as

indicated by development of pink color. All further experiments were done in minimal or red light, using freshly made solutions.

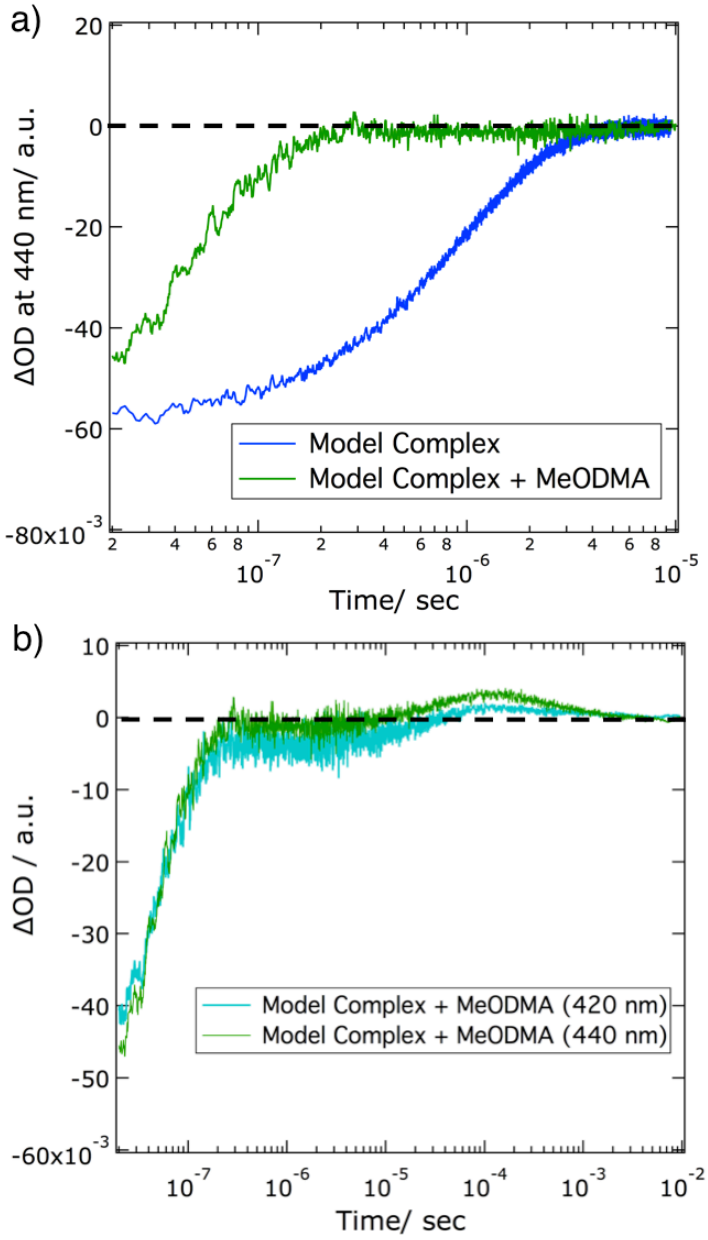

Figure 3.4 Transient absorption traces for the model complex $[Ru(bpy)_2(A\text{-}phen)]^{2+}$: a) comparison of TA at 440 nm for $Ru(bpy)_2(A\text{-}phen)]^{2+}$ (+/- MeODMA quencher); b) TA of quenched model complex at representative wavelengths (420 and 440 nm) showing initial bleach from $^*Ru(II)$, formation of Ru(I), and unassigned positive ΔOD at longer timescales. $[Ru(bpy)_2(A\text{-}phen)]^{2+}]$ = 8 μM and [MeODMA] = 8 mM, 50 mM sodium phosphate buffer, pH 7.

Photoreduction of Ru(II)$_{K115C}$-gsNOS

Luminescence decay traces (630 nm) for the *Ru(II) excited state of our photosensitizer-labeled gsNOS system, Ru(II)$_{K115C}$-gsNOS, are described by a biexponential function (τ_1 = 1.2 μs and τ_2 = 150 ns). τ_1 is very similar to the lifetime of free [Ru(bpy)$_2$(A-phen)]$^{2+}$ model complex. This biexponential behavior has been seen before in other labeled proteins[22] and is attributed to multiple possible solution conformations of the ruthenium complex attached to the protein that do not interconvert on the timescale of the measurements. Upon introduction of MeODMA quencher, this luminescence decay is effectively quenched resulting in a single observed lifetime ($\tau_{quenched}$ = 60 ns), similar to that of the quenched model complex (Figure 3.5). Again, we assign this to the formation of Ru(I). The *Ru(II) excited state is the only emissive species in our system, so transient luminescence data alone do not report on what is happening at the heme center of gsNOS.

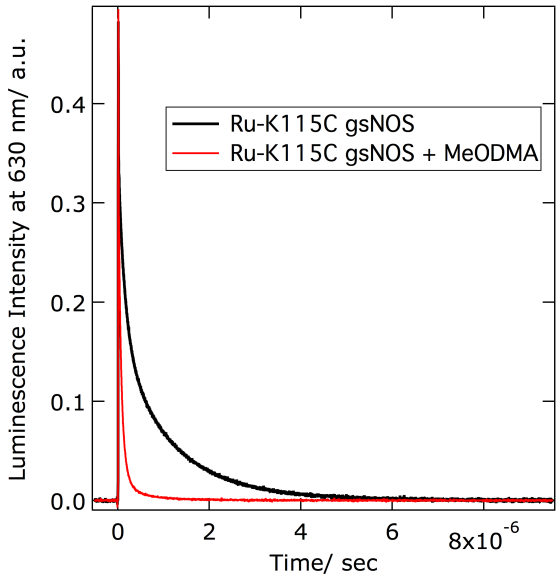

Figure 3.5 Comparison of *Ru(II) luminescence decay of labeled gsNOS with and without quencher, excited at 480 nm and monitored at 630 nm. [Ru(II)$_{K115C}$-gsNOS] = 8 μM and [MeODMA] = 8 mM, 50 mM sodium phosphate buffer, pH 7.

TA measurements were performed to track changes in both the ruthenium photosensitizer and the gsNOS heme oxidation states. The mixed-spin ferric-aquo resting state of gsNOS has a Soret maximum at 403 nm that shifts to 415 nm with shoulder broadening at 450 nm upon reduction to the ferrous state (Figure 3.2).[14] The MLCT bands of the $[Ru(bpy)_2(A\text{-}phen)]^{2+}$ label are also sensitive probes (as described in the previous section). In the absence of quencher, laser excitation at 480 nm results in formation of the $^{*}Ru(II)_{K115C}$-gsNOS-Fe(III) excited state that is characterized by a negative ΔOD in the Ru(II) absorbance with a return to baseline on the same timescale as its luminescence decay (Figure 3.6). We find no evidence for transient species associated with changes in the heme Soret absorbance.

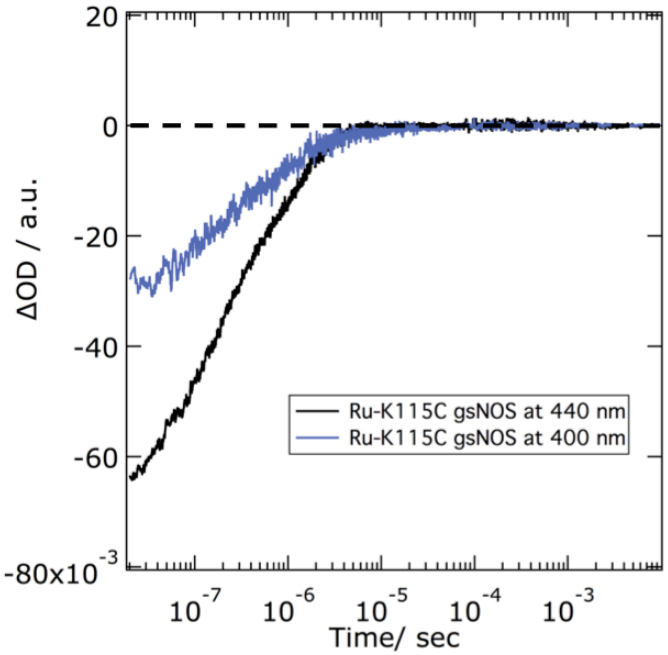

Figure 3.6 Transient absorption traces of the labeled $Ru(II)_{K115C}$-gsNOS system in the absence of quencher showing nearly instantaneous formation of $^{*}Ru(II)$ and the slower decay back to the Ru(II) ground state. Return rates match luminescence data and are independent of wavelength, however the magnitude changes from 400 to 440 nm $[Ru(II)_{K115C}$-gsNOS] = 8 μM, 50 mM sodium phosphate buffer, pH 7.

In contrast, TA measurements of $Ru(II)_{K115C}$-gsNOS made in the presence of quencher are distinct from the signals arising from the unquenched system showing a faster loss of $^{*}Ru(II)$ signal and an overall increase in ΔOD at longer times associated with the formation of ferrous heme (Figure 3.7).

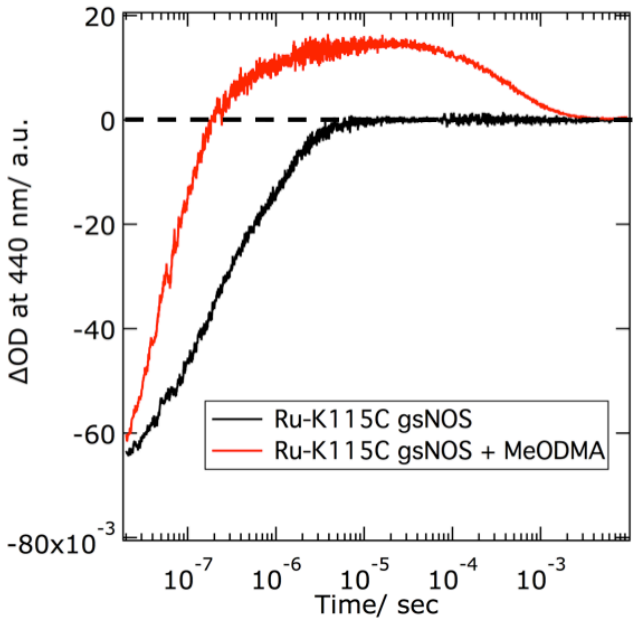

Figure 3.7 Transient absorption data at 440 nm of $Ru(II)_{K115C}$-gsNOS in the presence and absence of quencher. [$Ru(II)_{K115C}$-gsNOS] = 8 μM, [MeODMA] = 8 mM, 50 mM sodium phosphate buffer, pH 7.

Heme reduction in $Ru(II)_{K115C}$-gsNOS is further verified by a persistent bleach at 400 nm and a corresponding absorbance increase at longer wavelengths (410–440 nm) (Figure 3.8), as expected from the red-shifted and broadened Soret band of ferrous gsNOS.

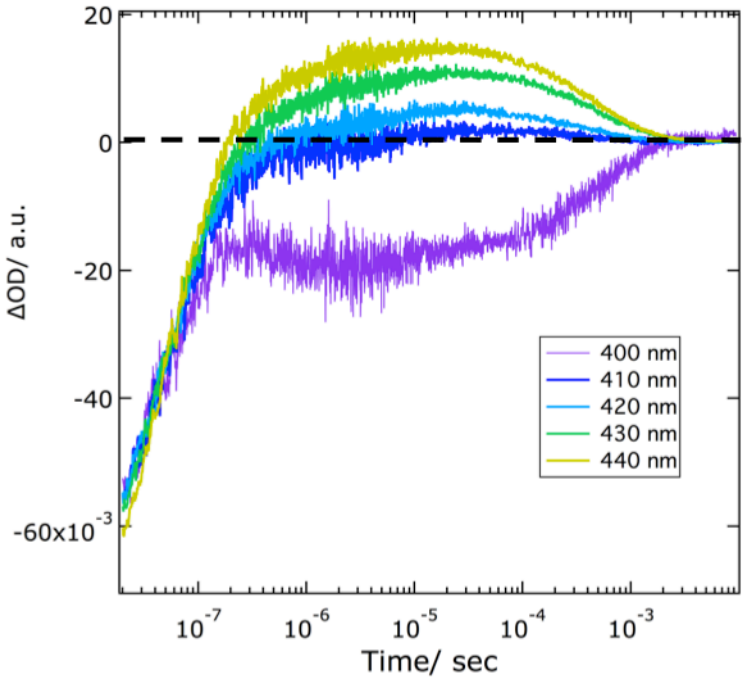

Figure 3.8 Transient absorption data of the quenched $Ru(II)_{K115C}$-gsNOS system at various wavelengths diagnostic of changes in heme Soret. [$Ru(II)_{K115C}$-gsNOS] = 8 μM and [MeODMA] = 8 mM, 50 mM sodium phosphate buffer, pH 7.

The data at early times are described by a biphasic kinetics model for all wavelengths measured, followed by a slow return to baseline at longer timescales. The initial phase is assigned as formation of $Ru(I)_{K115C}$-gsNOS-Fe(III) with a pseudo-first-order rate constant of k_1 = 1.7 x 10^7 s^{-1} (τ_1 = 60 ns) that nicely matches the single exponential rate of quenched model complex (k = 2.1 x 10^7 s^{-1}) and the second phase as heme reduction to form $Ru(II)_{K115C}$-gsNOS-Fe(II) with a rate of k_2 = 1.6 x 10^6 s^{-1} (τ_2 = 625 ns) (Figure 3.9). Global least-squares analysis of TA data from each of 400, 410, 420, 430, and 440 nm yield the same rates. Finally, the heme is reoxidized to form the initial state $Ru(II)_{K115C}$-gsNOS-Fe(III) with a lifetime on the order of $\tau \sim 500$ μs. The reoxidation step is presumably achieved by recombination with MeODMA radical cation,

but we cannot rule out other pathways such as trace impurities or O_2 trapped in the protein matrix.

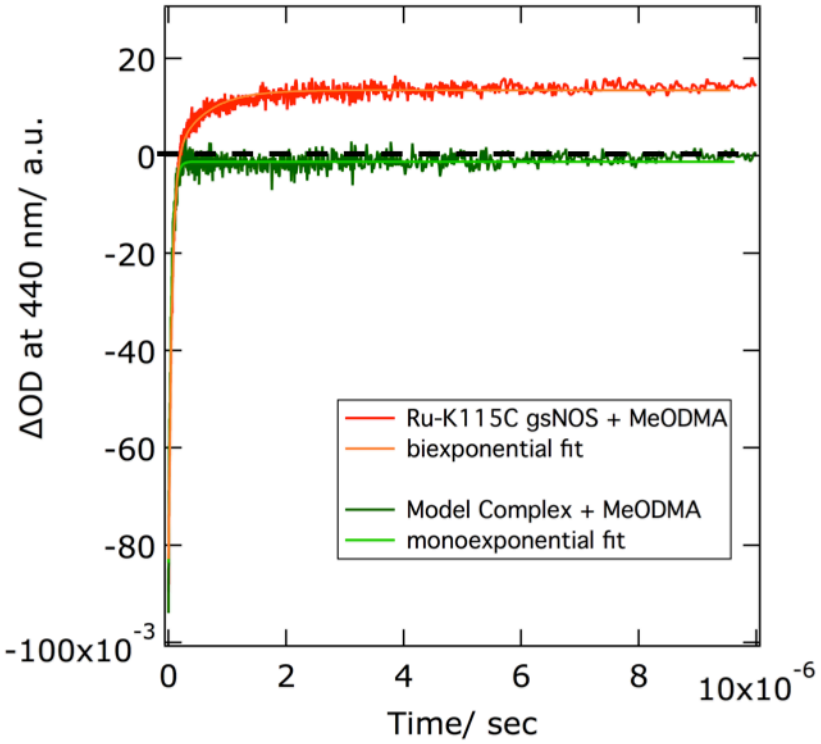

Figure 3.9 Biphasic kinetics of flash-quenched $Ru(II)_{K115C}$-gsNOS at 440 nm in comparison with the model complex $[Ru(bpy)_2(A\text{-}phen)]^{2+}$ at fast timescales. $[Ru(II)_{K115C}\text{-gsNOS}]$ = 8 μM, $[[Ru(bpy)_2(A\text{-}phen)]^{2+}]$ = 8 μM, [MeODMA] = 8 mM, 50 mM sodium phosphate buffer, pH 7.

To summarize the previous data, the observed formation of $Ru(I)_{K115C}$-gsNOS-Fe(III) occurs on the timescale of 60 ns, which is confirmed by both the quenched luminescence lifetime of $Ru(II)_{K115C}$-gsNOS and by the TA data for quenched model complex. The ferrous $Ru(II)_{K115C}$-gsNOS-Fe(II) species forms with a rate of k_{obs} = 1.6 x 10^6 s^{-1}, occurring on the order of 625 ns, which is in the range calculated from semi-classical ET theory (see chapter two for calculations). These data show that we can indeed rapidly inject electrons into the heme from a surface-bound photosensitizer using reductive flash-quench methodology.

Photoreduction of Ru(II)$_{K115C}$-gsNOS in the Presence of Substrate/Cofactor

Substrate and cofactor binding to gsNOS induce a number of changes that may affect the rate of heme reduction. In the NOS catalytic cycle, the binding of substrate (either L-Arg in the first turnover or NOHA in the second) sterically displaces the bound water molecule from the ferric resting state. The resulting five-coordinate high-spin ferric state can then be reduced by one electron from the reductase domain.[5] In the previous section, we showed that our covalently attached ruthenium(II) diimine photosensitizer was capable of reducing the six-coordinate mixed-spin ferric-aquo heme resting state of gsNOS in reductive flash-quench experiments. In addition to the electronic environment of the heme active site being different in the presence of substrate, each of the substrates binds with different affinities. In most cases the enzyme-bound intermediate, NOHA, binds more tightly than L-Arg with dissociation constants of $K_{s,NOHA}$ = 25 μM and $K_{s,L\text{-}Arg}$ = 75 μM for bacterial NOS from *Staphylococcus aureus* (saNOS).[25] This difference in affinity, as well as distinct substrate interaction with heme-bound dioxygen, enables regulation of the chemistry afforded in each of the two catalytic turnovers.[2]

As well as binding the substrates L-Arg and NOHA, NOS binds the unique redox cofactor, H_4B. This cofactor is necessary to supply the second reducing equivalent in the catalytic cycle.[10] There is a specific H_4B binding site known as the "N-terminal hook" in mNOS that is missing in bacterial NOS. Bacterial NOS enzymes, including gsNOS, make up for this with specific residue substitutions on each subunit at the dimer interface.[2] The presence of cofactor also changes the electronic environment, shifting the heme midpoint reduction potential by approximately 50 mV for nNOS and iNOS[26] and having effects on heme interactions with diatomic molecules.[27]

Flash-quench experiments were performed on $Ru(II)_{K115C}$-gsNOS in the presence of L-Arg or NOHA substrate to determine the effects of substrate binding on gsNOS reduction. Luminescence decays in the presence of MeODMA quencher were virtually identical, indicating that initial Ru(I) formation was not affected by either substrate. However, the TA traces of the $Ru(II)_{K115C}$-gsNOS system showed differences in the presence of substrates and slight differences between each L-Arg or NOHA substrate. In the presence of quencher, all samples showed conversion of the $^{*}Ru(II)_{K115C}$-gsNOS-Fe(III) excited state to the $Ru(I)_{K115C}$-gsNOS-Fe(III) species at the same rates, followed by comparable formation of the $Ru(II)_{K115C}$-gsNOS-Fe(II) reduced species. However, the rates of heme reoxidation were noticeably altered in the presence of both L-Arg and NOHA, showing slower returns to baseline with the NOHA-bound species being the slowest (Figure 3.10).

Experiments were also performed with H_4B to evaluate the effect of binding the redox cofactor, and similar results were observed in TA measurements (Figure 3.11). The presence of H_4B slows the reoxidation process as compared to $Ru(II)_{K115C}$-gsNOS alone and to the substrate-bound forms. Additionally, measurements made with both L-Arg and H_4B show even slower returns to baseline.

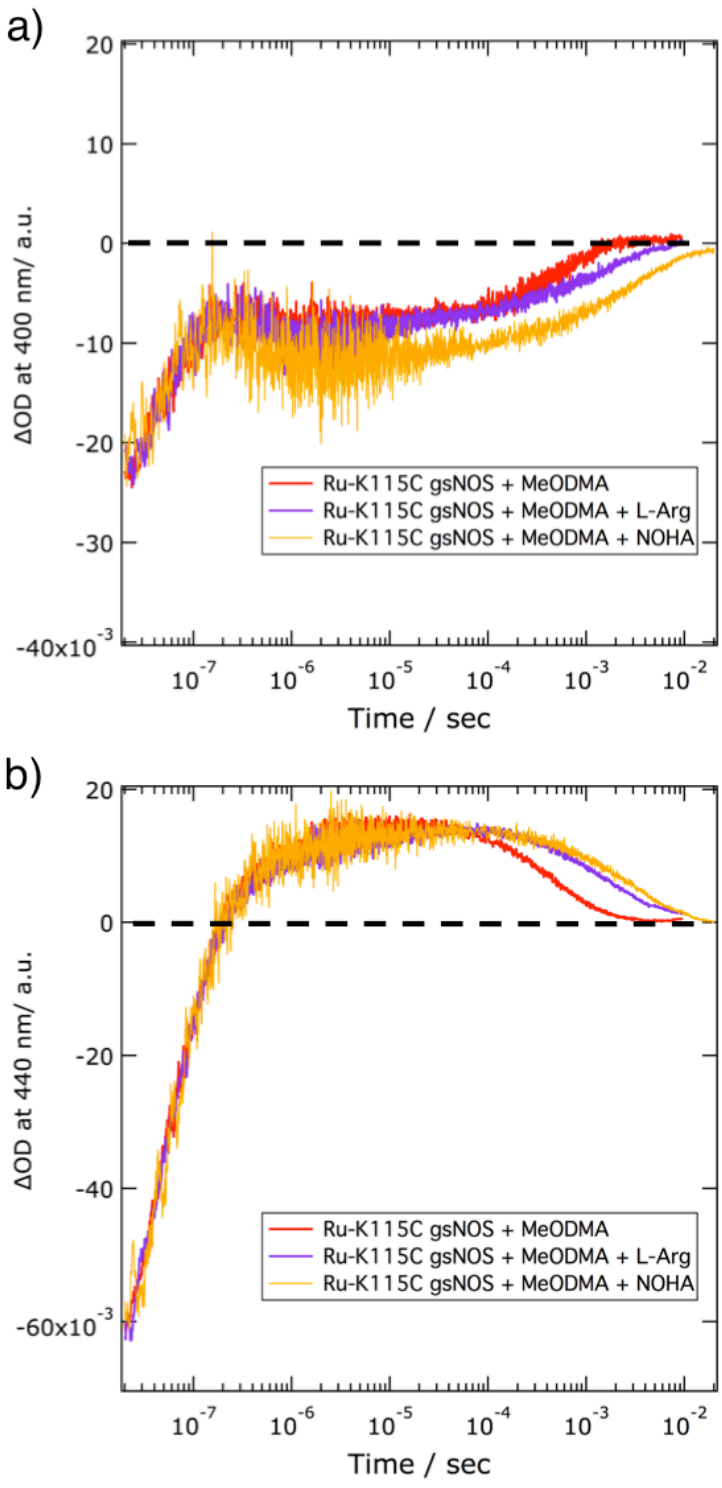

Figure 3.10 Transient absorption traces of the $Ru(II)_{K115C}$-gsNOS system in the presence of substrates from the first and second catalytic turnovers. Comparison of $Ru(II)_{K115C}$-gsNOS with each of L-Arg and NOHA measured at a) 400 nm and b) at 440 nm. [$Ru(II)_{K115C}$-gsNOS] = 8 μM, [L-Arg] = [NOHA] = 200 μM, and [MeODMA] = 8 mM, 50 mM sodium phosphate buffer, pH 7.

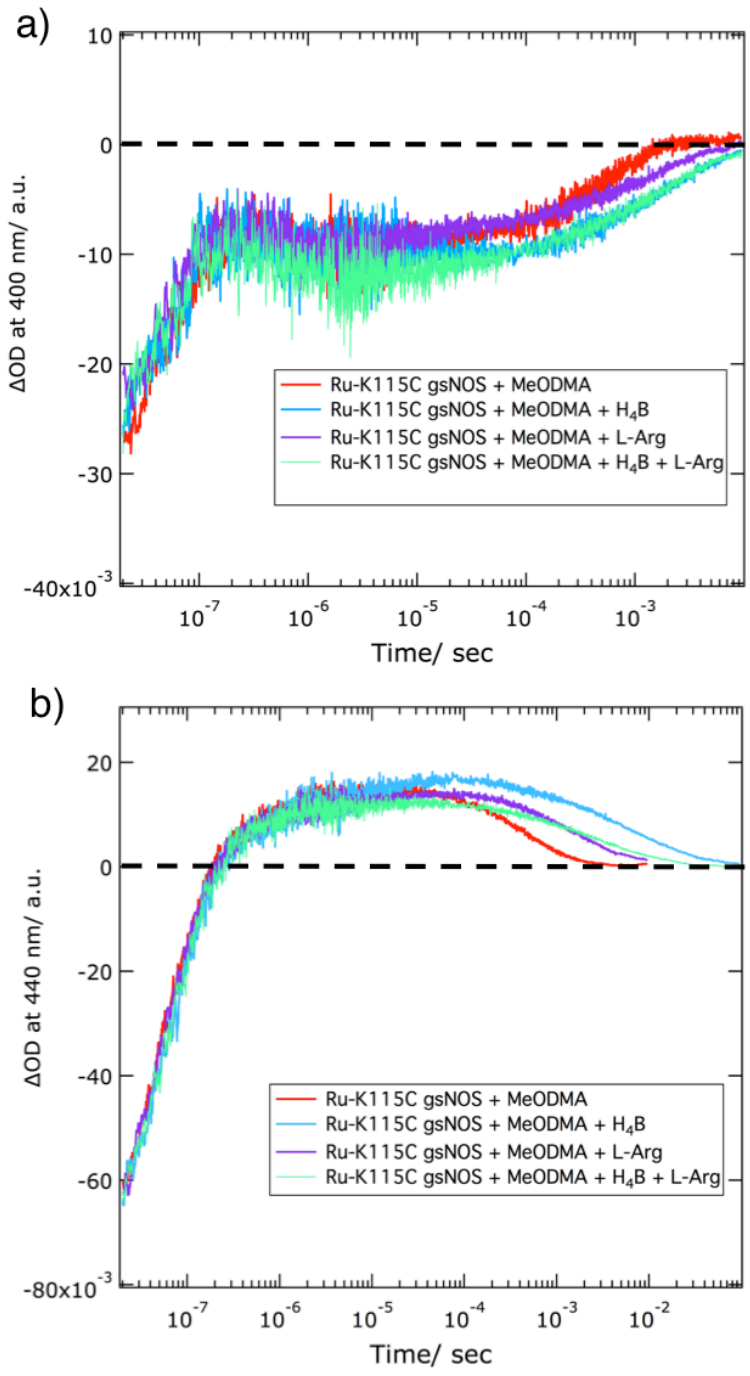

Figure 3.11 Comparative transient absorption traces of the Ru(II)$_{K115C}$-gsNOS system in the presence of the redox-active cofactor H4B +/- L-Arg measured at a) 400 nm and b) 440 nm. [Ru(II)$_{K115C}$-gsNOS] = 8 μM, [H_4B] = 60 μM, [L-Arg] = 200 μM, and [MeODMA] = 8 mM, 50 mM sodium phosphate buffer, pH 7.

The rates of heme reoxidation are changed in the presence of each substrate and cofactor in the following order: L-Arg > NOHA > H_4B > H_4B + L-Arg (with H_4B + L-Arg bound to $Ru(II)_{K115C}$-gsNOS being the slowest), however the rates of initial heme reduction are unchanged. One could test whether heme reduction by Ru(I) is driving force optimized by either altering the reduction potentials of the photosensitizer (by changing the ligands or the metal) or of the heme itself. Usually it is easier to change the label, however substrate/cofactor binding alters the reduction potential of the heme in this case. This is means that we have altered the overall driving force for the $Ru(II)_{K115C}$-gsNOS system in each case of substrate-bound heme. Interestingly, the fact that heme reduction rates do not change suggests that our system is driving force optimized.

If the above analysis is correct, the observed differences in heme reoxidation rates may still result from altered substrate-bound heme potentials, as the back reaction (presumably with the MeODMA radical cation) is not necessarily optimized. Alternatively, the presence of substrate could be blocking the interaction with the MeODMA radical cation. There is an observed contraction of the NOS dimer interface in the presence of substrate/cofactor that could hinder access to the heme by an oxidizing species. There are substantial overall changes in the NOS dimeric structure in the presence of both substrate and cofactor. Crystal structures of NOS from *Bacillus subtilis* (bsNOS) show two distinct dimer conformations in the presence and absence of substrate/cofactor: a "tight" and "loose" form (Figure 3.12).[28] Substrate/cofactor binding induces formation of the "tight" dimer, resulting in structural changes at the interface that bring the two heme active sites closer by approximately 3 Å and translates the subunits by 11 Å. The buried surface area at the dimer interface condenses from 1115 to 480 $Å^2$

per subunit. Furthermore, the helical T-regions lose most of their interactions in the "loose" form, whereas they make close contacts in the "tight" form that are crucial to dimer stability. The consequence of this increased peripheral rigidity and increased dimer association is that the heme is markedly less solvent-exposed in the presence of substrate/cofactor. If such a dimeric contraction is occurring with our $Ru(II)_{K115C}$-gsNOS system, it could account for the ordering of decreased reoxidation rates.

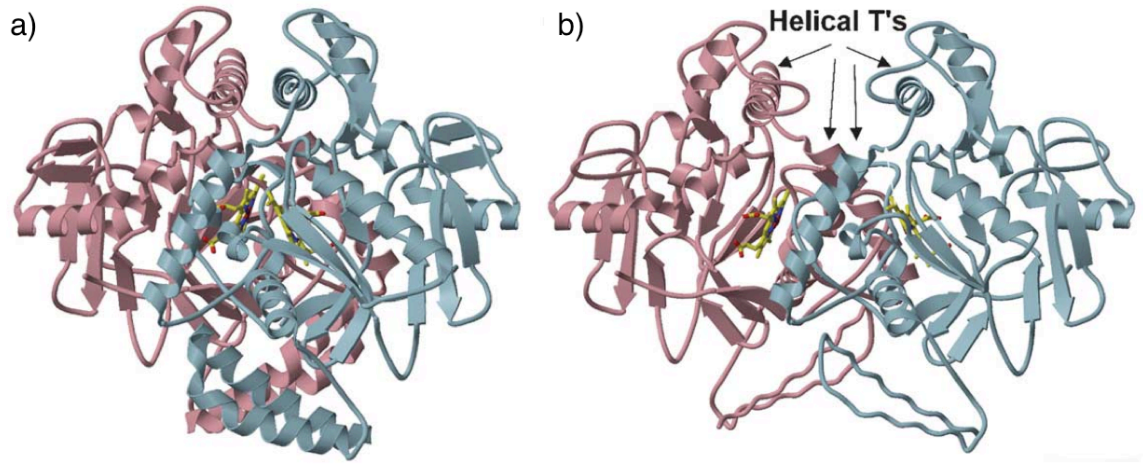

Figure 3.12 Ribbon diagrams of the crystal structures of bsNOS in presence and absence of substrate/cofactor. Subunits are shown in pink and light blue. a) bsNOS with the bound substrate L-Arg forms a "tight" dimer with close contacts formed by the helical T and N-terminal hairpin from each subunit and b) bsNOS in the absence of substrate forms a "loose" dimer and translates one subunit by approximately 11 Å exposing 50% more surface area. Figure reproduced from Pant.[28]

Photoreduction in the Presence of Oxygen

The previous sections described photo-triggered reduction of labeled gsNOS in the presence of substrates and/or cofactor. In order to access the rest of the catalytic cycle (see Figure 3.1), and potentially observe high-valent intermediates, dioxygen must be present. Once the heme is reduced, O_2 binds to give the ferrous-oxy species ($Fe(II)-O_2$). In wild-type gsNOS, this species is remarkably long-lived with a lifetime on the order of

minutes.[14] Single turnover experiments have been reported: in the absence of substrate, a mixture of species that presumably include both Fe(II)-oxy and Fe(III) states are observed, as evident by a broad and flattened Soret around 413 nm. The presence of L-Arg considerably simplifies these experiments with clean formation of gsNOS Fe(II)-O_2 with a Soret maximum at 427 nm (Figure 3.13).

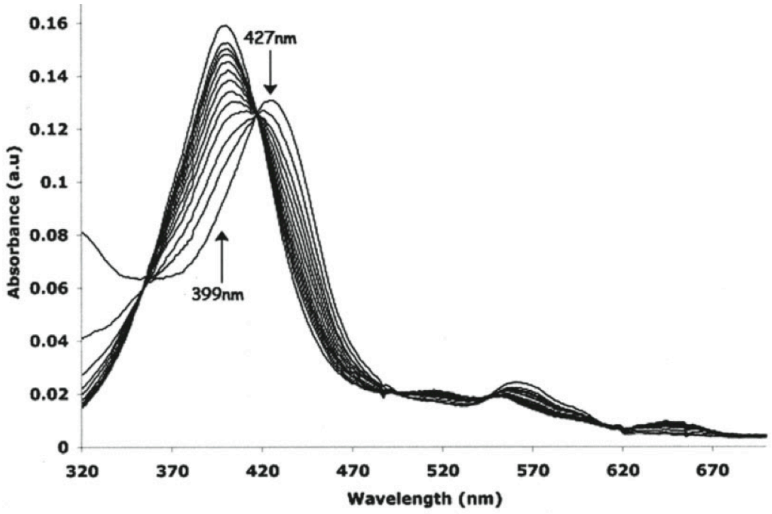

Figure 3.13 UV-visible absorption spectra of the ferrous-oxy complex conversion to the ferric species in the presence of L-Arg from stopped-flow experiments. Chemically reduced w.t. gsNOS loaded with substrate and injected with oxygenated buffer, spectra recorded every 5 sec. Figure reproduced from Sudhamsu.[14]

Flash-quench experiments in the presence of oxygen have been performed for the model complex and the labeled enzyme, in the presence and absence of substrates/cofactor. It should be noted at the outset that these data were very confusing and further complicated by interaction of oxygen with the $Ru(bpy)_2(A\text{-}phen)]^{2+}$ model complex and/or the MeODMA radical cation. These interactions preclude any definitive assignment of oxygenated intermediates. Transient absorption measurements have been recorded for five wavelengths between 400 and 440 nm. Since the cleanest conversion to

Fe(II)-O_2 was previously observed for L-Arg bound enzyme as monitored at 427 nm,[14] this discussion focuses predominantly on data from 430 nm traces.

Photoreduction of Model Complex in Presence of Oxygen

Flash-quench experiments of the $[Ru(bpy)_2(A\text{-}phen)]^{2+}$ model complex in the presence of oxygen have been performed in order to investigate possible oxygen interactions with the $^*Ru(II)$ excited state, the transiently-formed Ru(I) state, or the MeODMA radical cation. Aerated samples containing $[Ru(bpy)_2(A\text{-}phen)]^{2+}$ and MeODMA were excited at 480 nm and the quenched luminescence decay measured at 630 nm. Degassed and aerated samples showed virtually identical luminescence decay kinetics and it was determined that formation of $^*Ru(II)$ and the subsequent formation of Ru(I) were unchanged by O_2.

Transient absorption traces of the same system reveal differences in the presence of O_2. Following the same rates of Ru(I) formation, a species with a positive absorbance grows in on the microsecond timescale. The identity of this species is unknown, however it must come from an interaction between O_2 and either the MeODMA radical cation or the transiently formed Ru(I) model complex. These types of signals were observed at all wavelengths measured. Representative traces are shown in Figure 3.14. Unfortunately, this means that any signals in the labeled-protein system arising on that timescale cannot be unambiguously assigned to protein-based species.

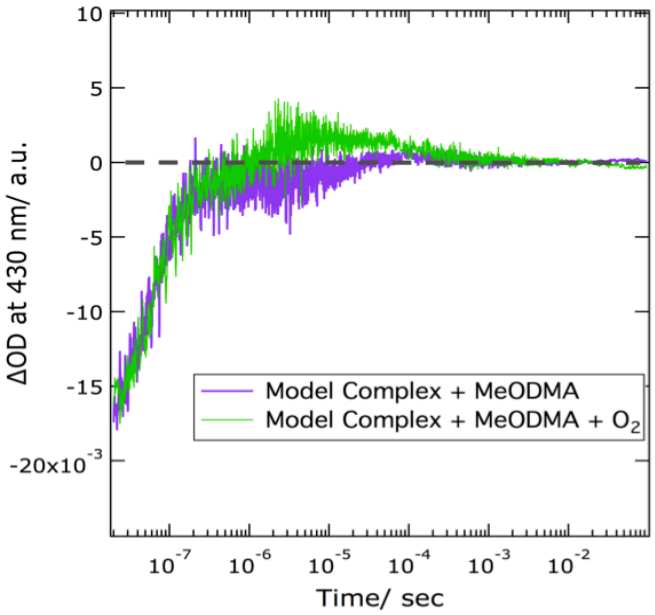

Figure 3.14 Transient absorption traces at 430 nm of the quenched model complex in the presence and absence of oxygen. $[Ru(bpy)_2(A\text{-}phen)]^{2+}$] = 8 μM and [MeODMA] = 8 mM, 50 mM sodium phosphate buffer, pH 7.

Photoreduction of Ru(II)$_{K115C}$-gsNOS in the Presence of Oxygen

Flash-quench experiments of the Ru(II)$_{K115C}$-gsNOS system in the presence of oxygen have been performed in the presence and absence of substrate and cofactor. Under the same conditions previously used for the model complex, aerated samples containing Ru(II)$_{K115C}$-gsNOS and MeODMA were excited at 480 nm and luminescence decay measured at 630 nm. These data for quenched Ru(II)$_{K115C}$-gsNOS were virtually identical, regardless of the presence of substrate, cofactor, or oxygen. As with the model complex, these data indicate that formation of *Ru(II) and subsequent conversion to Ru(I) are unaffected by O_2.

All TA traces of substrate-bound Ru(II)$_{K115C}$-gsNOS show substantial differences in the presence of O_2, however there is no clear formation of an Fe(II)-O_2 species. Qualitatively, it can be seen that Ru(I) forms with the same initial rate, but that the positive ΔOD associated with Fe(II) formation and the reoxidation event are altered

(Figure 3.15-a). Biphasic kinetics are observed in the early timescale data (Figure 3.15-b) and fitting yields the same Ru(I) formation rates: k_1 = 1.7 x 10^7 s^{-1} (τ_1 = 60 ns) for both degassed and aerated samples. The rate constant for the second phase is different with $k_{2,degas}$ = 2.1 x 10^6 s^{-1} ($\tau_{2,degas}$ = 500 ns) and $k_{2,oxygen}$ = 8.9 x 10^5 s^{-1} ($\tau_{2,oxygen}$ = 1.1 μs).

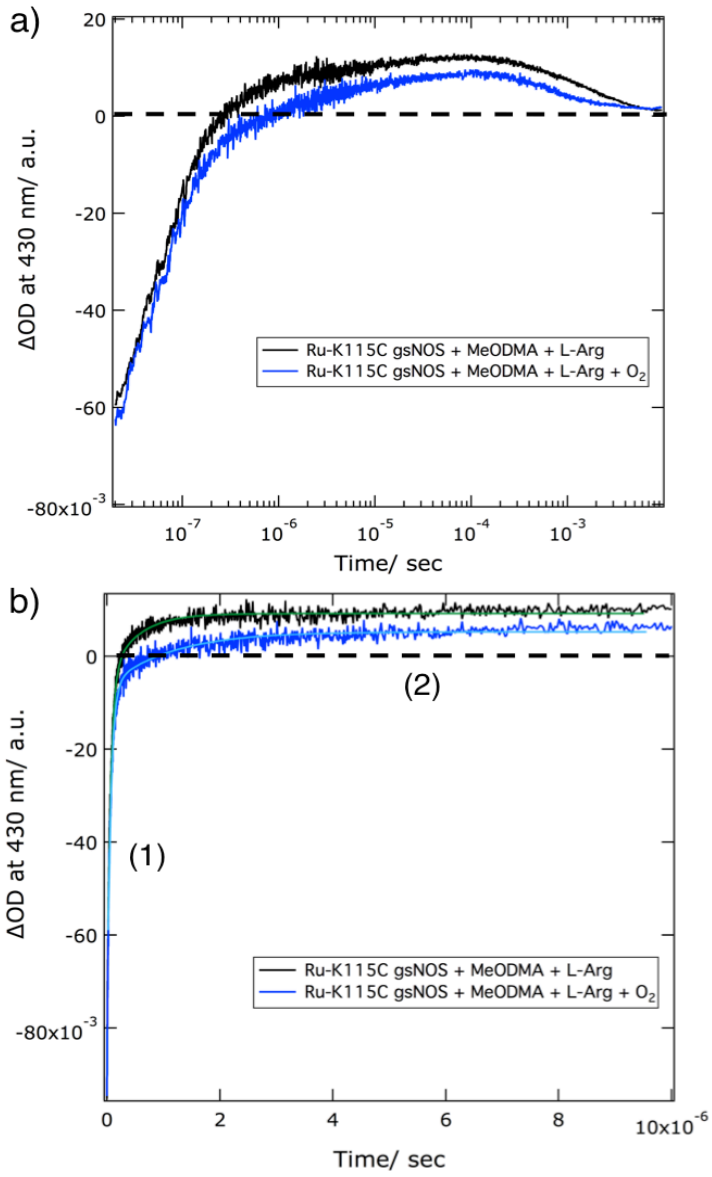

Figure 3.15 Transient absorption traces at 430 nm of the quenched $Ru(II)_{K115C}$-gsNOS system loaded with substrate +/- oxygen a) at longer timescales and b) biphasic kinetics of the first 10 microseconds. [$Ru(II)_{K115C}$-gsNOS] = 8 μM, [L-Arg] = 200 μM, and [MeODMA] = 8 mM, 50 mM sodium phosphate buffer, pH 7.

In the degassed system, $k_{2,degas}$ corresponds to the rate of Fe(II) formation. In the samples containing oxygen, this slower second rate ($k_{2,oxygen}$) for could reflect a number of processes. Altered Fe(II) formation, formation of a new species, or most likely, interaction of Ru(I) or MeODMA with O_2, could give the observed rate. Simple slower Fe(II) formation does not seem reasonable, since whatever amount of transiently formed Ru(I) that is available should still inject electrons to reduce the heme at the same rate.

Comparing the data from the model system with the labeled protein shows similar initial TA signals, followed by a positive ΔOD at longer times that could be associated with a transient protein-based species (Figure 3.16-a, phase 3). Examination of the data at early timescales (0–10 μs) reveals the same distribution of biphasic rates for both samples in the presence of O_2: a fast rate confirmed as the formation of Ru(I) followed by a second rate that is slower in the aerated samples (Figure 3.16-b, phases 1 and 2). Thus, this altered second phase ($k_{2,oxygen}$, also seen in the aerated protein system) must be attributed to the model complex and/or quencher and not to early formation of some other heme-protein species.

Formation of a new species, specifically Fe(II)-O_2, is an appealing cause for the altered signal in "phase 3" (Figure 3.16-a), however from the ground state UV-vis spectra[14] we would expect to see a further *increase* in ΔOD at 430 nm as compared to the degassed sample. It is possible that something else is affecting the yield of the ferrous-oxy species and could only be determined by a *very* careful examination of absorbance profiles across the full wavelength range.

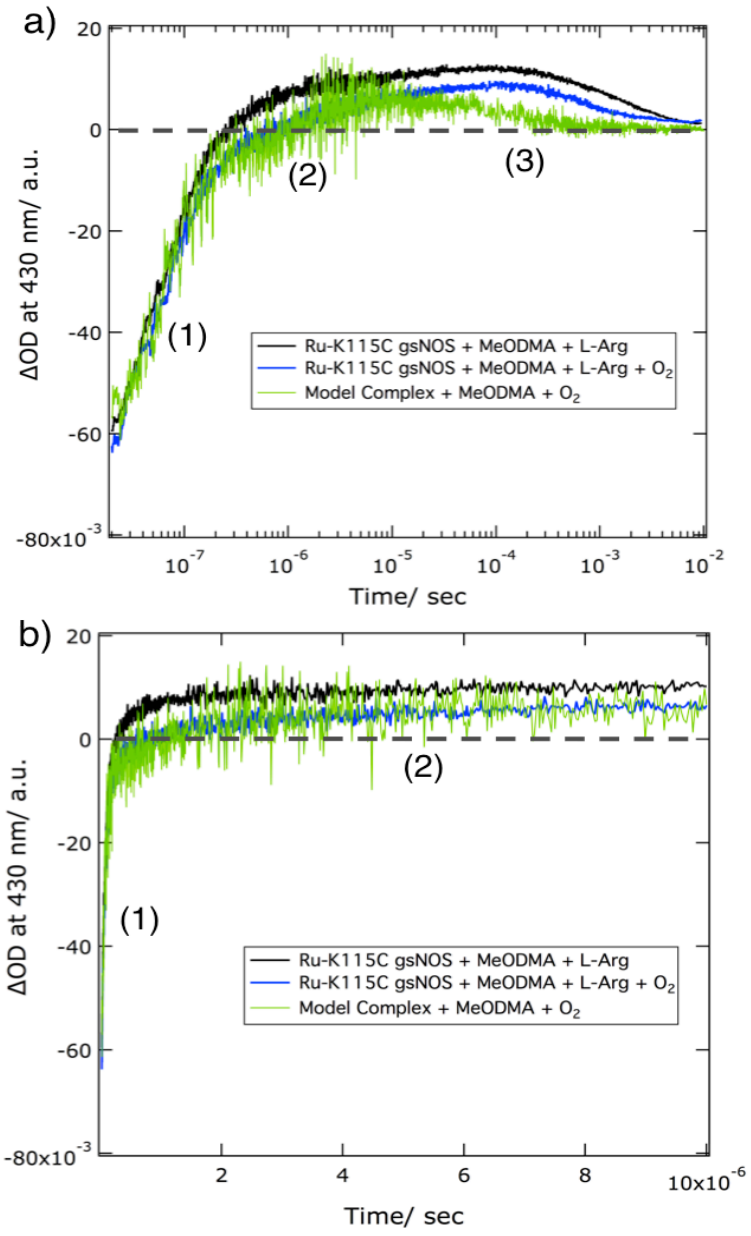

Figure 3.16 Transient absorption traces at 430 nm comparing the substrate-loaded [$Ru(II)_{K115C}$-gsNOS] system with the model complex in the presence of oxygen a) data at long timescale showing growth of protein signal from 100 μs to 1 ms, and b) the same data from 0 to 10 μs showing kinetics attributed to the interaction of model and/or quencher with oxygen. [$Ru(II)_{K115C}$-gsNOS] = [$Ru(bpy)_2(A\text{-}phen)]^{2+}$] = 8 μM, [L-Arg] = 200 μM, and [MeODMA] = 8 mM, 50 mM sodium phosphate buffer, pH 7. Phases are labeled 1–3.

Overall, the data from oxygenated samples of labeled gsNOS are complicated by the fact that the ruthenium(II) diimine label and/or the quencher radical cation are interacting with O_2. While the transient signals arising in "phase 3" are possibly protein derived, we cannot definitively assign them as formation of the desired ferrous-oxy species. We assume that the rate of O_2 binding is very fast (pseudo-first-order at these protein concentrations) once the ferrous state is formed. Unfortunately, we cannot separate the rates from the uncontrolled interactions with label/quencher and thus cannot yet extract this diatomic ligand-binding rate. Despite these confusing results, additional experiments were performed on the [$Ru(II)_{K115C}$-gsNOS] system fully loaded with each substrate (L-Arg and NOHA) and the redox-active cofactor H_4B in the presence of O_2. These were done under the hypothesis that if enough Ru(I) was formed, regardless of possible interactions with oxygen, one NOS cycle could be run and perhaps downstream intermediates observed. Those data (not shown) were equally complicated, with no clear formation of new transient species. Given the complexities of this system, full wavelength TA is needed to monitor changes in both shape and intensity of the Soret bands.

3.3 Conclusion

The covalent attachment of a ruthenium(II) diimine photosensitizer to the surface of gsNOS has provided a system whereby we can rapidly phototrigger heme reduction in the absence of a reductase domain. Reductive flash-quench methodology using the organic quencher, MeODMA, results in transient absorption signals assigned to $Ru(I)_{K115C}$-gsNOS-Fe(III), followed by formation of the $Ru(II)_{K115C}$-gsNOS-Fe(II)

species. This ferrous species forms with a rate of k_{obs} = 1.6 x 10^6 s^{-1} and a time constant (τ) of 625 ns that falls nicely within the range of reduction rates calculated from semi-classical electron transfer theory in chapter two. gsNOS heme reduction has also been achieved in the presence of substrates (L-Arg and NOHA) and the redox cofactor (H_4B); the rates of Fe(II) formation are comparable, despite substrate/cofactor-induced changes in ΔG^o, suggesting this system may be driving force optimized for heme reduction by Ru(I). Interestingly, the reoxidation rates are slower, perhaps reflecting the dimeric structural changes associated with substrate/cofactor binding. Further studies were carried out in the presence of oxygen with the hopes of running the full cycle and observing high-valent oxygenating intermediates. Unfortunately, the kinetics were extremely complicated by interactions of the redox-active O_2 ligand with the ruthenium(II) diimine label itself and/or the MeODMA quencher radical cation. Additional studies are needed to explore the diatomic ligand-binding event to the ferrous enzyme and will be discussed in chapter five of this thesis. Since no definitive assignments of transient intermediates beyond the ferrous state were possible in these experiments, it was determined that the activity of our labeled enzyme should be tested by an independent technique. These experiments and data will be described in chapter four.

3.4 Acknowledgements

I would like give heartfelt thanks to the following people for their contributions to this project: Maraia Ener for her assistance with transient data collection, kinetics fitting, and many, many helpful discussions; Dr. Jeff Warren for very helpful discussions about

"what it all means"; Dr. Charlotte Whited for the original synthesis of MeODMA; and a very talented undergraduate, Katja Luxem, for synthesis of the RuPhen model complex.

3.5 Materials and Methods

Materials

Labeled protein $Ru(II)_{K115C}$-gsNOS was prepared as described in chapter two of this thesis. L-arginine (L-Arg, Sigma) was used as received and stored at room temperature. N^{ω}-hydroxy-L-arginine acetate salt (NOHA, Sigma) was stored at 4 °C and freshly dissolved before each use to prevent hydrolysis. (6R)-5,6,7,8-tetrahydrobiopterin (H_4B, Sigma) was stored at -20 °C. The model complex $[Ru(bpy)_2(A\text{-}phen)]^{2+}$ was synthesized for a different project and was generously shared for use in these experiments. The synthesis followed procedures described in chapter two for the full label, however iodoacetic anhydride was replaced with acetic anhydride. *p*-methoxy-*N.N*-dimethylanaline (MeODMA) was previously synthesized by a former student according to published procedures.[29] To remove any age-related impurities, the stock of MeODMA was purified by sublimation under static vacuum (at ~75 °C) and portions of the white crystalline solid were stored in a dessicator under argon gas in between uses. Fresh stock solutions of the quencher MeODMA were made before each set of experiments and kept dark. Due to its limited solubility in water, 8 mg of MeODMA were first dissolved in 500μL of dimethyl sulfoxide (DMSO) and brought up to a total volume of 2.5 mL by dropwise addition of 50 mM sodium phosphate buffer resulting in a 25 mM stock solution (attempts to increase the stock concentration resulted in supersaturated solutions and precipitation).

General Sample Preparation

All samples were prepared in 50 mM sodium phosphate (NaPi) buffer, pH 7 using Milli-Q (18.2 MΩ) water and filtered (0.22 μm, Millipore) before use. *Note:* all ruthenium(II) diimine-containing samples were kept covered in foil or handled under red light to prevent photodamage. Specialized 1 cm pathlength quartz cuvettes (Starna Cells) fitted with Kontes valves and side-arm ground-glass Schlenk adaptors were made in-house at the Caltech glassblowing shop (Rick Gerhart). Cuvettes containing micro stir bars were attached to a Schlenk line and degassed by three sets of ten pump-purge cycles (very quick vacuum, followed by argon back-filling) spaced in 15 min intervals. This method provides a gentle way to degas protein samples that avoids denaturation caused by bubbling. Argon gas was precleaned by a commercially available oxygen scrubber before entering the line (Oxiclear, Labclear).

Typical sample volumes were 2 mL to provide enough height in the cuvette to accommodate both a micro stir bar and the width of laser/probe light without spatial interference. Labeled protein and model complex concentrations were chosen to balance decent signal size with ground state absorbance in the range of 0.8 OD at the Soret maximum and 0.4 at the Ru shoulder. Quencher concentrations were kept at 1000-fold excess to allow fitting of pseudo first-order kinetics. Substrate and cofactor concentrations were chosen to ensure all proteins were bound and mimicked conditions used in published single-turnover studies. Sample component concentrations were as follows: [$Ru(II)_{K115C}$-gsNOS] = 8 μM, [[$Ru(bpy)_2$(A-phen)]$^{2+}$] = 8 μM, [MeODMA] = 8 mM, [L-Arg] = 200 μM, [NOHA] = 200 μM, [H_4B] = 60 μM. UV-visible absorption

spectra were collected for all samples before and after laser experiments to confirm concentrations and to monitor sample stability.

Spectroscopic Measurements

All steady state and time-resolved spectroscopic measurements were carried out at the Beckman Institute Laser Resource Center. UV-visible absorption spectra were recorded on an Agilent 8453 UV-vis Spectrophotometer. Laser excitation for time-resolved measurements was provided by 8 ns pulses from a 10 Hz Q-switched Nd:YAG laser (Spectra-Physics Quanta-Ray PRO-Series). The third harmonic (355 nm) was used to pump an optical parametric oscillator (OPO, Spectra-Physics Quanta-Ray MOPO-700, tunable in the visible region). Laser light from the OPO at 480 nm with a final power of approximately 10 mJ/pulse (at the sample) was used to excite samples. Schematic for transient luminescence measurements is shown in Figure 3.17.

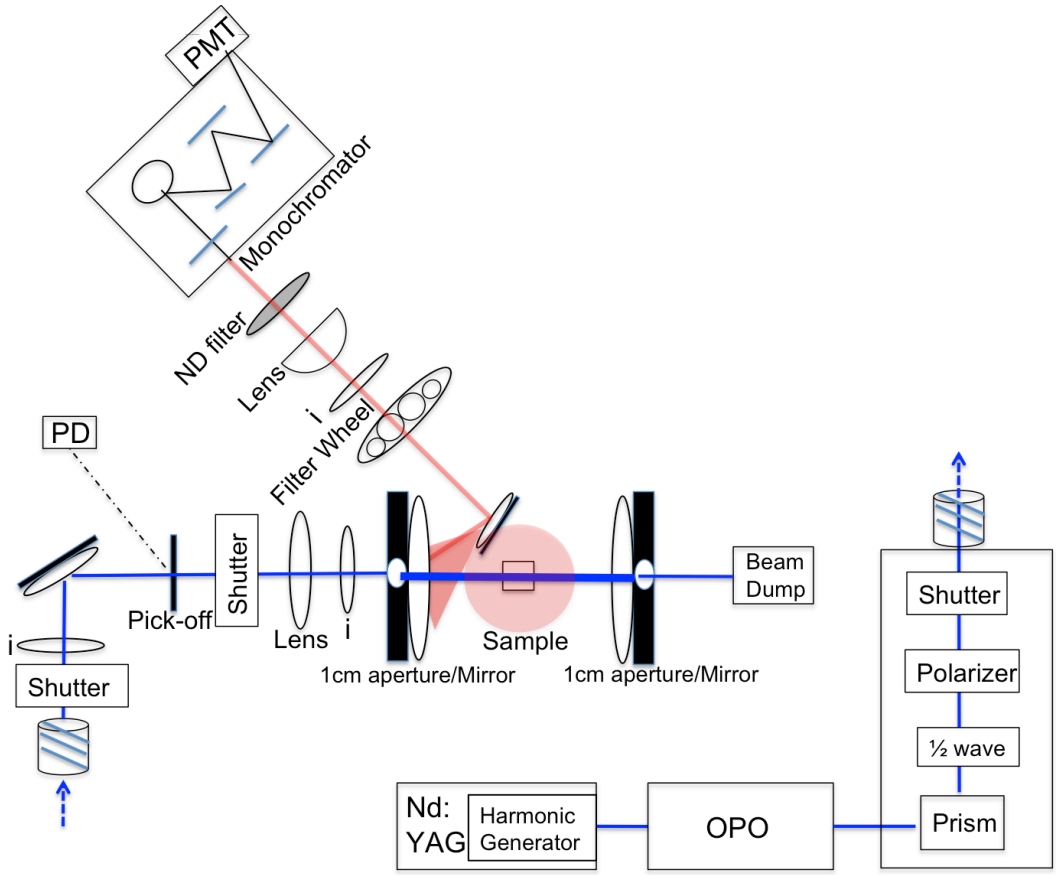

Figure 3.17 Laser and optical configuration used in transient luminescence studies. Following laser excitation, the light emitted from the sample is focused into the monocromator to select a specific wavelength and then collected at the PMT allowing for time-resolved measurements at a single wavelength. PD = photodiode used for timing shutter control, ND = neutral density filter, and i = iris used for alignment. All other components are described in the text. Note that the configuration is the same for transient absorption measurements minus the probe light source (see Figure 3.18).

Probe light for transient absorption kinetics measurements was provided by a 75 W arc lamp (PTI Model A 1010) that can be operated in continuous wave or pulsed modes. Timing between the laser and the probe light was controlled by a digital delay generator (EG&G 9650). After passing through the sample collinearly with the laser beam, probe wavelengths were selected for detection by a double monochromator (Instruments SA DH- 10) with 1 mm slits. Transmitted light was detected with a

photomultiplier tube (PMT, Hamamatsu R928) (Figure 3.18). The PMT current was amplified and recorded with a transient digitizer (LeCroy 9354A or Tektronix DSA 602). The data were converted to units of ΔOD ($\Delta OD = -\log_{10}(I/I_0)$, where I is the time-resolved probe-light intensity with laser excitation, and I_0 is the intensity without excitation).

Samples measured on the microsecond timescale or faster were stirred continuously and excited using a laser repetition rate of 10 Hz, with 100 shots/cycle x 3 cycles. Samples measured on a millisecond timescale were excited with a shutter-released laser pulse, stirred for 1 sec after collecting data, then allowed to sit for 2 sec until the solution settled before the next laser pulse. The sample was shot 1/cycle x 20 cycles in this configuration. All instruments and electronics in these systems were controlled by software written in LabVIEW (National Instruments).

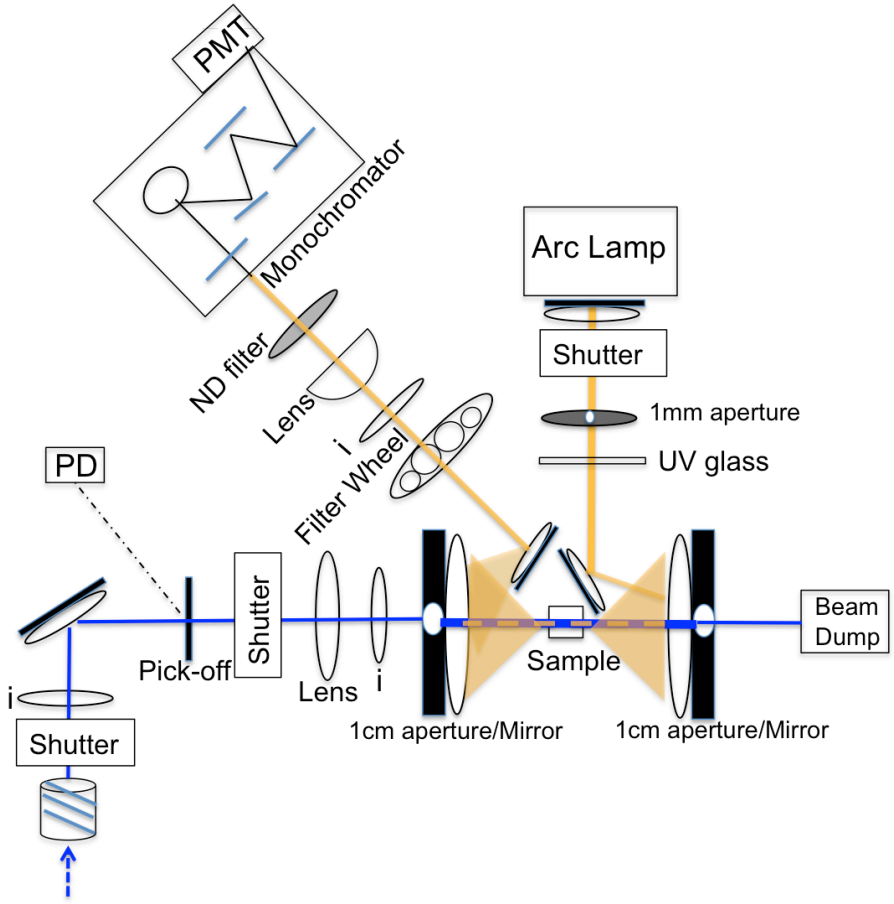

Figure 3.18 Optical configuration for transient absorption measurements. The arc lamp provides probe light through the sample along the same path as laser excitation. Initial probe light is collected through the ground state sample providing a blank measurement. Laser pulses are then timed to excite the sample and the resulting light transmitted through the excited state of the sample is recorded at the PMT. Laser source and component abbreviations are as in Figure 3.17 for the transient luminescence setup.

Data Fitting

Initial transient absorption data manipulation was performed using MATLAB R2010a (Mathworks, Inc.) as follows: for each wavelength, data from three different timescales (2 μs, 100 μs, and 100 ms) were logarithmically compressed with 600 points per decade. The compressed data were adjusted to match intensities by inspection, spliced together, and the x-axis was shifted to set the signal rise to $t = 0$. Data were fit to multiple exponentials using nonlinear least-squares minimization and quality of fit was evaluated

by inspection of residuals. Global least-squares analysis was used to fit data from multiple wavelengths to a single set of rates and amplitudes. Plots were made using IgorPro 6.1 (Wavemetrics).

3.6 References

1. Hughes, M. N. Chemistry of Nitric Oxide and Related Species. *Methods in Enzymology* **436**, 3–19 (2008).
2. Crane, B. R., Sudhamsu, J. & Patel, B. A. Bacterial Nitric Oxide Synthases. *Annu Rev Biochem* **79**, 445–470 (2010).
3. Marletta, M. A. Nitric Oxide Synthase Structure and Mechanism. *J Biol Chem* **268**, 12231-12234 (1993).
4. Stuehr, D. J. Update on Mechanism and Catalytic Regulation in the NO Synthases. *J Biol Chem* **279**, 36167–36170 (2004).
5. Alderton, W. K., Cooper, C. E., Knowles, R. G. Nitric Oxide Synthase: Structure, Function, and Inhibition. *Biochem J* **357**, 593-615 (2001).
6. Stuehr, D. Oxygen Reduction by Nitric-oxide Synthases. *J Biol Chem* **276**, 14533–14536 (2001).
7. Agapie, T. *et al.* NO formation by a catalytically self-sufficient bacterial nitric oxide synthase from Sorangium cellulosum. *Proc Nat Acad Sci USA* **106**, 16221–16226 (2009).
8. Sono, M., Roach, M. P., Coulter, E. D., Dawson, J. H., Heme-Containing Oxygenases. *Chem Rev* **96**, 2841-2887 (1996).
9. Zhu, Y. & Silverman, R. B. Revisiting Heme Mechanisms. A Perspective on the Mechanisms of Nitric Oxide Synthase (NOS), Heme Oxygenase (HO), and Cytochrome P450s (CYP450s). *Biochemistry* **47**, 2231–2243 (2008).
10. Wei, C.-C., Crane, B. R. & Stuehr, D. J. Tetrahydrobiopterin Radical Enzymology. *Chem Rev* **103**, 2365–2384 (2003).
11. Davydov, R. *et al.* EPR and ENDOR Characterization of Intermediates in the Cryoreduced Oxy-Nitric Oxide Synthase Heme Domain with Bound l-Arginine or N G Hydroxyarginine. *Biochemistry* **41**, 10375–10381 (2002).
12. Woodward, J. J., Chang, M. M., Martin, N. I. & Marletta, M. A. The Second Step of the Nitric Oxide Synthase Reaction: Evidence for Ferric-Peroxo as the Active Oxidant. *J Am Chem Soc* **131**, 297–305 (2009).
13. Winkler, J. R. & Gray, H. B. Electron transfer in ruthenium-modified proteins. *Chem Rev* **92**, 369–379 (1992).
14. Sudhamsu, J. Structure and Reactivity of a Thermostable Prokaryotic Nitric-oxide Synthase That Forms a Long-lived Oxy-Heme Complex. *J Biol Chem* **281**, 9623–9632 (2005).
15. Chang, I. J., Gray, H. B. & Winkler, J. R. High-driving-force electron transfer in metalloproteins: intramolecular oxidation of ferrocytochrome c by Ru (2, 2'-bpy) 2 (im)(his-33) 3+. *J Am Chem Soc* **113**, 7056–7057 (1991).
16. Huynh, M. H. V., Dattelbaum, D. M. & Meyer, T. J. Exited state electron and energy transfer in molecular assemblies. *Coord Chem Rev* **249**, 457–483 (2005).
17. Berglund, J., Pascher, T., Winkler, J. R., Gray, H. B. Photoinduced Oxidation of Horseradish Peroxidase. *J Am Chem Soc* **119**, 2464-2469 (1997).
18. Low, D., Winkler, J. R., Gray, H. B. Photoinduced Oxidation of Microperoxidase-8: Generation of Ferryl and Cation-Radical Porphyrins. *J Am Chem Soc* **118**, 117-120 (1996).

19. Dmochowski, I. J., Crane, B. R., Wilker, J. J., Winkler, J. R., Gray, H. B. Optical Detection of Cytochrome P450 by Sensitizer-linked Substrates. *Proc Nat Acad Sci USA* **96**, 12987-12990 (1999).
20. Dunn, A. R., Dmochowski, I. J., Winkler, J. R. & Gray, H. B. Nanosecond Photoreduction of Cytochrome P450cam by Channel-Specific Ru-diimine Electron Tunneling Wires. *J Am Chem Soc* **125**, 12450–12456 (2003).
21. Belliston-Bittner, W. *et al.* Picosecond Photoreduction of Inducible Nitric Oxide Synthase by Rhenium(I)−Diimine Wires. *J Am Chem Soc* **127**, 15907–15915 (2005).
22. Ener, M. E., Lee, Y. T., Winkler, J. R., Gray, H. B. & Cheruzel, L. Photooxidation of cytochrome P450-BM3. *Proc Nat Acad Sci USA* **107**, 18783–18786 (2010).
23. Mines, G. A., et al. Rates of Heme Oxidation and Reduction in Ru(His33)cytochrome c at Very High Driving Forces. *J Am Chem Soc* **118**, 1961-1965 (1996).
24. Mines, G. A. Cytochrome c: Folding Triggered by Electron Transfer. Rates of Heme Oxidation and Reduction at High Driving Forces; PhD Thesis; California Institute of Technology, Pasadena, 1997.
25. Salard, I. *et al.* Analogies and surprising differences between recombinant nitric oxide synthase-like proteins from Staphylococcus aureus and Bacillus anthracis in their interactions with l-arginine analogs and iron ligands. *J Inorg Biochem* **100**, 2024–2033 (2006).
26. Presta, A., Weber-Main, A. M., Stankovich, M. T. & Stuehr, D. J. Comparative effects of substrates and pterin cofactor on the heme midpoint potential in inducible and neuronal nitric oxide synthases. *J Am Chem Soc* **120**, 9460–9465 (1998).
27. Kabir, M., Sudhamsu, J., Crane, B. R., Yeh, S.-R. & Rousseau, D. L. Substrate−Ligand Interactions in Geobacillus stearothermophilus Nitric Oxide Synthase. *Biochemistry* **47**, 12389–12397 (2008).
28. Pant, K. & Crane, B. R. Structure of a Loose Dimer: an Intermediate in Nitric Oxide Synthase Assembly. *Journal of Molecular Biology* **352**, 932–940 (2005).
29. Sekiya, M., Tomie, M. & Leonard, N. J. Dealkylation of aromatic tertiary amines with formates. *J Org Chem* **33**, 318–322 (1968).

Chapter Four

LIGHT-DRIVEN CATALYSIS IN RUTHENIUM-MODIFIED NITRIC OXIDE SYNTHASE FROM *GEOBACILLUS STEAROTHERMOPHILUS*

4.1 Introduction

Nitric oxide synthase (NOS) is a monooxygenase responsible for the biological production of the radical nitric oxide (NO).[1] NOS converts the amino acid L-arginine (L-Arg) to L-citrulline (L-Cit) and NO via a stable enzyme-bound intermediate, N^{ω}-hydroxy-L-arginine (NOHA).[2] This reaction proceeds in two turnovers of the catalytic cycle. There are three NOS isoforms found in mammals (mNOS)[3] and NOS-like enzymes have now been discovered in all kingdoms of life, including archaea and bacteria.[4] All NOS isoforms function as homodimers and share nearly identical active sites containing a cysteine-ligated heme, as well as substrate and redox cofactor binding sites. However there are some differences between mNOS and bacterial NOS. The most striking difference is that while mNOSs have a linked reductase domain,[5] all but one of the bacterial NOS enzymes lack a dedicated reductase domain.[6] Chapter one of this thesis provides details about the domains of mNOS and structural differences in bacterial NOS.

The full mechanism by which NOS catalytically produces NO from L-Arg is still unknown,[3] however steps can be borrowed from other members of the cysteine thiolate-ligated heme enzyme superfamily to which it belongs. The first NOS turnover is a two-electron oxidation of L-Arg resulting in the hydroxylation of a guanidinium nitrogen in a reaction that is nearly identical to that of cytochrome P450-catalyzed hydroxylation; the second turnover, a three-electron oxidation to form NO and L-Cit, is thought to follow a unique mechanism.[7] The NOS resting state is a six-coordinate mixed-spin aquo-ferric heme. Substrate binding (L-Arg in the first cycle and NOHA in the second) in the pocket sterically displaces water to form a five-coordinate high-spin ferric state. Ferric NOS is reduced by one electron originating from the reductase domain to give a ferrous species

that can bind O_2. This ferrous-oxy species (often represented as a ferric-superoxide) is further reduced by one electron supplied by the redox-active cofactor (6R)-5,6,7,8-tetrahydrobiopterin (H_4B, pterin).[8] To date, the next experimentally observed species is the ferric resting state with bound NOHA. The second turnover shares similar steps: reduction, O_2 binding, and reduction by H_4B. From there, the next observed species is the NO-bound ferric heme, which then releases NO and L-Cit to complete the cycle. The missing oxygenating intermediates are thought to be a ferryl porphyrin radical cation[9] (analogous to Cpd I in P450) in the first turnover and either a hydroperoxo ferriheme[10] or Cpd I formed by subsequent protonation/water loss in the second[9] (Figure 4.1).

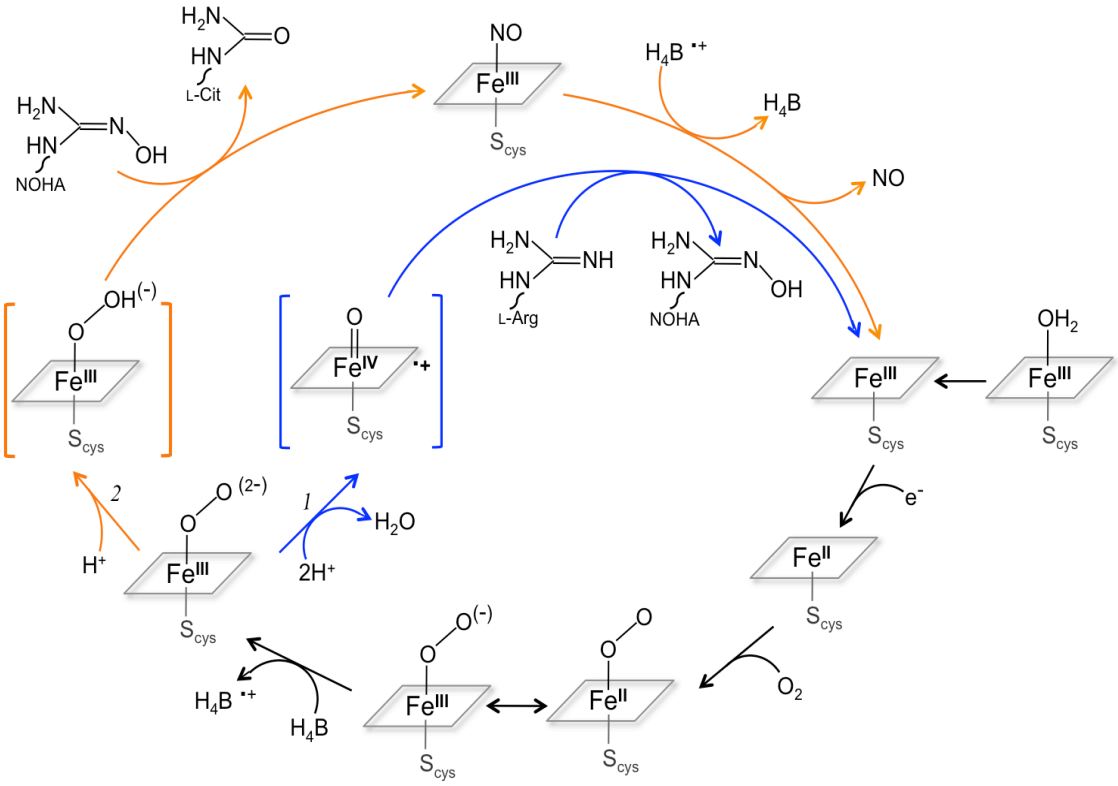

Figure 4.1 Putative mechanism for the catalytic production of NO by NOS enzymes: (1) first turnover formation of NOHA from L-Arg, shown in blue path; (2) second turnover formation of L-Cit and NO radical from NOHA, shown in orange path. The proposed oxygenating intermediates are shown in brackets.

Flash-quench methodology[11] has been developed in the Gray group to gain access to short-lived intermediates and is described more thoroughly in chapters one and three of this thesis. Briefly, laser excitation (the "flash") into the metal-ligand charge-transfer (MLCT) band of a ruthenium(II)diimine photosensitizer (e.g., $[Ru(bpy)_3]^{2+}$, bpy = 2,2'-bipyridine) creates an electronic excited state approximately 1.2 eV above the ground. This excited state can be "quenched" by an appropriate small molecule in solution yielding either a powerful -1.3 V reductant or +1.3 V oxidant[12] that can then go on to inject or pull electrons from the system of interest, such as heme. High-valent intermediates from various heme-containing proteins have been photoinduced using these techniques and these species have been observed by transient absorption (TA) spectroscopy.[13–15]

With the motivation of catching high-valent intermediates in the NOS catalytic cycle, a ruthenium(II) diimine photosensitizer has been covalently attached to the surface of NOS from the thermostable, nonpathogenic bacterium *Geobacillus stearothermophilus* (gsNOS). As gsNOS, like most bacterial NOS enzymes, lacks a dedicated reductase domain, we have the opportunity to supply electrons to the active site via a photosensitizer, thus side-stepping the need for a reductase domain entirely. A single surface cysteine mutation has been installed at position 115 in gsNOS for selective labeling with $[Ru(bpy)_2(IA\text{-}phen)]^{2+}$ (where IA-phen = 5-iodoacetamido-1,10-phenanthroline). The resultant conjugate, $Ru(II)_{K115C}$-gsNOS, has been characterized and crystallized with the structure solved to a resolution of 2.6 Å. Details regarding the expression, labeling, and full characterization can be found in chapter two of this thesis.

Reductive flash-quench experiments with this labeled $Ru(II)_{K115C}$-gsNOS system have been performed and are described in chapter three of this thesis. Anaerobic samples containing $Ru(II)_{K115C}$-gsNOS and an excess of the small-molecule quencher, *p*-methoxy-*N.N*-dimethylanaline (MeODMA) were irradiated with pulsed laser light at 480 nm (the "flash") to form the $^{*}Ru(II)$ excited state as outlined in Scheme 4.1 below.

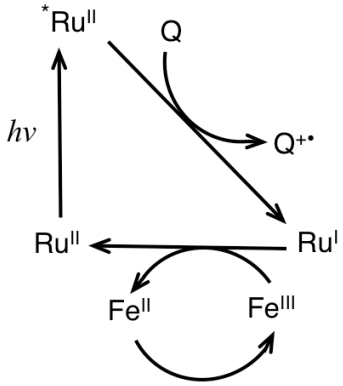

Scheme 4.1 Reductive flash-quench scheme for heme reduction in gsNOS. Ru represents the $[Ru(bpy)_2(IA\text{-}phen)]^{2+}$ complex attached to gsNOS, Q represents the quencher MeODMA, and Fe represents gsNOS heme.

Following laser excitation, the $^{*}Ru(II)_{K115C}$-gsNOS-Fe(III) excited state is quenched by MeODMA to transiently form $Ru(I)_{K115C}$-gsNOS-Fe(III). This Ru(I) species can then rapidly reduce the ferric resting sate of the gsNOS heme to form the ferrous enzyme $Ru(II)_{K115C}$-gsNOS-Fe(II). Presumably, recombination with the MeODMA radical cation[16] reoxidizes the heme to form the initial $Ru(II)_{K115C}$-gsNOS-Fe(III) state. Both the MLCT bands of the ruthenium complex and the Soret bands of the heme are sensitive to changes in oxidation state[17] and these absorption features can thus be used as spectroscopic handles to follow these types of processes. As such, transient absorption (TA) spectroscopy was performed and signals measured at various wavelengths in the range of 400–440 nm. The data from these experiments clearly show successful and rapid

electron injection into the heme from a surface-bound photosensitizer using reductive flash-quench methodology. The measured rate of electron transfer (ET) for this system is $k_{obs} = 1.6 \times 10^6\ s^{-1}$, with ferrous formation on the order of 625 ns.

Since the original goal was to observe the NOS catalytic cycle in action, similar flash-quench experiments were conducted with substrate- and cofactor-loaded enzyme in the presence of oxygen. In these experiments, flash-quench should produce a ferrous heme that readily binds O_2 to form the Fe(II)-oxy species and thus begin the catalytic cycle (Figure 4.1). Unfortunately, the kinetics were drastically complicated by interactions of O_2 with the transiently formed Ru(I) state of the label and/or the MeODMA quencher radical cation. While certain changes in the TA signals were suggestive of formation of a new species, definitive assignment of Fe(II)-oxy was not possible. It was determined that the light-driven activity of our ruthenium-modified enzyme should be tested by independent techniques (all of the laser experimental details and kinetics analyses can be found in chapter three).

Recently, a number of exciting examples of light-driven catalysis have been reported which have inspired the work described in this chapter. Nitrogenase catalyzes the biological reduction of nitrogen (N_2) to form ammonia (NH_3). This ATP-dependent, eight electron/eight proton reaction is achieved by cooperativity between two domains. Hydrolysis of two ATP molecules by the iron-protein (FeP) allows for injection of one electron at a time to the iron-molybdenum protein (MoFeP) that houses the active site. Characterization of reaction intermediates has been complicated by this continuous flow of electrons. A system has been designed that decouples this reaction by labeling the MoFeP active-site component with a ruthenium photosenzitizer and thus bypasses the

need for the FeP reductase protein.[18] In these experiments, they were able to show light-driven six-electron catalytic reduction of hydrogen cyanide to form methane and ammonia as detected by gas chromatography mass spectrometry (GC-MS).

Two more examples come from systems involving cytochromes P450 (CYP) where the required first reduction step is achieved by external light-driven "reductases." These studies are of particular interest as the first turnover of NOS is thought to follow similar steps to the catalytic cycle of P450 (refer to Figure 4.1). It was recently demonstrated that an engineered *in vitro* system using isolated photosystem I (PSI) and isolated membrane-bound P450 can carry out hydroxylation chemistry.[19] In these experiments, PSI provides light-driven electron transport through a ferredoxin mediator to CYP79A1, which catalyzes the transformation of L-tyrosine to (*E/Z*)-*p*-hydroxyphenylacetaldoxime. In another example, a ruthenium-modified P450-BM3 system was shown to selectively hydroxylate lauric acid under steady illumination with visible light.[20] Reductive flash-quench conditions were used to drive the necessary heme reduction to initiate catalysis in the presence of substrate, O_2, and the sacrificial quencher sodium diethyldithiocarbamate (DTC) (Scheme 4.2). Product formation was monitored by gas chromatography following derivatization of the functional groups.

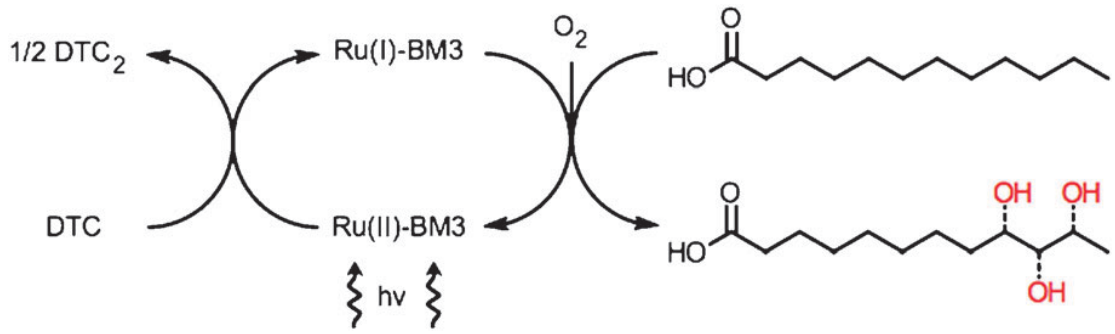

Scheme 4.2 Proposed photocatalytic cycle for ruthenium-modified P450-BM3 enzymatic hydroxylation of lauric acid. Scheme reproduced from Tran.[20]

We have successfully bypassed the need for a reductase domain and achieved phototriggered heme reduction of $Ru(II)_{K115C}$-gsNOS in the presence of each substrate and cofactor under reductive flash-quench conditions (chapter three). Inspired by the previously summarized studies of light-driven catalysis and with the desire to test the full enzymatic efficacy of our ruthenium-modified gsNOS system, experiments were designed to drive the catalytic NOS cycle using steady-state illumination with visible light. Since the biological products of this reaction are NO and L-citrulline, different detection assays are needed. The experimental setup, detection methods, and results are described in this chapter.

4.2 Results and Discussion

Photocatalytic Cycle of $Ru(II)_{K115C}$-gsNOS

In order to confirm enzymatic activity of the ruthenium-modified gsNOS system ($Ru(II)_{K115C}$-gsNOS) reductive flash-quench experiments were performed under steady-state illumination (Scheme 4.3). Blue light (470 nm) from a light emitting diode (LED) was used to excite the $[Ru(bpy)_2(IA\text{-}phen)]^{2+}$ label. The irreversible and water-soluble quencher, sodium diethyldithiocarbamate (DTC), was used as a sacrificial electron donor to reduce the excited state of the ruthenium label. This Ru(I) species can then inject electrons into the heme of the gsNOS active site and hopefully initiate catalysis in the presence of O_2, substrate and the redox-active cofactor, H_4B. The full cycle begins with L-Arg, however NO and L-Cit can be produced starting with the native intermediate, NOHA. Reactions with both substrates were investigated, as the frequency of electron

transfer under these conditions may not be enough to get around the cycle twice starting with L-Arg.

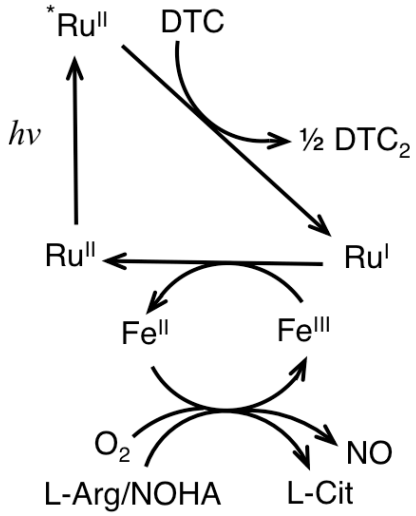

Scheme 4.3 Proposed photocatalytic cycle for light-driven gsNOS catalysis. Ru represents $[Ru(bpy)_2(IA\text{-}phen)]^{2+}$ attached to gsNOS, Fe represents the heme active site of gsNOS.

Detection of Photocatalytic Production of NO (by Griess Assay)

The biological products of the NOS cycle are NO and L-Cit. There are a few different options for the detection of NO, including NO-sensitive electrodes[21] and NO-specific fluorescent probes.[22] However NO reacts quickly in oxygenated water to form other NO_x species, namely nitrate (NO_3^-) and nitrite (NO_2^-). The colorimetric Griess Assay (Cayman Chemicals) provides a convenient way to quantify the sum of these NO metabolites *in vitro* which are proportional to the amount of NO originally present in solution. The assay is based on reaction of NO_2^- with Griess reagents to form a highly colored azo dye product (Scheme 4.4).[23]

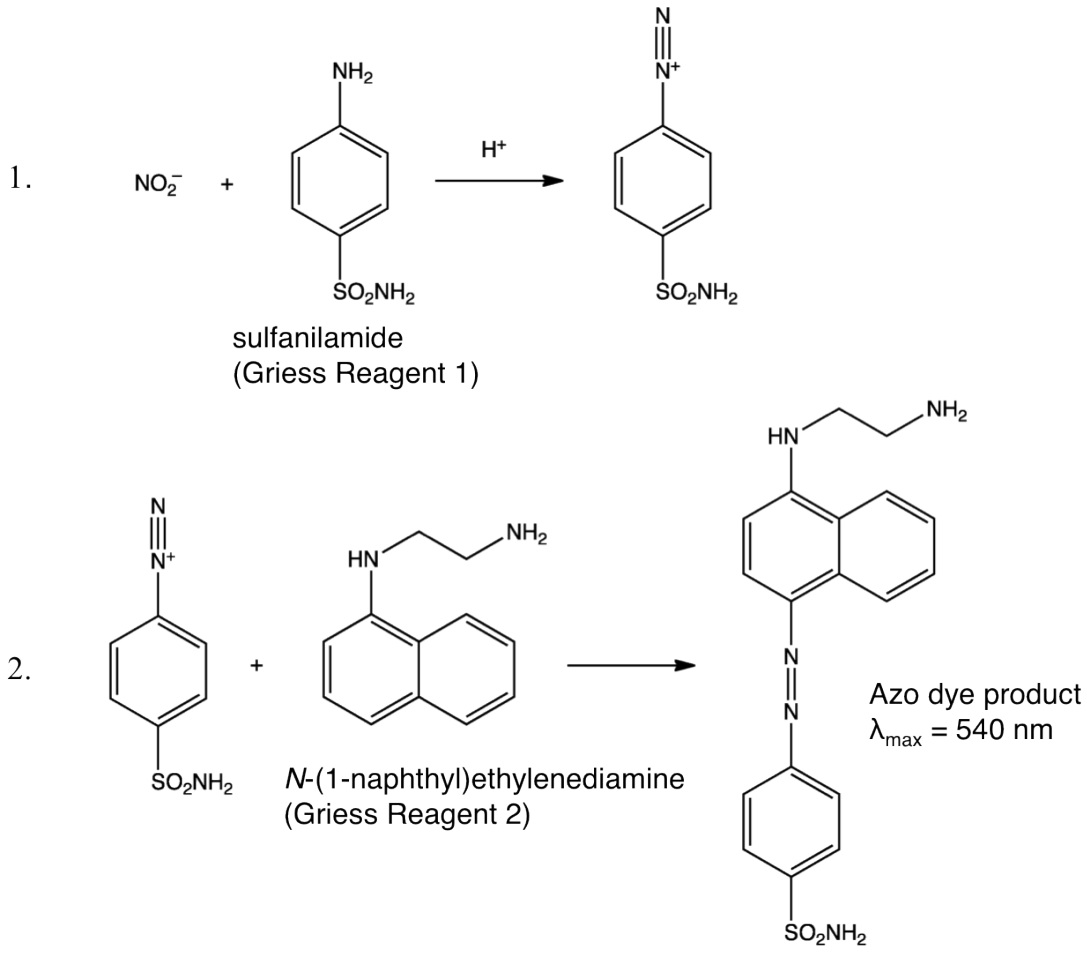

Scheme 4.4 Griess Assay reactions for the colorimetric detection of nitrites in solution. The final product is bright pink with a maximum absorbance at 540–550 nm.

Calibration curves were made for each set of experiments by reacting known amounts of NO_3^- and NO_2^- standards with Griess reagents and plotting the resulting absorbance at 550 nm (or 540 nm) as a function of combined NO_3^- and NO_2^- concentration. The absorbance spectra and calibration curve for a typical set of experiments are shown below (Figures 4.2 and 4.3)

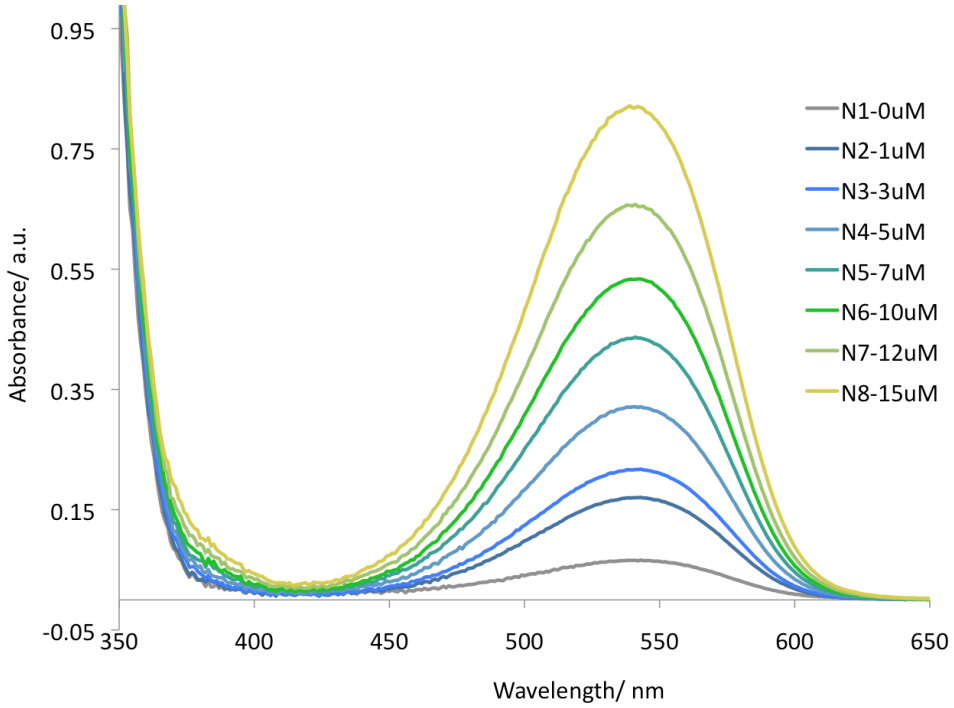

Figure 4.2 Absorbance spectra for nitrate and nitrite standards used in Griess Assay. There is a slight absorbance for the 0 μM nitrate standard solution that may come from trace amounts of nitrates in the buffer or nitrate reductase enzyme solution supplied with the kit.

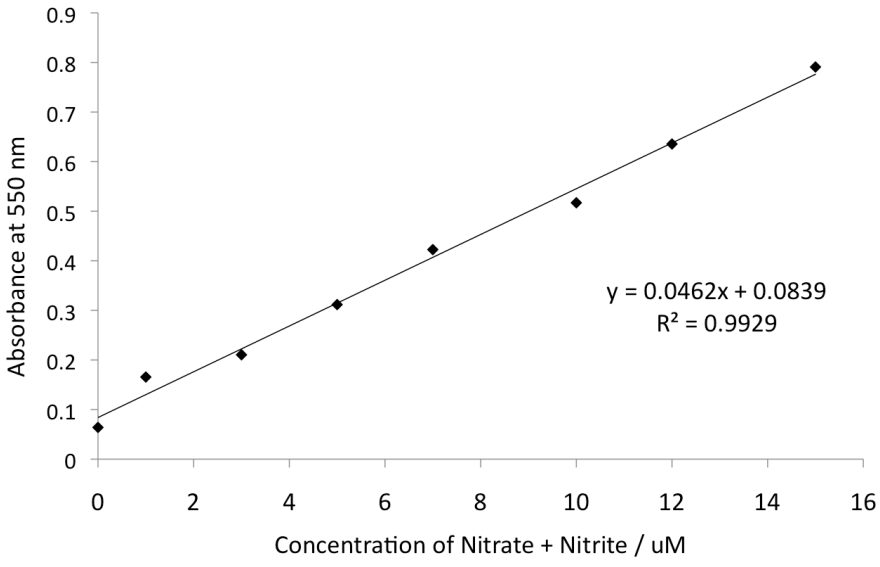

Figure 4.3 Calibration curve for nitrate and nitrite standards used in Griess Assay. Absorbance at 550 nm was determined to be more suitable for samples containing the full reaction mixture to avoid any residual protein absorbance. Comparative curves made with absorbance at 540 nm showed identical slopes.

The total concentration of NO_x from unknown samples can then be calculated from the following equation:

$$[NO_3^- + NO_2^-] = \left[\frac{(A_{550} - y_{int})}{slope}\right](dilution) \qquad \text{(eqn 4.1)}$$

In a typical experiment, an aerated solution of $Ru(II)_{K115C}$-gsNOS in sodium phosphate buffer, pH 7 was loaded with substrate (either L-Arg or NOHA) and the H_4B cofactor, combined with the DTC quencher, and irradiated with 470 nm light from an LED. After the irradiation period, the reaction is incubated with nitrate reductase to convert NO_3^- to NO_2^- and ensure that all produced NO_x species are accounted for,[24] before reaction with Griess reagents. The addition of Griess Reagents to the reaction mixture results in protein denaturation, and samples were centrifuged to remove any precipitated material before being carefully transferred to a cuvette for absorbance measurements. Representative spectra comparing the Griess products of a light-driven reaction using the intermediate NOHA as substrate with a dark control are shown in Figure 4.4. Calculations from the associated calibration curve give $[NO_2^-] = [NO] \sim 30$ μM in the final reaction mixture.

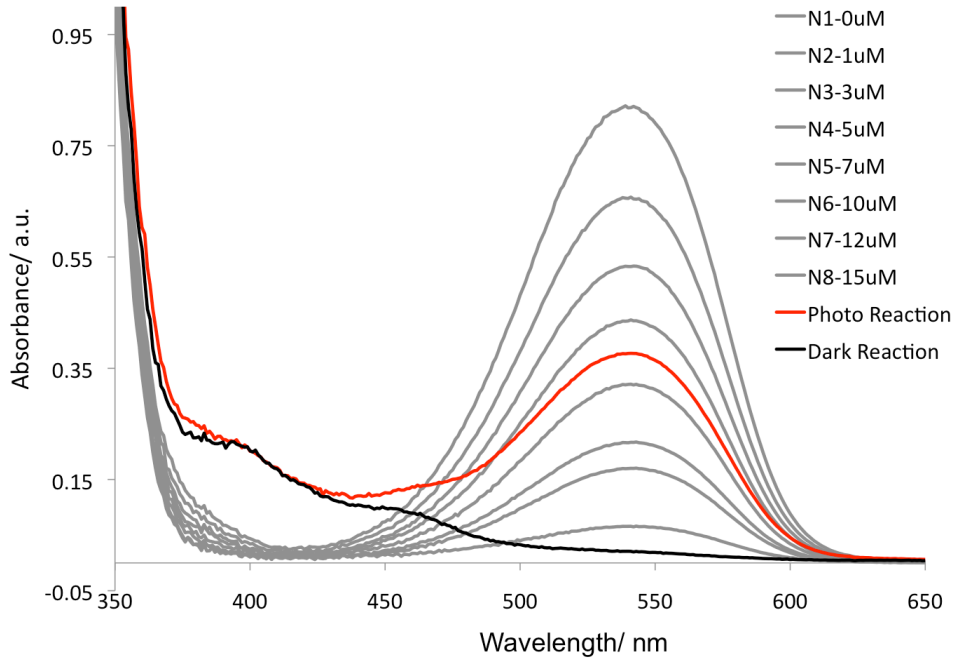

Figure 4.4 Typical raw absorbance spectra for Griess Assay comparing results for the photo-reaction of our labeled $Ru(II)_{K115C}$-gsNOS system and the dark control. Nitrate standards shown in gray. [$Ru(II)_{K115C}$-gsNOS] = 10 μM, [NOHA] = 200 μM, [H_4B] = 60 μM, [DTC] = 200 μM, in 50 mM phosphate buffer, pH 7. Reaction was illuminated at 470 nm for 30 min.

The same experiments were performed with L-Arg as the substrate, however the amount of NO produced (as measured from NO_2^- concentration) was markedly lower. Given the relatively large concentration of starting L-Arg compared to the amount of the NOHA intermediate formed in a single turnover, it is possible that another molecule of L-Arg simply rebinds before a second electron can be injected to finish the cycle. In such a scenario, very little NO_x would be produced. In an effort to give the enzyme enough time or electrons to get around the cycle twice, illumination was increased to 4.5 and 10.5 hours. In all cases, side-by-side comparisons of data from the Griess Assay showed approximately 5–6 times more NO produced from NOHA vs. L-Arg as substrate. While

reactions with L-Arg as substrate produced substantially less NO_x than with NOHA, the fact that increasing reaction time lead to any increased product was encouraging.

To explore the extent of catalytic activity, various time-course experiments were conducted with the fully loaded $Ru(II)_{K115C}$-gsNOS system using NOHA as substrate (NOHA was used in these experiments as it gave the most consistent signals *cf* L-Arg). Reactions were set up in parallel under identical conditions (to the best of my pippeting ability) and illuminated for various times between 15 min and 10 hr. Data from 15 min through 4 hr 30 min as well as a dark control are shown in Figure 4.5. Data from samples illuminated for longer times was omitted from the graph as further dilutions were necessary to maintain OD < 1; these data are represented in the time plot in Figure 4.6. Production of NO (as measured from NO_2^- concentration) leveled off at 7 hrs with $[NO_2^-]$ ~ 150 μM. The initial conditions were 10 μM enzyme with 200 μM NOHA and 200 μM DTC, meaning that up to 15 turnovers have been achieved per enzyme using this light-driven scheme. This leveling off could be due to running out of NOHA substrate or the irreversible DTC quencher. Precipitation of the NOS enzyme upon photodamage is also a likely problem. UV-visible absorption spectra were recorded of the longer timescale reactions before addition of Griess reagents (and thus before full protein denaturation) that showed appreciable amounts of heme Soret along with baseline scatter indicative that some amount of enzyme had precipitated by this point (not shown).

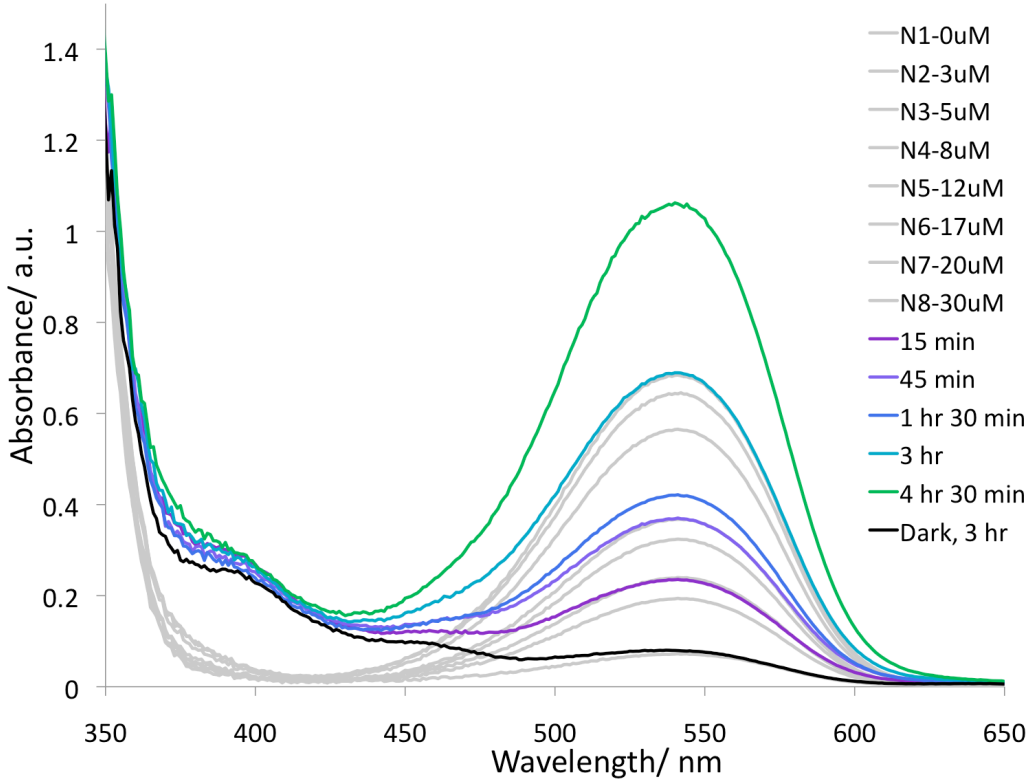

Figure 4.5 Raw absorbance data from Griess Assay of the photoreaction of $Ru(II)_{K115C}$-gsNOS system at different illumination times between 15 min and 4.5 hr. Nitrate standards are shown in gray. [$Ru(II)_{K115C}$-gsNOS] = 10 μM, [NOHA] = 200 μM, [H_4B] = 60 μM, [DTC] = 200 μM, in 50 mM phosphate buffer, pH 7.

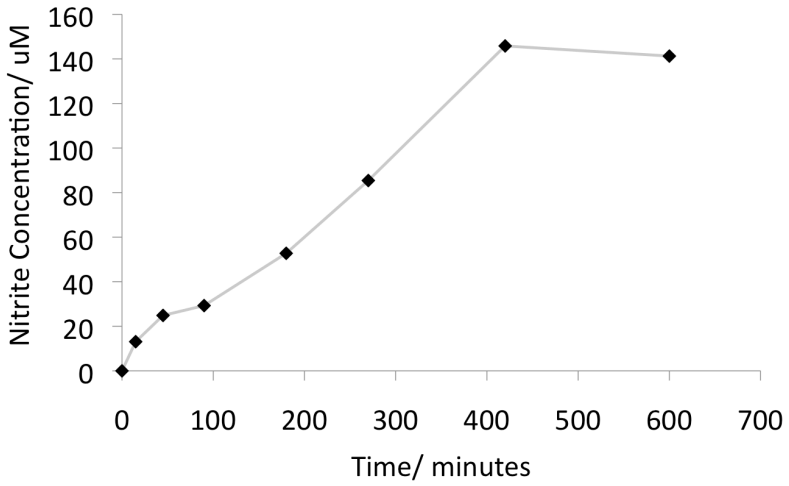

Figure 4.6 Plot of nitrite concentration vs. time as measured from absorbance at 550 nm from Griess Assay. NO production seems to level off at approximately 7 hr reflecting either exhausted supply of substrate or enzyme degradation. Raw data and reaction conditions are given in Figure 4.5. These measurements were made in duplicate.

Controls

Various control reactions were performed in addition to the dark measurements shown in the previous data. As expected, the removal of substrate results in no appreciable formation of NO (signals in the range of 0 μM nitrate standard). Removal of either DTC or H_4B or both yields interesting results. These controls investigate the role of reducing equivalents: DTC is needed to quench the *Ru(II) excited state and form the Ru(I) responsible for injecting electrons into the heme active site of our labeled gsNOS system (Scheme 4.3), and H_4B is needed to supply the second electron in the biological catalytic cycle. It was initially expected that removal of these components would shut down the cycle, however the data show only reduced NO production (approximately a third of NO produced from the fully loaded system). Given the steady-state illumination conditions, it is possible that *Ru(II) itself is supplying the electrons or that another NO_x-producing mechanism is at work. The triplet excited state of ruthenium(II) diimine complexes can be quenched by oxygen to form reactive oxygen species (ROS).[25] Quenching by energy transfer processes results in formation of singlet oxygen and by electron transfer results in superoxide. ROS in solution could interact with the O-H bonds in NOHA via radical reactions to produce variable amounts of NO_x and thus give positive signals in the Griess Assay. Another possibility comes from minor formation of peroxide. In the P450 and NOS cycles, it has been proposed that hydrogen peroxide can replace the chemically similar two-electron reduced molecular oxygen to access the hydroperoxo ferriheme intermediate via a so-called "peroxide shunt."[26–28] Control reactions with unlabeled gsNOS loaded with NOHA, plus the $[Ru(bpy)_2(A\text{-}phen)]^{2+}$ model complex in solution, show similar amounts of NO production (regardless of DTC or H_4B). However,

controls with unlabeled protein loaded with NOHA, H_4B, and DTC (without any ruthenium complexes) show negligible Griess signals, as do the same samples free of substrate. These controls support the idea that it is the presence of the $[Ru(bpy)_2(A\text{-}phen)]^{2+}$ complex (either attached to the protein, or free in solution) that creates the background signals associated with transformation of NOHA to NO_x possibly via some sort of ROS reaction. To summarize, only the removal of $[Ru(bpy)_2(A\text{-}phen)]^{2+}$, substrate, or light results in complete shutdown of NO_x production. Representative control data are compiled in Table 4.1

Table 4.1 Representative data from photoreaction controls. [NO_x] was measured from Griess Assay as previously described. All samples (except dark control) were illuminated for 45 minutes. Note that [NO_x] = 1 μM (+/-1) comes from signals in the range of the 0 μM nitrate standard and is considered negligible. Each measurement was made in triplicate.

System	[NO_x]/μM	System	[NO_x]/μM
RuNOS + DTC + H_4B + NOHA + Light	30 (+/- 4)	gsNOS + Ru Model + DTC + H_4B + NOHA + Light	8 (+/- 2)
RuNOS - DTC + H_4B + NOHA + Light	8 (+/- 2)	gsNOS + Ru Model - DTC + H_4B + NOHA + Light	8 (+/- 2)
RuNOS + DTC - H_4B + NOHA + Light	15 (+/-3)	gsNOS + Ru Model - DTC - H_4B + NOHA + Light	8 (+/- 2)
RuNOS - DTC - H_4B + NOHA + Light	8 (+/- 2)	gsNOS + Ru Model + DTC + H_4B - NOHA + Light	1 (+/- 1)
RuNOS + DTC + H_4B - NOHA + Light	1 (+/- 1)	gsNOS + DTC + H_4B + NOHA + Light	1 (+/- 1)
RuNOS + DTC + H_4B + NOHA - Light	1 (+/- 1)	Ru Model + DTC + H_4B + NOHA + Light	3 (+/- 1)

Inhibitors

The ability of our labeled $Ru(II)_{K115C}$-gsNOS system to produce NO in the presence of various inhibitors and substrate analogs was explored. As discussed in the previous section, control experiments with illuminated samples containing NOHA and the $[Ru(bpy)_2(A\text{-}phen)]^{2+}$ complex (either free in solution or bound to gsNOS), but in the absence of quencher and redox-active cofactor, still showed some amount of NO_x production. These NO_x species could be produced through noncatalytic routes activated by ROS formation. One way to help verify that NO specifically is being produced in the fully loaded system is to introduce an inhibitor. If the Griess signals are all simply the result of NO_x formed from ROS interactions with NOHA in solution, then addition of an inhibitor should have no effect. If the amount decreases, then that suggests gsNOS catalyzed NO formation.

Recent work with NOS from *Bacillus subtilis* (bsNOS) compared binding interactions of a number of substrates and inhibitors.[29] Additionally, they investigated the ability of bsNOS to catalyze the oxidation of L-Arg by H_2O_2 in the presence of these substrate analogs. Their data showed reasonable binding affinities for N^{ω}-methyl-L-arginine (Me-L-Arg, $k_{s,app}$ = 5.3 μM) and N^{ω}-nitro-L-arginine (NO_2-L-Arg, $k_{s,app}$ = 0.5 μM) as compared to L-Arg ($k_{s,app}$ = 5.0 μM). These values of $k_{s,app}$ are apparent dissociation constants and were calculated from difference spectra in competitive binding studies with imidazole. Furthermore, the presence of either Me-L-Arg or NO_2-L-Arg lead to 95% inhibition of L-Cit formation in the H_2O_2 oxidation of L-Arg. As such, Me-L-Arg or NO_2-L-Arg were chosen as good initial substrate-analogs for our studies of light-driven catalysis with $Ru(II)_{K115C}$-gsNOS (Figure 4.7).

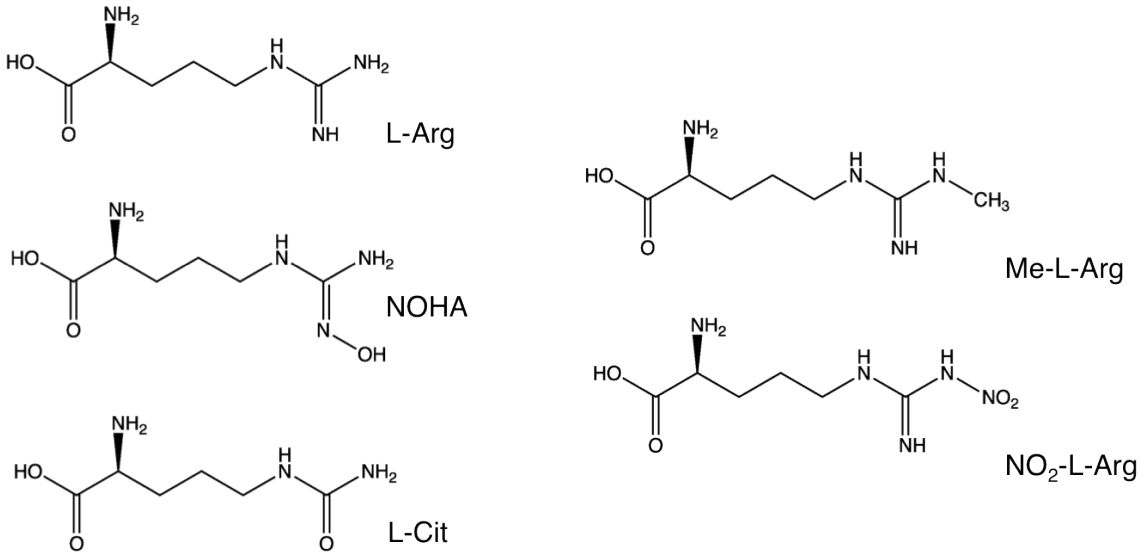

Figure 4.7 Structures of the natural NOS substrates and product compared with two L-Arg substrate analogs.

Experiments were performed as previously outlined, except with the addition of either Me-L-Arg or NO_2-L-Arg. A typical sample contained an aerated solution of $Ru(II)_{K115C}$-gsNOS in sodium phosphate buffer, pH 7 that was first loaded with substrate (NOHA) to ensure initial binding. The H_4B cofactor and DTC quencher were added, followed by addition of the substrate analog (Me-L-Arg or NO_2-L-Arg) in a 1:1 ratio of NOHA:inhibitor. The samples were irradiated with 470 nm light from an LED. The Griess Assay was then performed as described above. Additional controls were performed in the absence of NOHA, as well as in the absence of protein/ruthenium complex (to ensure that the NO_2 group of NO_2-L-Arg did not provide any interference with the Griess Assay). The results are summarized in Table 4.2

Table 4.2 Representative data from $Ru(II)_{K115C}$-gsNOS photoreaction in the presence of inhibitors/substrate-analogs. $[NO_x]$ was measured from Griess Assay as previously described. All samples were illuminated for 45 minutes. Note that $[NO_x]$ = 1 μM (+/-1) comes from signals in the range of the 0 μM nitrate standard and is considered negligible, N/D = not detectable. Measurements were made in triplicate.

System	$[NO_x]$/μM	System	$[NO_x]$/μM
RuNOS + DTC + H_4B + NOHA - Inhibitor + Light	30 (+/- 4)		
RuNOS + DTC + H_4B + NOHA + NO_2-L-Arg + Light	16 (+/- 2)	RuNOS + DTC + H_4B + NOHA + Me-L-Arg + Light	16 (+/- 3)
RuNOS + DTC + H_4B - NOHA + NO_2-L-Arg + Light	7 (+/- 2)	RuNOS + DTC + H_4B - NOHA + Me-L-Arg + Light	5 (+/- 2)
- RuNOS + DTC + H_4B - NOHA + NO_2-L-Arg + Light	1 (+/- 1)	- RuNOS + DTC + H_4B - NOHA + Me-L-Arg + Light	N/D

These data show that the photo-reaction of $Ru(II)_{K115C}$-gsNOS to produce NO from NOHA (as measured from NO_x) is substantially inhibited by the presence of Me-L-Arg or NO_2-L-Arg (by approximately 50%). This suggests that at a significant portion of the NO_x detected in the system fully loaded with NOHA is in fact coming from light-driven gsNOS catalysis.

Detection of Photocatalytic Production of L-citrulline (by LC-MS)

In order to corroborate the evidence from the Griess Assay that our ruthenium labeled gsNOS system is capable of light-driven catalysis, the reaction was analyzed for production of L-Cit using on-line liquid chromatography–mass spectrometry (LC–MS) and liquid chromatography tandem mass spectrometry (LC–MS–MS). Proteins can clog the LC columns and were thus excluded from the standard mixtures as well as filtered out from the actual photoreactions before application. Individual components were analyzed to acquire their retention times and electrospray ionization (ESI) mass spectra which are summarized in Table 4.3. Standard mixtures of all the reaction components (minus $Ru(II)_{K115C}$-gsNOS) were analyzed (Figure 4.8) to gauge conditions best suited for analyte separation (see materials and methods section for column information and optimized conditions).

Table 4.3 List of components in the standard mixture with their observed m/z and associated retention times

Component	Observed m/z (+ H^+)	Retention time (min)
L-Cit	176	1.5
H_4B	242	2.1
NOHA	191	5.2
Na^+ DTC	150	5.9

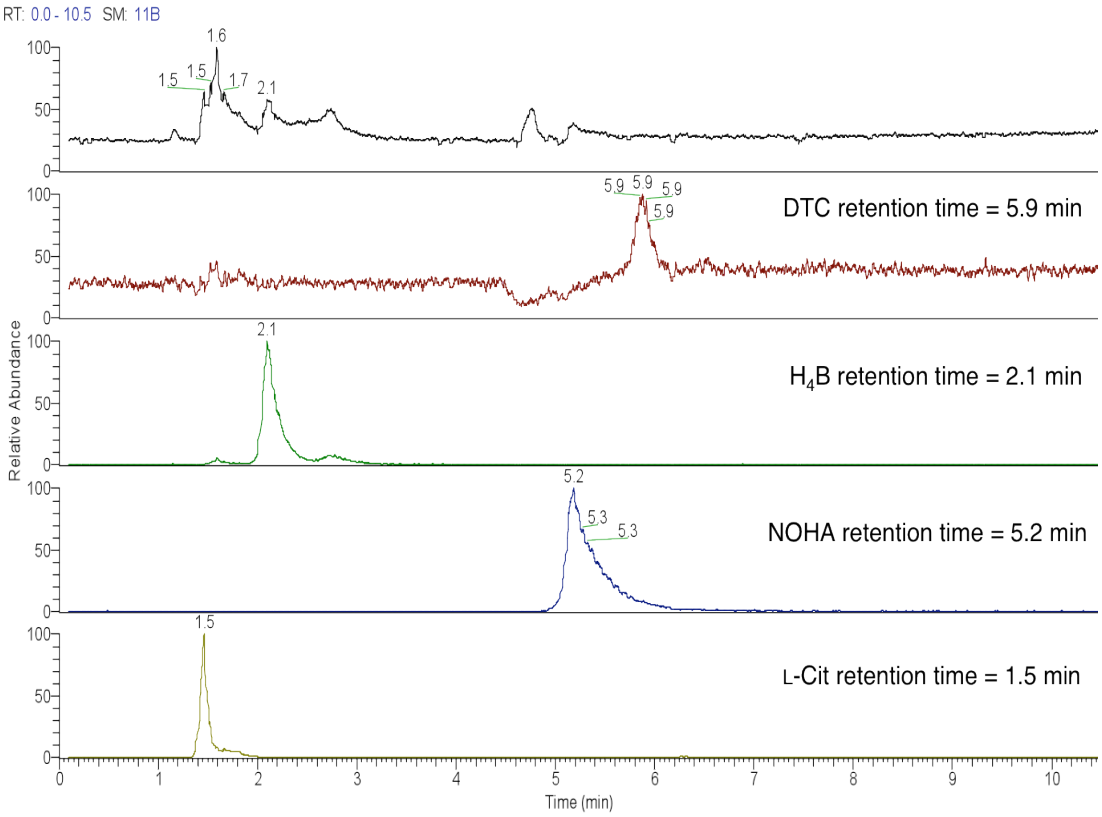

Figure 4.8 LC-MS chromatograms of standard reaction mixture off of PrimeSep Column directly interfaced to ESI source operating in positive ion mode.

Maintaining the same conditions used in the Griess Assay experiments, reactions were set up with an aerated solution of $Ru(II)_{K115C}$-gsNOS in sodium phosphate buffer, pH 7 and loaded with substrate (NOHA). The H_4B cofactor and the DTC quencher were added, and the mixture was irradiated with 470 nm light from an LED for 45 minutes. Following irradiation, the protein was removed using amicon micron centrifugal filter devices (10,000 MWCO) prior to LC–MS analysis. Formation of L-Cit was confirmed by both retention time and tandem mass fragmentation. A representative chromatogram and mass spectrum for the reaction are shown in Figure 4.9.

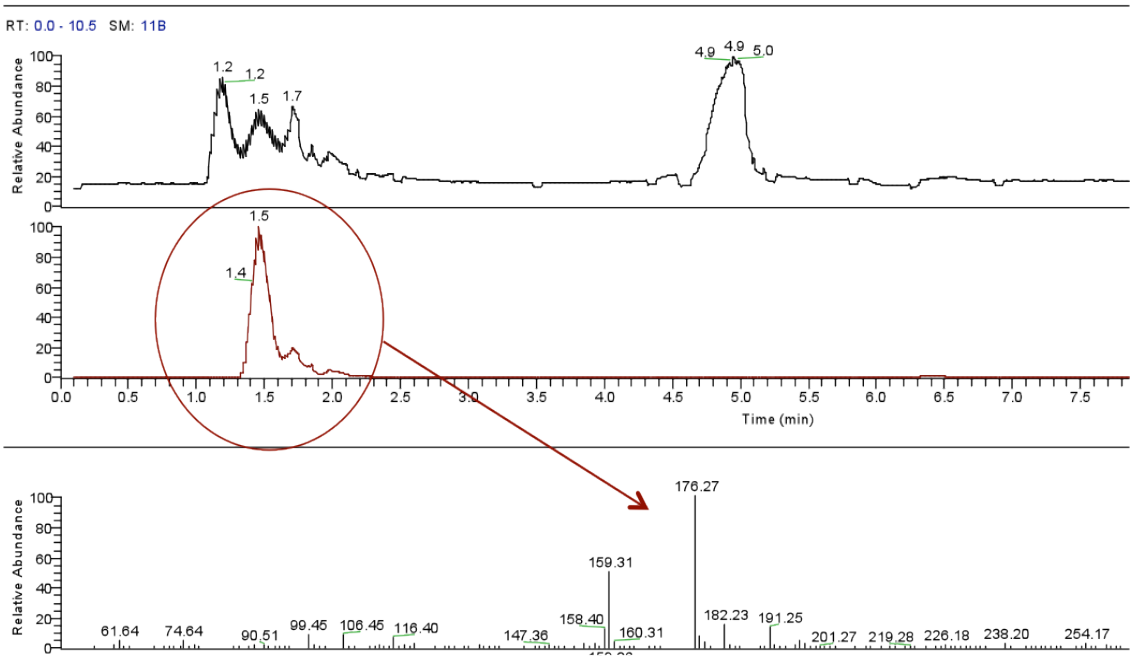

Figure 4.9 Confirmation of L-Cit production from the Ru(II)$_{K115C}$-gsNOS photoreaction by 1.5 min retention time and m/z = 176 from standards. All the other components are present, but not shown for clarity. The new peak with a 4.9 min retention is unassigned, however, there are other possible species present in the reaction mixture such as the DTC dimer formed in the irreversible reductive quenching of the *Ru(II) excited state that were not accounted for in the standards.

4.3 Conclusion

Experiments have been performed to test the efficacy of our photosensitizer-labeled gsNOS enzyme, Ru(II)$_{K115C}$-gsNOS, and excitingly, light-driven catalysis has been demonstrated under reductive flash-quench conditions. The Griess Assay was used to indirectly measure NO production via quantification of its NO_x metabolites in aqueous solution. LC-MS was used to directly detect L-citrulline as the other photoreaction product and its formation was confirmed both by retention time and tandem mass spec fragmentation. Given that NO production (measured by the Griess Assay) starting from L-Arg is low compared to NOHA, but still increases with reaction time, it would be very informative to repeat those conditions and use LC–MS to see if any amount of L-Cit is in

fact produced. Control reactions that remove the $[Ru(bpy)_2(A\text{-}phen)]^{2+}$ complex, the substrate NOHA, or the light source show almost complete shut-down of catalysis. Controls that contain the $[Ru(bpy)_2(A\text{-}phen)]^{2+}$ complex (either attached to the protein or free in solution) and NOHA, but remove either the DTC quencher or the H_4B cofactor still produce some amount of NO_x upon illumination. It is possible that these NO_x species are the result of *Ru(II) excited state quenching by oxygen to form ROS that can go on to do chemistry with the substrate. Two L-Arg analogs were investigated for their ability to inhibit NO production in the fully loaded $Ru(II)_{K115C}$-gsNOS system; addition of either Me-L-Arg or NO_2-L-Arg resulted in ~50% inhibition. Time-course reactions show maximum NO production of ~150 μM at 7 hours starting with 10 μM $Ru(II)_{K115C}$-gsNOS and 200 μM NOHA. While it is likely that some amount of unavoidable photooxidative damage to the protein occurs over time, it may be possible to boost NO production by increasing the starting concentration of substrate.

4.4 Acknowledgements

I deeply grateful to Dr. Mona Shahghali for her assistance with the LC–MS experiments, specifically for hunting down three different columns to run in nonstandard modes and for getting as excited as I was when we confirmed L-Cit production! Thanks also go to Maraia Ener and Dr. Jeff Warren for insightful discussions.

4.5 Materials and Methods

Materials

Labeled protein $Ru(II)_{K115C}$-gsNOS was prepared as described in chapter two of this thesis. The model complex $[Ru(bpy)_2(A\text{-}phen)]^{2+}$ was synthesized as described in chapter three. *Note:* all ruthenium(II) diimine-containing samples (model and protein) were kept covered in foil or handled under red light to prevent photodamage. L-arginine (L-Arg), N^{ω}-hydroxy-L-arginine acetate salt (NOHA), (6R)-5,6,7,8-tetrahydrobiopterin (H_4B), sodium diethyldithiocarbamate (DTC), N^{ω}-methyl-L-arginine (Me-L-Arg), and N^{ω}-nitro-L-arginine (NO_2-L-Arg) were all purchased from Sigma-Aldrich and used as received. NOHA, Me-L-Arg, and NO_2-L-Arg were all stored at 4 °C and freshly dissolved before each use. H_4B was stored at -20 °C. 50 mM sodium phosphate (NaPi) buffer, pH 7 was prepared using Milli-Q (18.2 MΩ) water and filtered (0.22 μm, Millipore) before use. The Nitrate/Nitrite Colorimetric Kit containing Greiss reagents, standards, and the nitrate reductase was purchased from Cayman Chemical Company.

Griess Assay

Griess Assays were performed according to the manufacturer's instructions with the following changes. Absorbance was measured in a 1 cm pathlength microcuvette (200 μL sample volume) instead of using the micro well plate supplied with the kit for use with an absorbance platereader. Due to the longer pathlength used in our experiments, nitrate/nitrite standard curves were made with more dilute solutions (0–15 μM) than outlined in the kit to keep absorbance < 1.

Typical experiments were set up in parallel, starting from freshly prepared stocks of each reaction component. Sample volumes were 80 μL and were made up in thin-walled PCR tubes (which are fairly transparent to visible light). Steady-state illumination was achieved using a 470 nm light emitting diode (LED, M470L1, Thorlabs) operating at the LED driver maximum current (~700 mA). Following the desired photoreaction time, 10 μL each of the nitrate reductase and cofactor mixture were added and incubated in the dark at room temperature for 1 hour. 50 μL Griess Reagent 1 was added, immediately followed by 50 μL Griess Reagent 2 bring the final volume to 200 μL. The color was allowed to develop for 10 min before recording absorbance. UV-visible absorption spectra were recorded on an Agilent 8453 UV-vis Spectrophotometer. Data were processed using Microsoft Excel (cringe).

Liquid Chromatography-Tandem Mass Spectrometry

The formation of L-citrulline was confirmed using on-line liquid chromatography-mass spectrometery (LC–MS) and liquid chromatography tandem mass spectrometry (LC–MS–MS) in the Mass Spectrometry Facility at the California Institute of Technology. The LC system consisted of an Accela 600 pump (Thermofisher, USA), an Accela Open CTC PAL Autosampler (CTC Analytics, Switzerland), and an external column heater (Supelco, USA). The LC columns were interfaced directly to an electrospray ionization (ESI) source (Thermofisher, USA) of an LTQ linear ion trap mass spectrometer, operated in the positive ion mode, and spectra were acquired from *m/z* 50 to 300 over the length of the chromatographic run. In some experiments, tandem MS was utilized for full confirmation by retention time, mass, and fragment analysis.

DTC, NOHA, and L-Cit are all polar molecules and were thus expected to have very short retention times on the more typically used reversed phase LC columns. Three different columns were evaluated for their ability to separate trace amounts of L-Cit amongst much higher component concentrations: 1) Cogent Hydride column (MicroSolv, USA), 2.1 i.d. x 50 mm, 4.2 µm particle, 100 Å pore size, operated in normal phase separation mode, 2) Acquity UPLC BEH Amide column (Waters, USA), 2.1 i.d. x 150 mm, 4.2 µm particle, 100 Å pore size, operated in hydrophobic interaction liquid chromatography (HILIC) separation mode, and 3) PrimeSep A column (SIELC Technologies, USA) 2.1 mm i.d. x 100 mm, 5 µm particle, 100 Å pore size, operated in mixed mode chromatography, reversed-phase ion-exchange separation mode. The PrimeSep A column (3) gave the most consistent separation and was the most tolerant of the high-salt reaction conditions (50 mM buffer). Optimized conditions were as follows:

Mobile Phase A: 20 mM ammonium formate in 30% acetonitrile
Mobile Phase B: 50 mM ammonium formate in 50% acetonitrile
Flow Rate: 200 µL/min
Column Temperature: 40 °C
Sample Injection Volume: 5 µL

Analytes were eluted with the following gradient:

Time 0.00 min 0%B
Time 0.50 min 0%B
Time 10.00 min 100%B
Time 11.00 min 0%B
Time 14.00 min 0%B

Since the actual amount of L-Cit produced in the reaction would be much less than that in the standards, a low detection limit was explored. A sample containing 60 pmoles of pure L-Cit was run and clearly detected under these conditions (Figure 4.10).

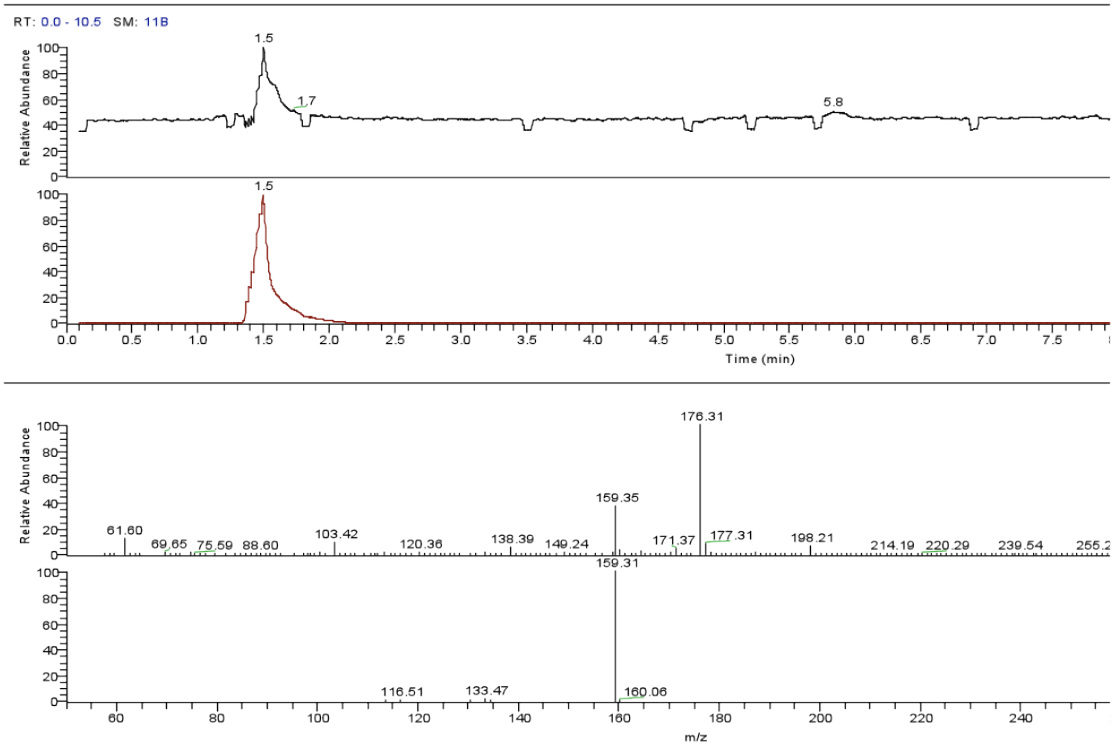

Figure 4.10 LC tandem MS of 60 pmoles L-Cit standard loaded onto PrimeSep A column, showing 1.5 min retention time and a detected m/z = 176.

4.6 References

1. Marletta, M. A. Nitric Oxide Synthase Structure and Mechanism. *J Biol Chem* **268**, 12231-12234 (1993).
2. Alderton, W. K., Cooper, C. E., Knowles, R. G. Nitric Oxide Synthase: Structure, Function, and Inhibition. *Biochem J* **357**, 593-615 (2001).
3. Stuehr, D. J. Update on Mechanism and Catalytic Regulation in the NO Synthases. *J Biol Chem* **279**, 36167–36170 (2004).
4. Crane, B. R., Sudhamsu, J. & Patel, B. A. Bacterial Nitric Oxide Synthases. *Annu Rev Biochem* **79**, 445–470 (2010).
5. Stuehr, D. Oxygen Reduction by Nitric-oxide Synthases. *J Biol Chem* **276**, 14533–14536 (2001).
6. Agapie, T. *et al.* NO formation by a catalytically self-sufficient bacterial nitric oxide synthase from Sorangium cellulosum. *Proc Nat Acad Sci USA* **106**, 16221–16226 (2009).
7. Zhu, Y. & Silverman, R. B. Revisiting Heme Mechanisms. A Perspective on the Mechanisms of Nitric Oxide Synthase (NOS), Heme Oxygenase (HO), and Cytochrome P450s (CYP450s). *Biochemistry* **47**, 2231–2243 (2008).
8. Wei, C.-C., Crane, B. R. & Stuehr, D. J. Tetrahydrobiopterin Radical Enzymology. *Chem Rev* **103**, 2365–2384 (2003).
9. Davydov, R. *et al.* EPR and ENDOR Characterization of Intermediates in the Cryoreduced Oxy-Nitric Oxide Synthase Heme Domain with Bound l-Arginine or N G Hydroxyarginine. *Biochemistry* **41**, 10375–10381 (2002).
10. Woodward, J. J., Chang, M. M., Martin, N. I. & Marletta, M. A. The Second Step of the Nitric Oxide Synthase Reaction: Evidence for Ferric-Peroxo as the Active Oxidant. *J Am Chem Soc* **131**, 297–305 (2009).
11. Chang, I. J., Gray, H. B. & Winkler, J. R. High-driving-force electron transfer in metalloproteins: intramolecular oxidation of ferrocytochrome c by Ru (2, 2'-bpy) 2 (im)(his-33) 3+. *J Am Chem Soc* **113**, 7056–7057 (1991).
12. Huynh, M. H. V., Dattelbaum, D. M. & Meyer, T. J. Exited state electron and energy transfer in molecular assemblies. *Coord Chem Rev* **249**, 457–483 (2005).
13. Berglund, J., Pascher, T., Winkler, J. R., Gray, H. B. Photoinduced Oxidation of Horseradish Peroxidase. *J Am Chem Soc* **119**, 2464-2469 (1997).
14. Low, D., Winkler, J. R., Gray, H. B. Photoinduced Oxidation of Microperoxidase-8: Generation of Ferryl and Cation-Radical Porphyrins. *J Am Chem Soc* **118**, 117-120 (1996).
15. Ener, M. E., Lee, Y. T., Winkler, J. R., Gray, H. B. & Cheruzel, L. Photooxidation of cytochrome P450-BM3. *Proc Nat Acad Sci USA* **107**, 18783–18786 (2010).
16. Mines, G. A., et al. Rates of Heme Oxidation and Reduction in Ru(His33)cytochrome c at Very High Driving Forces. *J Am Chem Soc* **118**, 1961-1965 (1996).
17. Sono, M., Roach, M. P., Coulter, E. D., Dawson, J. H., Heme-Containing Oxygenases. *Chem Rev* **96**, 2841-2887 (1996).

18. Roth, L. E. & Tezcan, F. A. ATP-Uncoupled, Six-Electron Photoreduction of Hydrogen Cyanide to Methane by the Molybdenum–Iron Protein. *J Am Chem Soc* **134**, 8416–8419 (2012).
19. Jensen, K., Jensen, P. E. & Møller, B. L. Light-Driven Cytochrome P450 Hydroxylations. *ACS Chem Biol* **6**, 533–539 (2011).
20. Tran, N.-H. *et al.* Light-initiated hydroxylation of lauric acid using hybrid P450 BM3 enzymes. *Chem Commun* **47**, 11936 (2011).
21. Davies, I. R. & Zhang, X. Nitric Oxide Selective Electrodes. *Methods in Enzymology* **436**, 63–95 (2008).
22. Lim, M. H. Preparation of a copper-based fluorescent probe for nitric oxide and its use in mammalian cultured cells. *Nat Protoc* **2**, 408–415 (2007).
23. Green, L.C. et al. Analysis of Nitrate, Nitrite, and [15N]Nitrate in Biological Fluids. *Anal Biochem* **126**, 131-138 (1982).
24. Verdon, C. P., Burton, B. A., Prior, R. L. Sample Pretreatment with Nitrate Reductase and Glucose-6-Phosphate Dehydrogenase Quantitatively Reduces Nitrate... *Anal Biochem* **224**, 502-508 (1995).
25. Timpson, C. J., Carter, C. C. & Olmsted III, J. Mechanism of quenching of electronically excited ruthenium complexes by oxygen. *J Phys Chem* **93**, 4116–4120 (1989).
26. Nordblom, G. D., White, R. E. & Coon, M. J. Studies on hydroperoxide-dependent substrate hydroxylation by purified liver microsomal cytochrome P-450. *Arch Biochem Biophys* **175**, 524–533 (1976).
27. Joo, H., Lin, Z., Arnold, F. H. Laboratory evolution of peroxide-mediated cytochrome P450 hydroxylation. *Nature* **399**, 670-673 (1999).
28. Pufahl, R. A., Wishnok, J. S. & Marletta, M. A. Hydrogen peroxide-supported oxidation of NG-hydroxy-L-arginine by nitric oxide synthase. *Biochemistry* **34**, 1930–1941 (1995).
29. Salard-Arnaud, I., Stuehr, D., Boucher, J.-L. & Mansuy, D. Spectroscopic, catalytic and binding properties of Bacillus subtilis NO synthase-like protein: Comparison with other bacterial and mammalian NO synthases. *J Inorg Biochem* **106**, 164–171 (2012).

Chapter Five

DIATOMIC MOLECULE BINDING IN RUTHENIUM-MODIFIED NITRIC OXIDE SYNTHASE FROM *GEOBACILLUS STEAROTHERMOPHILUS*

5.1 Introduction

The radical nitric oxide (NO), is now recognized as an essential biological regulator after having been long considered solely a poison and pollutant.[1] NO has many roles, such as an endothelian relaxing factor, a protective immunocytotoxin, and as a signaling molecule in the nervous system.[2] NO is produced in mammals by a family of nitric oxide synthases (mNOS). mNOS catalyzes the oxidation of L-arginine (L-Arg) to L-citrulline (L-Cit) + NO. The reaction proceeds in two turnovers with N^{ω}-hydroxy-L-arginine (NOHA) as a stable bound intermediate.[3] All mNOS isoforms are homodimers that contain an oxygenase domain linked to a reductase domain.[4] The oxygenase domain houses a cysteine-ligated heme, as well as substrate and redox cofactor binding sites that form the catalytic active site of the enzyme. The calmodulin-linked reductase domain is a source of electrons and has binding sites for flavin adenine dinucleotide (FAD), flavin mononucleotide (FMN), and nicotinamide adenine dinucleotide phosphate (NADPH).[3] Chapter one contains a more detailed description of the domains of mNOS enzymes.

Monooxygenases, including chloroperoxidase (CPO), cytochromes P450, and NOS, belong to the heme-thiolate superfamily of enzymes that activate dioxygen (O_2) to oxegenate substrates.[5] While the full two-step mechanism of NO production by NOS is not yet fully understood,[6] the first turnover is thought to follow a cycle similar to the well-studied P450s. The NOS resting state is a six-coordinate mixed-spin ferric-aquo heme. Substrate binding in the pocket displaces water to form a five-coordinate high-spin ferric state. In the first turnover, L-Arg is converted to NOHA. Ferric NOS is supplied with an electron from the reductase domain to give a ferrous species that can bind O_2. Oxygen binding gives a ferrous-oxy complex, that is further reduced by one electron

coming from the unique redox cofactor (6R)-5,6,7,8-tetrahydrobiopterin (H_4B).[7] To date, the next experimentally observed species is the ferric resting state with bound NOHA. The second turnover of the catalytic cycle has similar steps: reduction, O_2-binding, and reduction by H_4B. From there, the next observed species is the ferric-NO, which then releases NO. The missing reactive intermediates involved in these heme-based oxygenations are thought to be a ferryl porphyrin radical cation (analogous to compound I in P450) in the first turnover and either a hydroperoxo ferriheme or Cpd I formed by subsequent protonation/water loss in the second[8,9] (Figure 5.1).

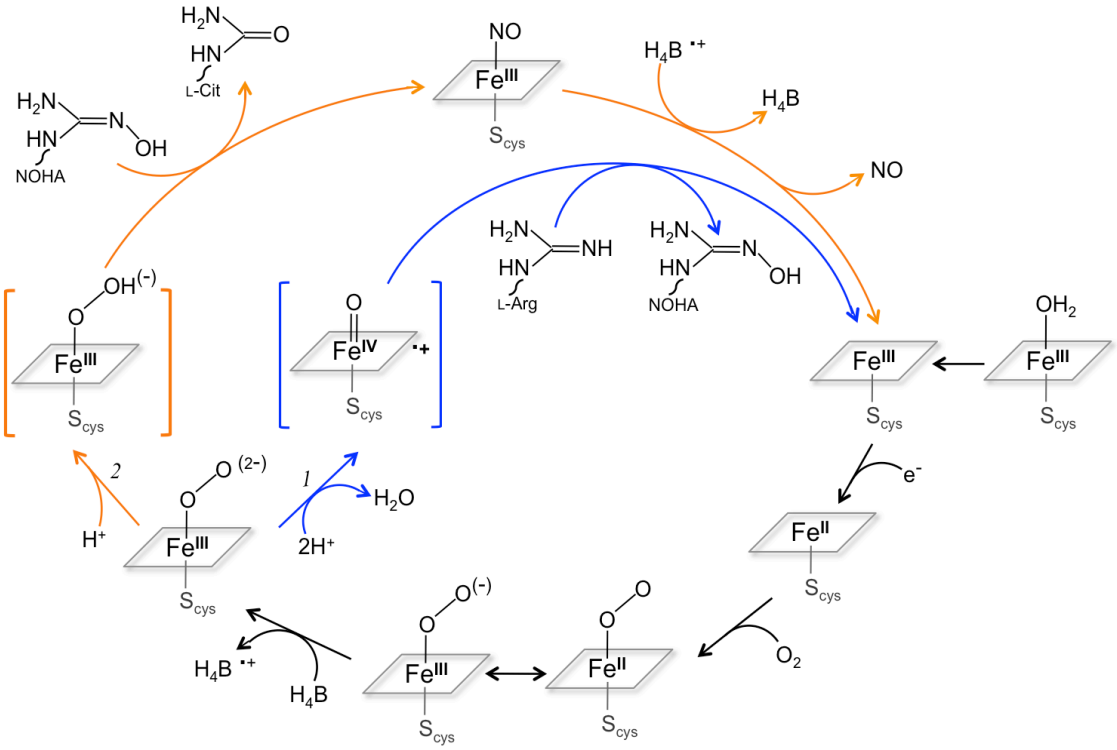

Figure 5.1 Putative mechanism for the catalytic production of NO by NOS enzymes: (1) first turnover formation of NOHA from L-Arg, shown in blue path; (2) second turnover formation of L-Cit and NO radical from NOHA, shown in orange path. The proposed oxygenating intermediates are in brackets.

Many bacterial NOS homologs have been identified that exhibit NOS-like activity.[10] The role of NO in prokaryotes remains an open question, but *in vivo* NO

production has been confirmed.[11] A key difference between bacterial NOS and mNOS is the absence of a linked reductase domain. Three bacterial forms of NOS have been crystallized from *Bacillus subtilis* (bsNOS),[12] *Staphylococcus aureus* (saNOS),[13] and *Geobacillus stearothermophilus* (gsNOS).[14] All form stable dimers. Their structures are very similar to each other and to the oxygenase domain of mNOS (Figure 5.2), but bacterial NOS lack part of the H_4B binding domain.[2] Despite slight differences in heme electronics and substrate/cofactor binding, bacterial NOS and mNOS are suggesed to share the same mechanism for catalytic production of NO from L-Arg via the bound NOHA intermediate.[15] There are various advantages to working with bacterial NOS including good expression yields in *E. coli* and increased stability.[16] Lessons learned from these NOS-like enzymes can be applied to their mammalian counterparts.

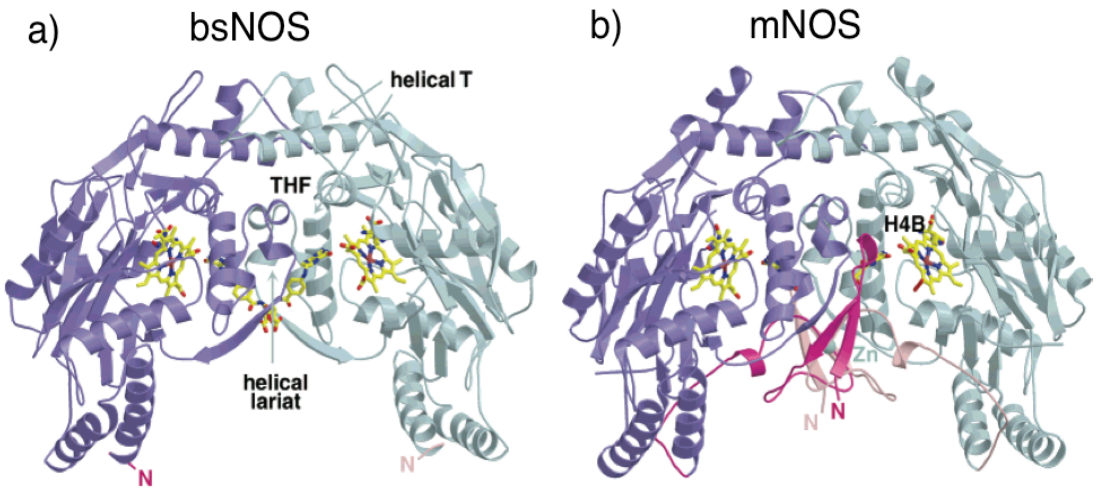

Figure 5.2 Comparison of representative dimeric structures of bacterial and mammalian NOS showing nearly identical overall folds: a) *Bacillus subtilis*, highlighting alternate bound cofactor, tetrahydrofolate (THF); b) inducible NOS from mammalian macrophages, highlighting bound cofactor, tetrahydrobiopterin (H_4B) and the missing N-terminal hook in pink (reproduced from Pant[12]).

It is of great interest to understand how NOS interacts with diatomic ligands since O_2 is a reactant (cosubstrate) and NO is a product in this very complex transformation.

Various techniques, including UV-visible spectroscopy,[15] stopped-flow spectrophotometry,[17] X-ray crystallography,[18,19] Electron Paramagnetic Resonance (EPR)/Electron-Nuclear Double Resonance (ENDOR),[8] and Raman spectroscopies,[20,21] have been used to gain insight into interactions of diatomics with mNOS and bacterial NOS. Studies involving O_2 are challenging, so both NO and carbon monoxide (CO) have been used as surrogates for gas-binding. Single-turnover experiments are better suited for studies of NO release.[22,23,24,25]

There are many open questions about gas diffusion pathways and interactions of diatomics with heme while substrate/cofactor are bound. Despite lacking part of the H_4B binding site, bacterial NOS binds H_4B at the dimer interface with residues from each subunit.[2] Crystal structures of bsNOS show formation of a destabilized "loose" dimer that converts to a "tight" dimer upon substrate/cofactor binding in a cooperative fashion.[26] Another significant difference between mammalian and bacterial NOSs is in the notably slower NO-release rates observed for bacterial NOS enzymes.[2] Structure and sequence comparisons reveal variations in a few key residues thought to "gate" NO release.[12,25] For example, a conserved Val located directly above the distal side of the heme in mNOS is substituted by an Ile in many bacterial NOSs; this substitution is thought to slow gas release by sterically constraining the active site.[27] The second gate residue shows more variation, both in position and size of residue, but again NO-release rates seem correlated with steric bulk.[14,25] These gate effects on NO-release have been studied by single-turnover experiments. Taken together, substrate/cofactor binding, as well as amino acid composition along diffusion pathways, create structural and electronic changes that affect the interaction of gsNOS with diatomics.

NOS from the thermostable and nonpathogenic bacterium, *Geobacillus stearothermophilus* (gsNOS), presents a unique and convenient system to study. The three-dimensional structure of gsNOS is remarkably similar to other bacterial NOS enzymes, as well as $mNOS_{oxy}$.[14] However, gsNOS has more constrained distal and proximal heme environments, a slightly more compact overall fold as compared with other bacterial NOS, and exhibits the slowest recorded NO-release rate of all NOS enzymes studied to date.[14]

Given these interesting properties, it is of interest to study the process by which diatomic molecules bind to gsNOS, in addition to diatomic release. CO binds to ferrous heme and thus can be used as a surrogate for O_2 binding, as mentioned above. Flash photolysis of preformed ferrous-CO adducts is a useful technique for studying interactions of heme proteins with diatomics.[28–30] Excitation by visible light causes rapid CO dissociation and because the iron retains its Fe(II) oxidation state, the released CO can rebind. This rebinding process can be followed by transient absorption (TA) spectroscopy that monitors changes in the heme Soret maxima (e.g., ferrous NOS-CO λ_{max} = 446 nm vs. ferrou NOS λ_{max} = 415 nm).[19] Preliminary CO-photolysis experiments have been performed previously with gsNOS variants to determine whether diatomic ligand rebinding (in addition to NO release) is affected by channel gating.[31] While these types of experiments are extremely useful, they do not necessarily report on the direct binding event. Furthermore, these initial studies were performed in the absence of substrate, which has substantial effects on the heme active site and overall gsNOS dimeric structure.

A method of triggering rapid heme reduction (faster than mixing) is needed to study the direct binding event of diatomic molecules such as O_2 or CO to gsNOS. The Gray group has developed "flash-quench" methodology[32] to trigger redox events in small molecule[33,34] and protein[35] systems and is described in detail in chapters one and three of this thesis. Briefly, laser excitation (the "flash") into the metal-ligand charge-transfer (MLCT) band of a ruthenium(II)diimine photosensitizer creates an electronic excited state. Introduction of another small-molecule in solution (the "quench") can lead to the formation of either a potent -1.3 V reductant, $[Ru(bpy)_3]^{1+}$, or +1.3 V oxidant, $[Ru(bpy)_3]^{3+}$.[36] From there, electrons can either be injected into or pulled from the heme, in the case of NOS.

Previous chapters of this thesis describe covalent attachment of a $[Ru(bpy)_2(IA\text{-}phen)]^{2+}$ photosensitizer (where IA-phen = 5-iodoacetamido-1,10-phenanthroline) to an engineered Cys115 on the surface of gsNOS, forming the $Ru(II)_{K115C}$-gsNOS conjugate. Under reductive "flash-quench" conditions, this modification provides a route to bypass the need for a separate reductase domain and allows for phototriggered heme reduction. Chapter three describes initial laser studies showing formation of the ferrous species with a rate of k_{obs} = 1.6 x 10^6 s^{-1} (τ = 625 ns) that is independent of presence of L-Arg or NOHA substrate or H_4B cofactor. In the hopes of observing downstream intermediates in the NOS catalytic cycle, experiments were performed in the presence of oxygen. Unfortunately the kinetics were extremely complicated by the redox-active nature of O_2, presumably due to interactions with the transiently formed Ru(I) label and/or the reductive quencher. Thus, while we were able to generate the ferrous heme, we were unable to definitively assign formation of a ferrous-oxy species. In order to explore the

diatomic binding event, we turn to CO as a redox-inactive substitute. Using similar reductive flash-quench conditions with our $Ru(II)_{K115C}$-gsNOS conjugate, we hope to initiate direct CO-binding as shown in Scheme 5.1. Given the large changes in heme absorbance upon formation of Fe(II)-CO, transient absorption (TA) spectroscopy can be used to observe this binding reaction. Furthermore, experiments in the presence of substrates can be performed to investigate their effects on diatomic ligand interactions with the active site of gsNOS.

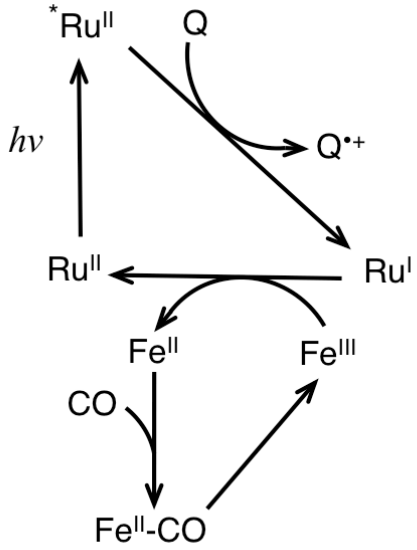

Scheme 5.1 Reductive flash-quench scheme for CO-binding upon heme reduction in gsNOS. Ru represents the $[Ru(bpy)_2(IA\text{-}phen)]^{2+}$ complex attached to gsNOS, Q represents the quencher *p*-methoxy-*N.N*-dimethylanaline (MeODMA), and Fe represents gsNOS heme.

5.2 Results and Discussion

Reductively Quenching the Model Complex $[Ru(bpy)_2(A\text{-}phen)]^{2+}$ in the Presence of CO

Photophysical properties of the model complex $[Ru(bpy)_2(A\text{-}phen)]^{2+}$ (where A-phen = 5-acetamido-1,10-phenanthroline) were explored under an atmosphere of CO. These experiments were performed in order to determine whether the presence of CO

would affect formation rates of the *Ru(II) excited state or the reductive quenching by *p*-methoxy-*N.N*-dimethylanaline (MeODMA) to form the Ru(I) state. As described in chapter three, the *Ru(II) excited state is luminescent with an emission maximum centered around 630 nm. Following 480 nm laser excitation into the tail of the Ru(II) MLCT band, the *Ru(II) luminescence decays with a lifetime on the order of $\tau \sim 1$ μs. Upon introduction of excess MeODMA, the luminescence decay at 630 nm is effectively quenched with a pseudo-first-order rate constant of $k = 1.7 \times 10^{7}$ s^{-1} ($\tau \sim 60$ ns), providing a rate of Ru(I) formation. These experiments were repeated under an atmosphere of CO and no changes to the quenched lifetime were observed.

TA was measured for the same samples at wavelengths in the region of both Ru(II) absorbance and the heme Soret (400–440 nm). In the presence of MeODMA quencher, TA traces of the $[Ru(bpy)_2(A\text{-}phen)]^{2+}$ model complex exhibit a nearly instantaneous initial bleach (negative optical density, $\Delta OD < 0$) indicative of *Ru(II) excited state formation, followed by a return to baseline suggesting formation of the Ru(I) species with a rate constant similar to that of the luminescence decay. These rates are unchanged in the presence of CO (Figure 5.3). As discussed in Chapter Three, there is a further increase in ΔOD that develops at longer timescales (~100 μs) that is tentatively assigned to side reactions of the MeODMA radical cation over time. These data indicate that CO does not interact with the model complex or the quencher to affect formation of transient species in the flash-quench scheme.

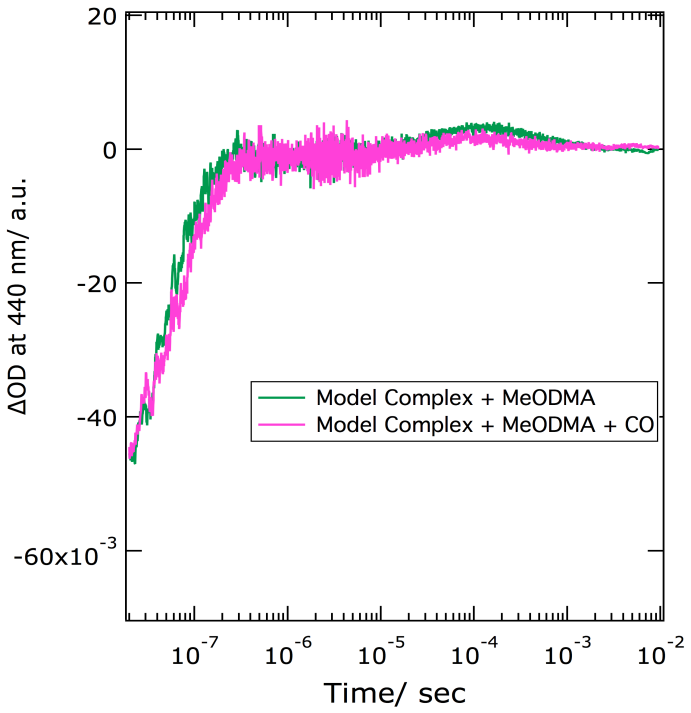

Figure 5.3 Representative transient absorption at 440 nm for the quenched model complex $[Ru(bpy)_2(A\text{-}phen)]^{2+}$ in the presence and absence of CO showing initial bleach from $^*Ru(II)$, the formation of Ru(I), and slight positive ΔOD at longer timescales. $[Ru(bpy)_2(A\text{-}phen)]^{2+}]$ = 8 μM and [MeODMA] = 8 mM, 50 mM sodium phosphate buffer, pH 7.

Phototriggered CO-binding of Ru(II)$_{K115C}$-gsNOS

Luminescence decay (630 nm) for the $^*Ru(II)$ excited state of our photosensitizer-labeled gsNOS system, $Ru(II)_{K115C}$-gsNOS, is described by a biexponential function (τ_1 = 1.2 μs and τ_2 = 150 ns). These rates likely reflect multiple solution conformations of the label that do not interconvert within the timescale of these measurements. The same rates and distribution are observed in the presence of CO, indicating that CO does not interact with the $^*Ru(II)$ excited state. Addition of excess MeODMA quencher results in a faster luminescence decay with a single observed lifetime ($\tau_{quenched}$ = 60 ns), similar to that of the quenched model complex. Experiments performed in the presence of CO yield the

same quenched rate ($\tau_{quenched,CO}$ = 63 ns), again suggesting that the rate of Ru(I) formation is unaffected by CO. Figure 5.4 shows luminescence data for the $Ru(II)_{K115C}$-gsNOS system under the above experimental conditions. The $^{*}Ru(II)$ excited state is the only emissive species in our system, so transient luminescence data alone do not report on what is happening at the heme center of gsNOS.

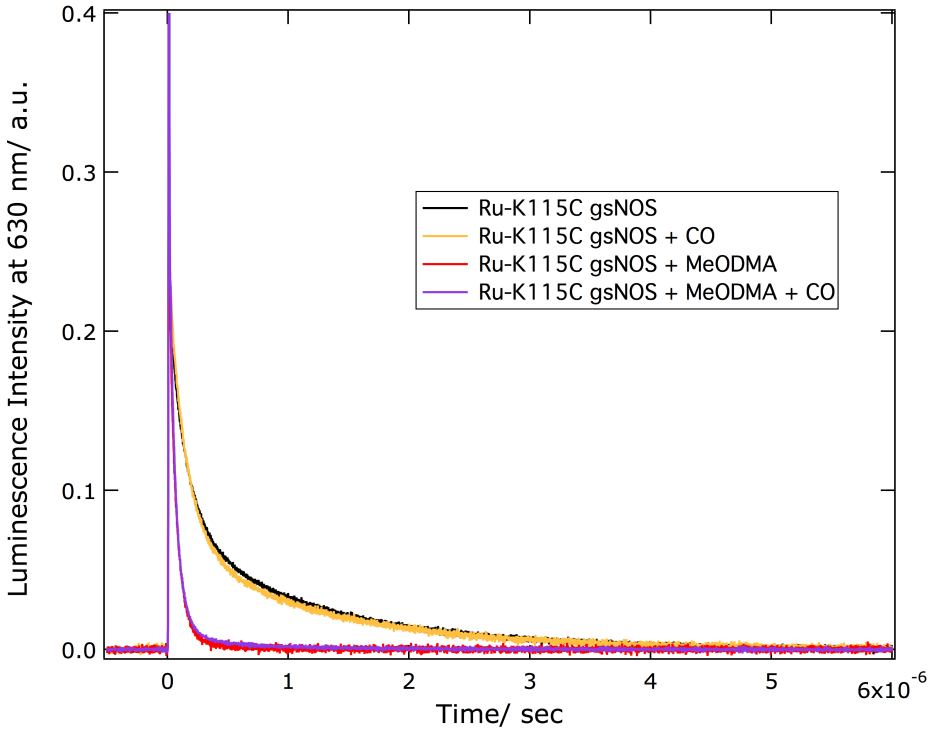

Figure 5.4 Luminescence decays for the labeled protein $Ru(II)_{K115C}$-gsNOS showing unquenched and quenched lifetimes are unaffected by CO. Samples were excited at 480 nm and monitored at 630 nm. [$Ru(II)_{K115C}$-gsNOS] = 8 μM and [MeODMA] = 8 mM, 50 mM sodium phosphate buffer, pH 7.

As mentioned above, there are changes in the gsNOS Soret maximum upon reduction and CO-binding. Chemically reduced samples were prepared in a glove box and back-filled with CO to obtain ground state UV-visible spectra of the species we hope to generate transiently under flash-quench conditions (Figure 5.5). The resulting difference spectrum provides a spectroscopic handle for TA measurements.

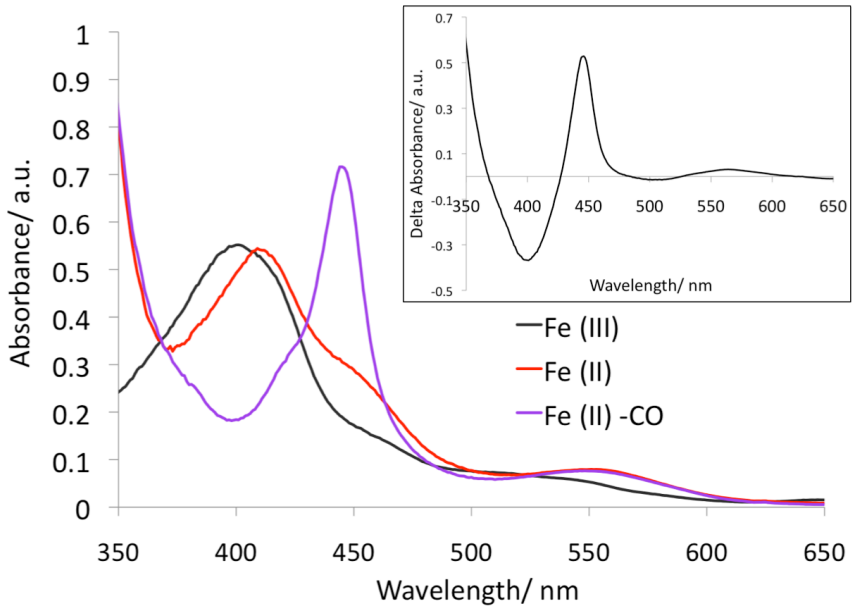

Figure 5.5 UV-visible absorption spectra of $Ru(II)_{K115C}$-gsNOS showing Soret maxima for the Fe(III) heme, chemically reduced Fe(II), and Fe(II)-CO species. Inset: difference spectrum between the oxidized resting state and chemically prepared Fe(II)-CO $Ru(II)_{K115C}$-gsNOS.

TA measurements were performed to track changes in both the ruthenium photosensitizer and at the gsNOS heme active site for our $Ru(II)_{K115C}$-gsNOS system. In the absence of quencher we have previously observed laser-induced formation of the $^{*}Ru(II)_{K115C}$-gsNOS-Fe(III) excited state that is characterized by a negative ΔOD in the Ru(II) absorbance (400–440 nm) with a return to baseline on the same timescale as its luminescence decay. We found no evidence for transient species associated with changes in the heme Soret absorbance. These same measurements made in the presence of CO show slight qualitative differences in their returns to baseline (to the Ru(II) ground state) (Figure 5.6). However, fitting the data to biexpoential functions yields essentially the same lifetimes (τ_1 = 1.0 μs and τ_2 = 140 ns; $\tau_{1,CO}$ = 1.3 μs and $\tau_{2,CO}$ = 130 ns), similar to the rates observed for the luminescence decays.

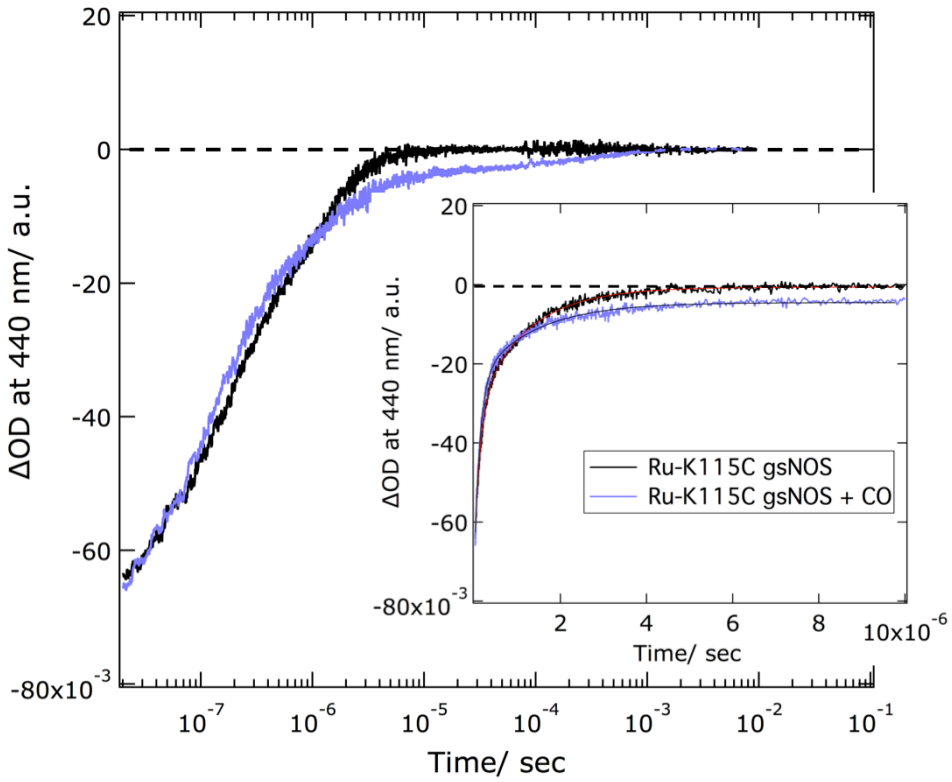

Figure 5.6 Transient absorption data at 440 nm of unquenched $Ru(II)_{K115C}$-gsNOS in the presence and absence of CO. Inset: data from early timescale, fit to biexponential functions. [$Ru(II)_{K115C}$-gsNOS] = 8 μM, 50 mM sodium phosphate buffer, pH 7.

We know from previous experiments (detailed in chapter three) that ferrous gsNOS forms under reductive flash-quench conditions. If CO binds, we expect to see a further red shifted heme Soret at 440 nm (Figure 5.5). The next step was to measure TA in the presence of MeODMA quencher and CO. TA traces at 440 nm for quenched $Ru(II)_{K115C}$-gsNOS in the presence and absence of CO both show the expected faster loss of $^{*}Ru(II)$ signal and an overall increase in ΔOD at intermediate times associated with the formation of ferrous heme. However, the samples containing CO show less intensity associated with Fe(II) formation, followed by a large increase in ΔOD at longer times (Figure 5.7). We assign this new transient species as Fe(II)-CO. Despite the differences in early signal intensity, the biexponential fits show similar rates with time constants $\tau_{1,CO}$ =

70 ns and $\tau_{2,CO}$ = 770 ns (as compared with samples under argon, τ_1 = 62 ns and τ_2 = 625 ns). The bimolecular rate of Fe(II)-CO formation cannot be extracted without kinetics modeling of CO concentration dependence studies, which have not yet been conducted. However the observed signal forms on the order of ~1 ms and is consistent with rates observed in CO-photolysis studies where the rebinding process is monitored.[31] The final decay back to baseline is assumed to be associated with reoxidation by the MeODMA radical cation, a process that would release CO from the heme.

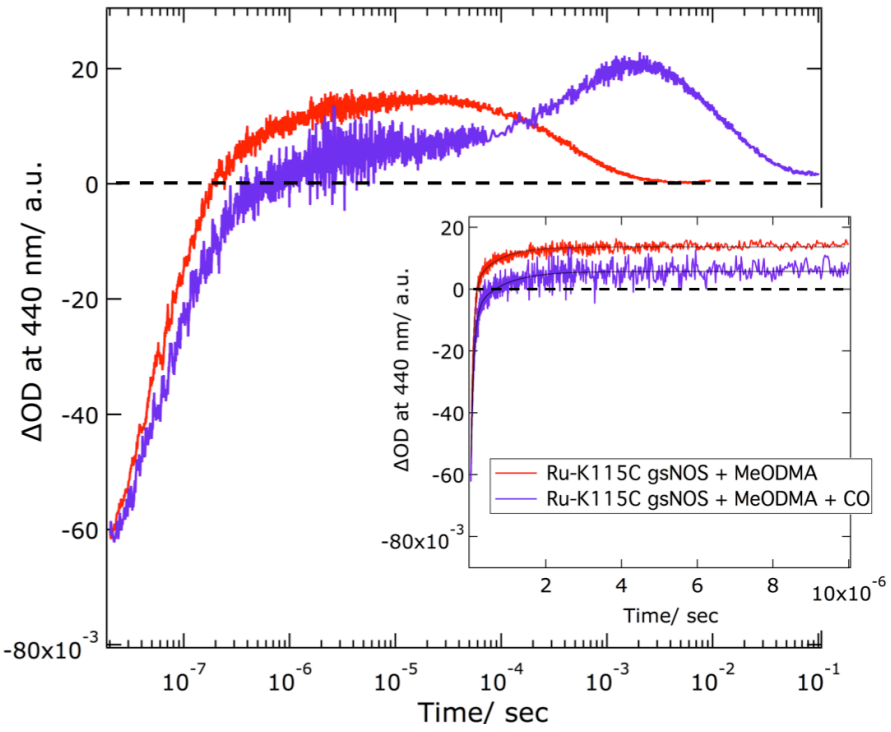

Figure 5.7 Transient absorption data at 440 nm of quenched $Ru(II)_{K115C}$-gsNOS in the presence and absence of CO. Inset: data from early timescale, fit to biexponential functions. [$Ru(II)_{K115C}$-gsNOS] = 8 μM, [MeODMA] = 8 mM, 50 mM sodium phosphate buffer, pH 7.

The assignment of Fe(II)-CO was confirmed by TA measurements at multiple wavelengths. These data show bleached signals measured at 400 and 420 nm at rates concomitant with the increase in ΔOD at 440 nm (Figure 5.8).

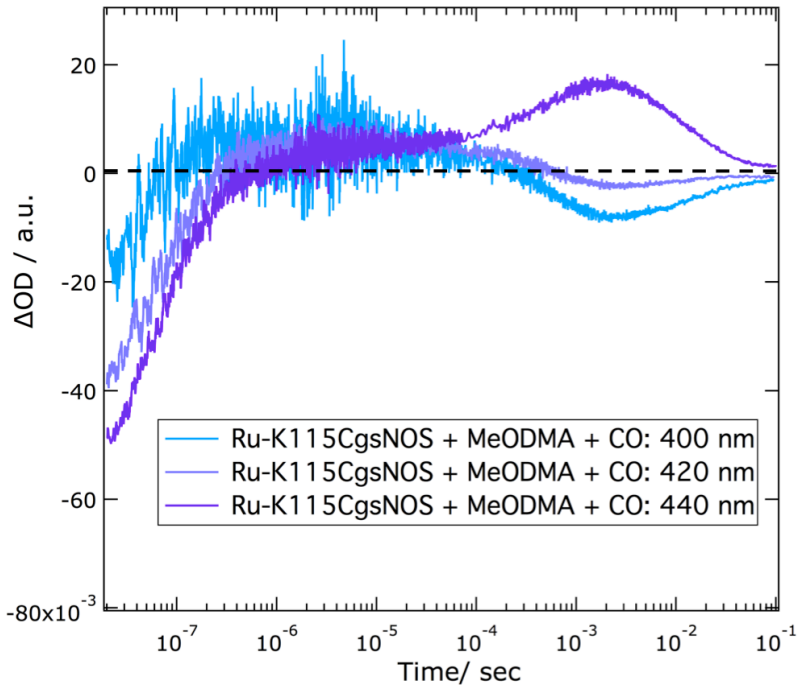

Figure 5.8 Transient absorption data at multiple wavelengths of quenched $Ru(II)_{K115C}$-gsNOS + CO. [$Ru(II)_{K115C}$-gsNOS] = 8 μM, [MeODMA] = 8 mM, 50 mM sodium phosphate buffer, pH 7.

Removal of CO from the sample by equilibrating overnight under argon basically results in a return to the signals seen in samples that were never exposed to CO. There is still slightly increased ΔOD at longer timescales, that may come from small amounts of Fe(II)-CO formed due to residual CO in the protein matrix during degassing. Alternatively, it could be the result of more thorough degassing in general that extends the natural lifetime of the ferrous species. Interestingly, the signals coming from initial formation of Fe(II) reach the same intensity, indicating that the lower intensity seen in CO samples comes from CO-binding and not from some other differences in the $Ru(II)_{K115C}$-gsNOS sample (Figure 5.9).

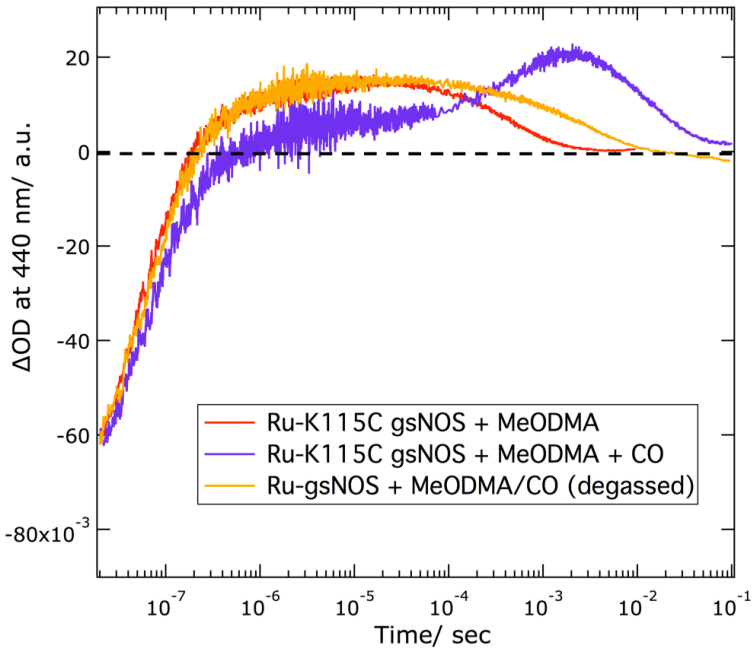

Figure 5.9 Transient absorption data at 440 nm of quenched $Ru(II)_{K115C}$-gsNOS comparing samples made in the absence of CO, presence of CO, and then degassed with Argon to remove CO. [$Ru(II)_{K115C}$-gsNOS] = 8 μM, [MeODMA] = 8 mM, 50 mM sodium phosphate buffer, pH 7.

Phototriggered CO-binding of $Ru(II)_{K115C}$-gsNOS in the Presence of Substrates

The same flash-quench experiments described in the previous section with $Ru(II)_{K115C}$-gsNOS in the presence of CO were performed with substrate bound. As before, CO-binding was monitored by TA and assigned by large positive ΔOD signals at 440 nm. The experiments with L-Arg bound show very little CO binding. Samples with NOHA bound show markedly increased Fe(II)-CO formation compared with L-Arg, but still less than substrate-free enzyme (Figure 5.10). Differences between the two substrates can be rationalized by their different modes of interaction with diatomic ligands in the active site of gsNOS as previously reported.[21]

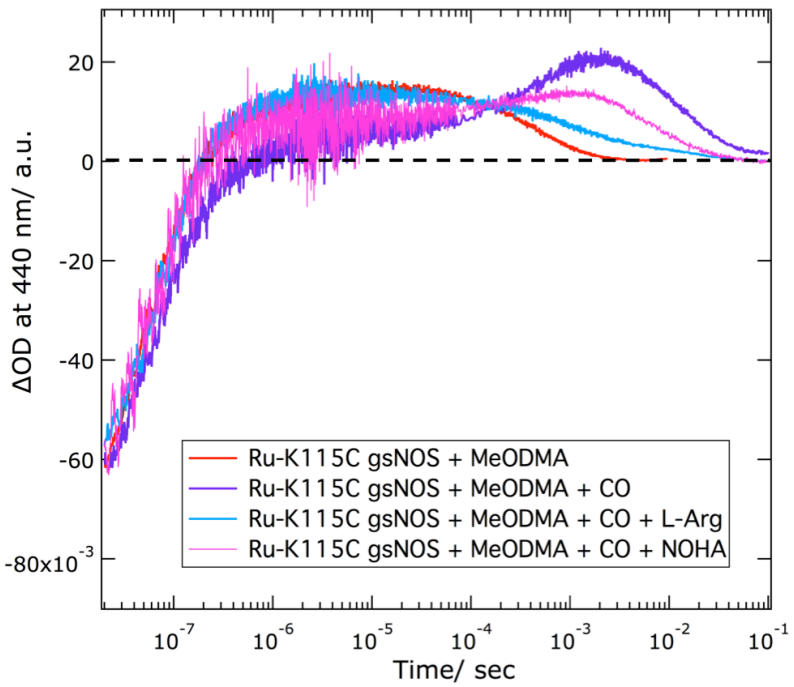

Figure 5.10 Transient absorption data at 440 nm of quenched $Ru(II)_{K115C}$-gsNOS + CO in the presence of each substrate. $[Ru(II)_{K115C}\text{-gsNOS}]$ = 8 μM, [MeODMA] = 8 mM, [L-Arg] = [NOHA] = 200 μM, 50 mM sodium phosphate buffer, pH 7.

These data that show less overall CO binding were initially confusing given that L-Arg or NOHA must be bound in the active site before the O_2 binding events in the native NOS cycle. There are differences between the binding modes of O_2 and CO: O_2 adopts a bent geometry and CO binds linearly to Fe(II) heme. But it still seems unlikely that substrate binding would sterically exclude a diatomic molecule of comparable size. This difference in binding can be explained however, if one considers the large overall structural and active site changes associated with substrate binding seen in bacterial NOS enzymes. As previously mentioned, crystal structures of NOS from *Bacillus subtilis* (bsNOS) show two distinct dimer conformations in the presence and absence of substrate/cofactor: a "tight" and "loose" form (Figure 5.11).[26] Substrate/cofactor binding induces formation of the "tight" dimer, resulting in structural changes at the interface that

bring the two heme active sites closer by approximately 3 Å and translates the subunits by 11 Å. The buried surface area at the dimer interface condenses from 1115 to 480 $Å^2$ per subunit. Furthermore, the helical T-regions lose most of their interactions in the "loose" form, whereas they make close contacts in the "tight" form that are crucial to dimer stability. The consequence of this increased peripheral rigidity and increased dimer association is that the heme is markedly less solvent-exposed in the presence of substrate/cofactor. Furthermore, H_4B binding blocks the proximal channel.

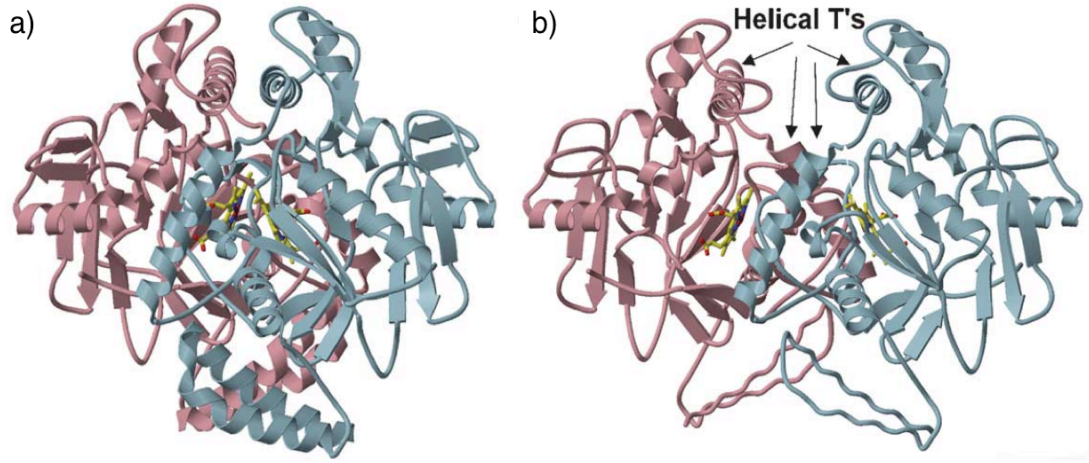

Figure 5.11 Ribbon diagrams of the crystal structures of bsNOS in presence and absence of substrate/cofactor. Subunits are shown in pink and light blue. a) bsNOS with the bound substrate L-Arg forms a "tight" dimer with close contacts formed by the helical T and N-terminal hairpin from each subunit and b) bsNOS in the absence of substrate forms a "loose" dimer and translates one subunit by approximately 11 Å exposing 50% more surface area. Figure reproduced from Pant.[26]

If such a dimeric contraction is occurring with our $Ru(II)_{K115C}$-gsNOS system, it could account for the decreased amount of Fe(II)-CO formation in the presence of substrate. To investigate whether more time was needed to allow CO access to the interior of the contracted substrate-bound protein, two experiments were performed. One where L-Arg-bound gsNOS was chemically reduced in an anaerobic chamber and then

back-filled with CO and another where the samples containing L-Arg were allowed to pre-equilibrate overnight under an atmosphere of CO before flash-quench. Given the steady-state nature of the first experiment, collection of UV-visible absorption spectra were enough to definitively show that reduced L-Arg-bound $Ru(II)_{K115C}$-gsNOS is capable of binding CO (Figure 5.12). Opening the cuvette to air results in the reoxidation to the Fe(III) state over minutes and the release of CO.

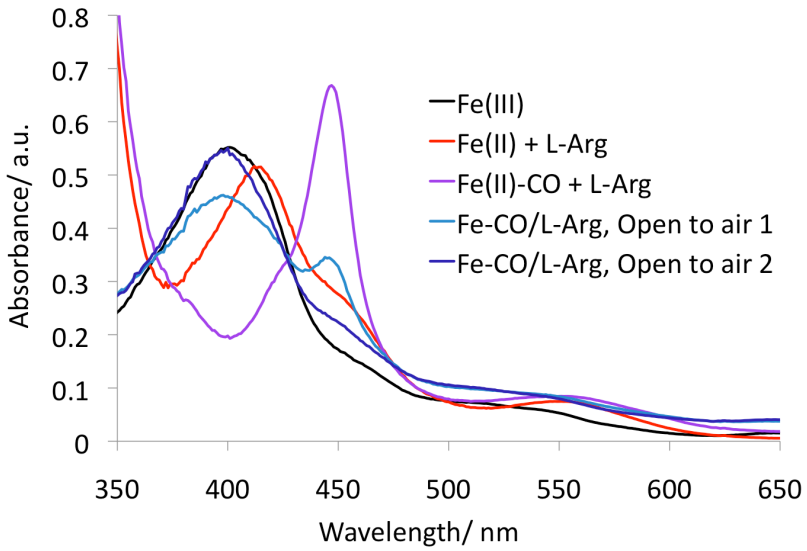

Figure 5.12 UV-visible absorption spectra of $Ru(II)_{K115C}$-gsNOS showing Soret maxima for chemically reduced Fe(II) and Fe(II)-CO species both bound to L-Arg. The broader Soret in the original Fe(III) spectrum is due to lack of substrate in that sample.

TA measurements of the pre-equilibrated sample in the second experiment were performed and show more formation of the L-Arg-bound Fe(II)-CO species as compared to freshly made L-Arg samples. This adds further support to the idea that more time is required for CO to access the heme in the contracted dimer (Figure 5.13).

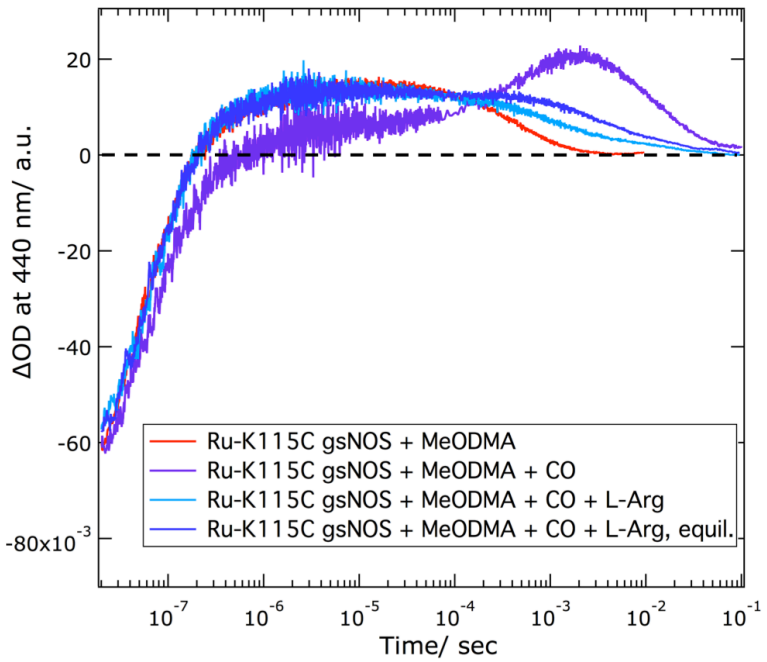

Figure 5.13 Transient absorption data at 440 nm of quenched L-Arg-bound $Ru(II)_{K115C}$-gsNOS given time to equilibrate with CO overnight. [$Ru(II)_{K115C}$-gsNOS] = 8 μM, [MeODMA] = 8 mM, [L-Arg] = 200 μM, 50 mM sodium phosphate buffer, pH 7.

It is very likely that substrate binding has profound effects on both diatomic gas binding and release. Raman studies of CO-bound gsNOS in particular show unique environments in both the distal and proximal heme cavities upon diatomic binding in the absence of substrate/cofactor suggesting two distinct populations of ferrous-CO are present.[21] Indeed, flash-photolysis studies of CO re-binding of substrate-free gsNOS show biexponential behavior suggesting two different binding modes.[31] This is different than the single NO-release rate observed in single-turnover experiments loaded with substrate and cofactor.[25]

Furthermore, two NO-release "gate" residues have been identified in NOS.[12,25] Bacterial NOS enzymes have a bulkier Ile at position 223, directly above the heme in the distal pocket, and a His at position 134 in the substrate channel. Swap mutations have

been prepared in bsNOS and lead to increased NO-release rates.[27] These "gate" mutations have been made in gsNOS (Ile223Val, His134Ser, and Ile223Val/His134Ser)[25] to explore the pathway for diatomic release. The resultant rates of NO-release were measured and it was observed that less bulk at these positions resulted in faster NO release rates, supporting the idea that bulk gates the release of NO. Flash-photolysis studies of CO re-binding of these substrate-free gsNOS "gate" mutants were complicated by biexponential behavior. It would be greatly informative to perform the flash-quench direct CO-binding studies described in this chapter on these mutants in the presence of substrate, as well as cofactor. This type of measurement could then be compared to the NO-release single-turnover experiments to investigate whether diatomic binding and release share the same pathway. Additional mutations could be made to *increase* the bulk in the distal channel. Inspection of space-filling models of gsNOS in Pymol suggest that the single mutants Ile223Leu, His134Trp, and the double mutant Ile223Leu/His134Trp would provide more channel bulk, without fully blocking substrate access. If CO-binding rates remain the same, while NO-release is slowed, that would provide information that diatomic binding occurs through a different pathway than release.

5.3 Conclusion

It is of interest to understand how NOS interacts with diatomic ligands since O_2 is a reactant (cosubstrate) and NO is a product in the catalytic cycle. CO can be used as a redox-inactive surrogate for O_2, as it also binds to ferrous heme. Fe(II)-CO produces a large shift in the Soret absorbance that can be used as a spectroscopic handle in transient absorption measurements. Reductive flash-quench experiments have been performed

using our $Ru(II)_{K115C}$-gsNOS system to transiently reduce the heme and allow CO binding. TA measurements show clear formation of the Fe(II)-CO adduct on the order of 1 ms, however further experiments are needed to extract the bimolecular rate constant. Measurements made with substrate-bound $Ru(II)_{K115C}$-gsNOS show differing amounts of Fe(II)-CO formation. These data suggest that the observed substrate-induced structural changes in both the dimer and the active site itself could play a role in diatomic gas binding. This is the first study where the direct binding event of CO to NOS has been observed and represents a starting point for deeper investigations into the factors that affect diatomic ligand binding in NOS.

5.4 Acknowledgements

I would like to thank Dr. Jeff Warren for his assistance with setting up the CO line and more importantly for his insights into gas diffusion in NOS; I would also like to acknowledge Dr. Charlotte Whited for her inspiring initial work with NO-release and CO rebinding in NOS.

5.5 Materials and Methods

Labeled protein $Ru(II)_{K115C}$-gsNOS was prepared as described in chapter two of this thesis. L-arginine (L-Arg, Sigma) was used as received and stored at room temperature. N^{ω}-hydroxy-L-arginine acetate salt (NOHA, Sigma) was stored at 4 °C and freshly dissolved before each use to prevent hydrolysis. (6R)-5,6,7,8-tetrahydrobiopterin (H_4B, Sigma) was stored at -20 °C. The model complex $[Ru(bpy)_2(A\text{-}phen)]^{2+}$ and *p*-

methoxy-*N.N*-dimethylanaline (MeODMA) were prepared and handled as described in chapter three.

General Sample Preparation

All samples were prepared in 50 mM sodium phosphate (NaPi) buffer, pH 7 using Milli-Q (18.2 MΩ) water and filtered (0.22 μm, Millipore) before use. *Note:* all ruthenium(II) diimine-containing samples were kept covered in foil or handled under red light to prevent photodamage. Specialized 1 cm pathlength quartz cuvettes (Starna Cells) fitted with Kontes valves and side-arm ground-glass Schlenk adaptors were made in-house at the Caltech glassblowing shop (Rick Gerhart). Cuvettes containing micro stir bars were attached to a Schlenk line and degassed by three sets of ten pump-purge cycles (very quick vacuum, followed by argon back-filling) spaced in 15 min intervals. This method provides a gentle way to degas protein samples that avoids denaturation caused by bubbling. Argon gas was precleaned by a commercially available oxygen scrubber before entering the line (Oxiclear, Labclear).

Samples for steady-state CO-binding were prepared in an anaerobic chamber ("wet" glove box used for aqueous samples) under an inert atmosphere of nitrogen. $Ru(II)_{K115C}$-gsNOS was reduced with sodium dithionite. Excess dithionite was removed using a PD-10 desalting column (GE Healthcare), equilibrated with degassed NaPi buffer, pH 7. L-Arg was added to the samples, which were then sealed in quartz cuvettes fitted with a Kontes valve and a side-arm ground-glass Schlenk adaptor (as previously described for degassed samples). The sealed samples were removed from the box and attached to a separate Schlenk line containing carbon monoxide. The cuvettes were back-filled with CO following the pump-purge method described for argon to provide a nearly

100% CO atmosphere in the cuvette. Given the toxicity of CO, extra care was taken when using this line, including the use of a CO monitor in the hood.

Typical sample volumes for TA measurements were 2 mL to provide enough height in the cuvette to accommodate both a micro stir bar and the width of laser/probe light without spatial interference. Labeled protein and model complex concentrations were chosen to balance decent signal size with ground state absorbance in the range of 0.8 OD at the Soret maximum and 0.4 at the Ru shoulder. Quencher concentrations were kept at 1000-fold excess to allow fitting of pseudo-first-order kinetics. Substrate concentrations were chosen to ensure all proteins were bound and mimicked conditions used in published single-turnover studies. Sample component concentrations were as follows: $[Ru(II)_{K115C}\text{-gsNOS}]$ = 8 μM, $[[Ru(bpy)_2(A\text{-phen})]^{2+}]$ = 8 μM, [MeODMA] = 8 mM, [L-Arg] = 200 μM, and [NOHA] = 200 μM.

Spectroscopic Measurements

All steady state and time-resolved spectroscopic measurements were carried out at the Beckman Institute Laser Resource Center. UV-visible absorption spectra were recorded on an Agilent 8453 UV-vis Spectrophotometer. Laser excitation for time-resolved measurements was provided by 8 ns pulses from a 10 Hz Q-switched Nd:YAG laser (Spectra-Physics Quanta-Ray PRO-Series). The third harmonic (355 nm) was used to pump an optical parametric oscillator (OPO, Spectra-Physics Quanta- Ray MOPO-700, tunable in the visible region). Laser light from the OPO at 480 nm with a final power of approximately 10 mJ/pulse (at the sample) was used to excite samples. Probe light for transient absorption kinetics measurements was provided by a 75 W arc lamp (PTI Model A 1010). Details and schematics for the laser and optical configuration for transient

luminescence and absorption measurements can be found in the methods section of chapter three.

Data Fitting

Initial transient absorption data manipulation was performed using MATLAB R2010a (Mathworks, Inc.) as follows: for each wavelength, data from three different timescales (2 μs, 100 μs, and 100 ms) were logarithmically compressed with 600 points per decade. The compressed data were adjusted to match intensities by inspection, spliced together, and the x-axis was shifted to set the signal rise to $t = 0$. Data were fit to multiple exponentials using nonlinear least-squares minimization and quality of fit was evaluated by inspection of residuals. Global least-squares analysis was used to fit data from multiple wavelengths to a single set of rates and amplitudes. Simple biexponential fitting for TA data and all TA plots were made using IgorPro 6.1 (Wavemetrics). UV-vis data were processed using Microsoft Excel.

5.6 References

1. Hughes, M. N. Chemistry of Nitric Oxide and Related Species. *Methods in Enzymology* **436**, 3–19 (2008).
2. Crane, B. R., Sudhamsu, J. & Patel, B. A. Bacterial Nitric Oxide Synthases. *Annu Rev Biochem* **79**, 445–470 (2010).
3. Alderton, W. K., Cooper, C. E., Knowles, R. G. Nitric Oxide Synthase: Structure, Function, and Inhibition. *Biochem J* **357**, 593-615 (2001).
4. Griffith, O. W., Stuehr, D. J., Annual Reviews Physiology 1995, 57, 707-736.
5. Sono, M., Roach, M. P., Coulter, E. D., Dawson, J. H., Heme-Containing Oxygenases. *Chem Rev* **96**, 2841-2887 (1996).
6. Stuehr, D. J. Update on Mechanism and Catalytic Regulation in the NO Synthases. *J Biol Chem* **279**, 36167–36170 (2004).
7. Wei, C.-C., Crane, B. R. & Stuehr, D. J. Tetrahydrobiopterin Radical Enzymology. *Chem Rev* **103**, 2365–2384 (2003).
8. Davydov, R. *et al.* EPR and ENDOR Characterization of Intermediates in the Cryoreduced Oxy-Nitric Oxide Synthase Heme Domain with Bound l-Arginine or N G Hydroxyarginine. *Biochemistry* **41**, 10375–10381 (2002).
9. Woodward, J. J., Chang, M. M., Martin, N. I. & Marletta, M. A. The Second Step of the Nitric Oxide Synthase Reaction: Evidence for Ferric-Peroxo as the Active Oxidant. *J Am Chem Soc* **131**, 297–305 (2009).
10. Kunst, F., Ogasawara, N., Moszer, I. & et al. The complete genome sequence of the gram-positive bacterium Bacillus subtilis. *Nature* **390**, 249–256 (1997).
11. Adak, S. Direct Evidence for Nitric Oxide Production by a Nitric-oxide Synthase-like Protein from Bacillus subtilis. *J Biol Chem* **277**, 16167–16171 (2002).
12. Pant, K., Bilwes, A. M., Adak, S., Stuehr, D. J. & Crane, B. R. Structure of a Nitric Oxide Synthase Heme Protein from Bacillus subtilis. *Biochemistry* **41**, 11071–11079 (2002).
13. Bird, L. E. *et al.* Crystal structure of SANOS, a bacterial nitric oxide synthase oxygenase protein from Staphylococcus aureus. *Structure* **10**, 1687–1696 (2002).
14. Sudhamsu, J. Structure and Reactivity of a Thermostable Prokaryotic Nitric-oxide Synthase That Forms a Long-lived Oxy-Heme Complex. *J Biol Chem* **281**, 9623–9632 (2005).
15. Salard-Arnaud, I., Stuehr, D., Boucher, J.-L. & Mansuy, D. Spectroscopic, catalytic and binding properties of Bacillus subtilis NO synthase-like protein: Comparison with other bacterial and mammalian NO synthases. *J Inorg Biochem* **106**, 164–171 (2012).
16. Sudhamsu, J. & Crane, B. R. Bacterial nitric oxide synthases: what are they good for? *Trends Microbiol* **17**, 212–218 (2009).
17. Wei, C. C., Wang, Z. Q. & Stuehr, D. J. Nitric oxide synthase: Use of stopped-flow spectroscopy and rapid-quench methods in single-turnover conditions to examine formation and reactions of heme-O2 intermediate in early catalysis. *Methods Enzymol* **354**, 320–338 (2002).
18. Pant, K. & Crane, B. R. Nitrosyl−Heme Structures of Bacillus subtilis Nitric Oxide Synthase Have Implications for Understanding Substrate Oxidation. *Biochemistry* **45**, 2537–2544 (2006).

19. Doukov, T., Li, H., Soltis, M. & Poulos, T. L. Single Crystal Structural and Absorption Spectral Characterizations of Nitric Oxide Synthase Complexed with N ω-Hydroxy-l-arginine and Diatomic Ligands. *Biochemistry* **48**, 10246–10254 (2009).
20. Santolini, J., Roman, M., Stuehr, D. J. & Mattioli, T. A. Resonance Raman Study of Bacillus subtilis NO Synthase-like Protein: Similarities and Differences with Mammalian NO Synthases. *Biochemistry* **45**, 1480–1489 (2006).
21. Kabir, M., Sudhamsu, J., Crane, B. R., Yeh, S.-R. & Rousseau, D. L. Substrate−Ligand Interactions in Geobacillus stearothermophilus Nitric Oxide Synthase. *Biochemistry* **47**, 12389–12397 (2008).
22. Boggs, S., Huang, L. & Stuehr, D. J. Formation and Reactions of the Heme−Dioxygen Intermediate in the First and Second Steps of Nitric Oxide Synthesis As Studied by Stopped-Flow Spectroscopy under Single-Turnover Conditions. *Biochemistry* **39**, 2332–2339 (2000).
23. Tejero, J. *et al.* Stabilization and Characterization of a Heme-Oxy Reaction Intermediate in Inducible Nitric-oxide Synthase. *J Biol Chem* **283**, 33498–33507 (2008).
24. Agapie, T. *et al.* NO formation by a catalytically self-sufficient bacterial nitric oxide synthase from Sorangium cellulosum. *Proc Nat Acad Sci USA* **106**, 16221–16226 (2009).
25. Whited, C. A. *et al.* Gating NO Release from Nitric Oxide Synthase. *J Am Chem Soc* **134**, 27–30 (2012).
26. Pant, K. & Crane, B. R. Structure of a Loose Dimer: an Intermediate in Nitric Oxide Synthase Assembly. *Journal of Molecular Biology* **352**, 932–940 (2005).
27. Wang, Z.-Q. A Conserved Val to Ile Switch near the Heme Pocket of Animal and Bacterial Nitric-oxide Synthases Helps Determine Their Distinct Catalytic Profiles. *J Biol Chem* **279**, 19018–19025 (2004).
28. Scheele, J. S. *et al.* Kinetics of CO ligation with nitric-oxide synthase by flash photolysis and stopped-flow spectrophotometry. *J Biol Chem* **272**, 12523–12528 (1997).
29. Stevenson, T. H., Gutierrez, A. F., Alderton, W. K., Lian, L. & Scrutton, N. S. Kinetics of CO binding to the haem domain of murine inducible nitric oxide synthase: differential effects of haem domain ligands. *Biochem J* **358**, 201 (2001).
30. Cao, W. *et al.* Investigations of Photolysis and Rebinding Kinetics in Myoglobin Using Proximal Ligand Replacements. *Biochemistry* **43**, 11109–11117 (2004).
31. Whited, C. A. Tuning Nitric Oxide Synthase: Investigating the Thiolate 'Push' and NO Release; PhD Thesis; California Institute of Technology, Pasadena, 2011.
32. Chang, I. J., Gray, H. B. & Winkler, J. R. High-driving-force electron transfer in metalloproteins: intramolecular oxidation of ferrocytochrome c by Ru (2, 2'-bpy) 2 (im)(his-33) 3+. *J Am Chem Soc* **113**, 7056–7057 (1991).
33. Ogata, T., Yanagida, S., Brunschwig, B. S. & Fujita, E. Mechanistic and Kinetic Studies of Cobalt Macrocycles in a Photochemical CO2 Reduction System: Evidence of Co-CO2 Adducts as Intermediates. *J Am Chem Soc* **117**, 6708–6716 (1995).
34. Dempsey, J. L., Winkler, J. R. & Gray, H. B. Kinetics of Electron Transfer Reactions of H2-Evolving Cobalt Diglyoxime Catalysts. *J Am Chem Soc* **132**, 1060–1065 (2010).

35. Winkler, J. R. & Gray, H. B. Electron transfer in ruthenium-modified proteins. *Chem Rev* **92**, 369–379 (1992).
36. Huynh, M. H. V., Dattelbaum, D. M. & Meyer, T. J. Exited state electron and energy transfer in molecular assemblies. *Coord Chem Rev* **249**, 457–483 (2005).